Tectonophysics 536–537 (2012) 61–100

Contents lists available at SciVerse ScienceDirect

Tectonophysics

journal homepage: www.elsevier.com/locate/tecto

Earthquake source parameters along the Hellenic subduction zone and numerical simulations of historical tsunamis in the Eastern Mediterranean

Seda Yolsal-Çevikbilen *, Tuncay Taymaz

Istanbul Technical University, the Faculty of Mines, Department of Geophysical Engineering, Maslak TR-34469, Istanbul, Turkey

ARTICLE INFO

Article history:
Received 25 March 2011
Received in revised form 26 January 2012
Accepted 13 February 2012
Available online 25 February 2012

Keywords:
Active tectonics
Earthquakes
Eastern Mediterranean
Slip distribution
Source rupture parameters
Tsunamis

ABSTRACT

We studied source mechanism parameters and slip distributions of earthquakes with $M_w \geq 5.0$ occurred during 2000–2008 along the Hellenic subduction zone by using teleseismic P- and SH-waveform inversion methods. In addition, the major and well-known earthquake-induced Eastern Mediterranean tsunamis (e.g., 365, 1222, 1303, 1481, 1494, 1822 and 1948) were numerically simulated and several hypothetical tsunami scenarios were proposed to demonstrate the characteristics of tsunami waves, propagations and effects of coastal topography. The analogy of current plate boundaries, earthquake source mechanisms, various earthquake moment tensor catalogues and several empirical self-similarity equations, valid for global or local scales, were used to assume conceivable source parameters which constitute the initial and boundary conditions in simulations. Teleseismic inversion results showed that earthquakes along the Hellenic subduction zone can be classified into three major categories: [1] focal mechanisms of the earthquakes exhibiting E–W extension within the overriding Aegean plate; [2] earthquakes related to the African–Aegean convergence; and [3] focal mechanisms of earthquakes lying within the subducting African plate. Normal faulting mechanisms with left-lateral strike slip components were observed at the eastern part of the Hellenic subduction zone, and we suggest that they were probably concerned with the overriding Aegean plate. However, earthquakes involved in the convergence between the Aegean and the Eastern Mediterranean lithospheres indicated thrust faulting mechanisms with strike slip components, and they had shallow focal depths ($h<45$ km). Deeper earthquakes mainly occurred in the subducting African plate, and they presented dominantly strike slip faulting mechanisms. Slip distributions on fault planes showed both complex and simple rupture propagations with respect to the variation of source mechanism and faulting geometry. We calculated low stress drop values ($\Delta\sigma<30$ bars) for all earthquakes implying typically interplate seismic activity in the region. Further, results of numerical simulations verified that damaging historical tsunamis along the Hellenic subduction zone are able to threaten especially the coastal plains of Crete and Rhodes islands, SW Turkey, Cyprus, Levantine, and Nile Delta–Egypt regions. Thus, we tentatively recommend that special care should be considered in the evaluation of the tsunami risk assessment of the Eastern Mediterranean region for future studies.

1. Introduction

Complex tectonic evolution is responsible for intense earthquake activity, deformation, and various types of faulting mechanisms, tsunamis, volcanism and geological structures in Eastern Mediterranean. This region is so called as a natural laboratory to study the main stages of active margin development such as ocean closure and ophiolite formation, continental subduction, continent–continent collision, back-arc basin evolution, slab roll-back and slab-break-off (Fig. 1a,b; Aksu et al., 2008; Bécel et al., 2009, 2010; Ganas and Parsons, 2009; Hall et al., 2008; Laigle et al., 2008; Le Pichon and Angelier, 1981; Mascle et al., 1986; McClusky et al., 2000, 2003; McKenzie, 1972, 1978; Roumelioti et al., 2011; Shaw and Jackson, 2010; Skarlatoudis et al., 2009; Taymaz et al., 1990, 1991, 2004, 2007a, 2007b; Vassilakis et al., 2011; Yolsal-Çevikbilen, 2012; Zitter et al., 2003). Hellenic and Cyprus arcs, deep Rhodes and Finike basins, Anaximander and Erasthothenes Sea Mountains, Pliny and Strabo trenches, and the Dead Sea Transform Fault are the best examples reflecting the tectonic complexity of the region (Fig. 1b). Additionally, historical documents, earthquake catalogues (e.g. Ambraseys, 1962, 2009; Ambraseys et al., 1994; Ambraseys and Synolakis, 2010; Antonopoulos, 1980; Guidoboni and Comastri, 2005a, 2005b; Guidoboni and Ebel, 2009; Papadopoulos, 2001; Sbeinati et al., 2005; Soloviev et al., 2000) and several tsunami studies (e.g. Bilham, 2008; Fokaefs and Papadopoulos, 2006; Guidoboni and Comastri, 1997; Okal et al., 2009; Shaw et al., 2008; Yalçıner et al., 2004; Yolsal et al., 2007) clearly demonstrate the tsunami potential along the Eastern Mediterranean coastal plains. They verified many catastrophic earthquake-induced tsunamis occurred particularly along the convergent plate

* Corresponding author. Tel.: +90 2122856260.
E-mail address: yolsalse@itu.edu.tr (S. Yolsal-Çevikbilen).

0040-1951/$ – see front matter © 2012 Elsevier B.V. All rights reserved.
doi:10.1016/j.tecto.2012.02.019

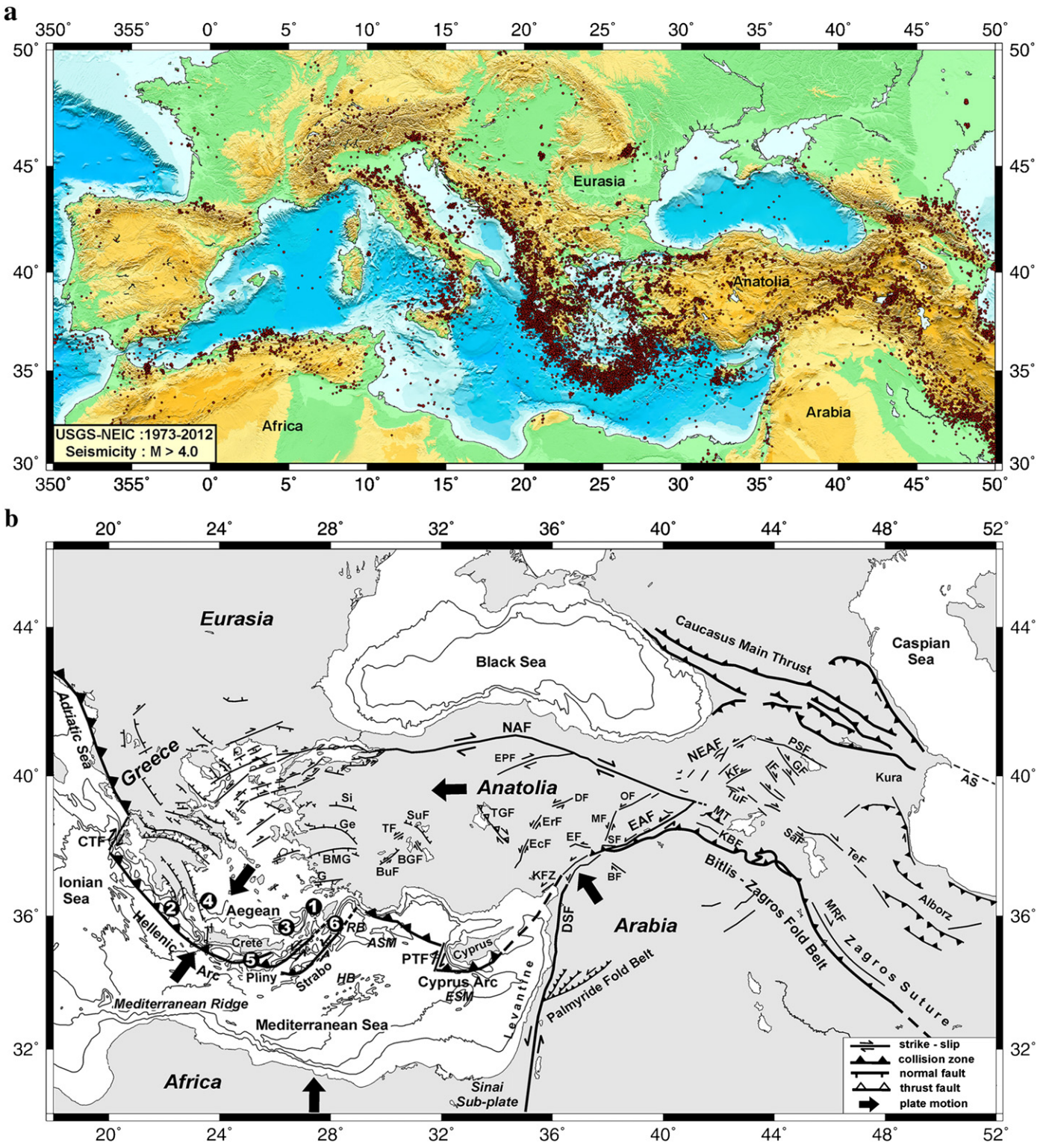

Fig. 1. (a) General view of seismicity in the Mediterranean Sea and (b) tectonic sketch map of active boundaries and main structures in the Eastern Mediterranean region, compiled from our observations and those of Mascle and Martin (1990), Taymaz et al. (1990, 1991, 2004), Şaroğlu et al. (1992), Woodside et al. (2000, 2002), Tan and Taymaz (2006), Yolsal et al. (2007), Aksu et al. (2008), Hall et al. (2008) and thereafter. AS: Apşeron Sill, ASM: Anaximander Sea Mountains, BF: Bozova Fault, BGF: Beyşehir Gölü Fault, BMG: Büyük Menderes Graben, BuF: Burdur Fault, CTF: Cephalonia Transform Fault, DSF: Dead Sea Transform Fault, DF: Deliler Fault, EAF: East Anatolian Fault, EcF: Ecemiş Fault, EF: Elbistan Fault, EPF: Ezine Pazarı Fault, ErF: Erciyes Fault, ESM: Eratosthenes Sea Mountains, G: Gökova, Ge: Gediz Graben, GF: Garni Fault, HB: Herodotus Basin, IF: Iğdır Fault, KBF: Kavakbaşı Fault, KF: Kağızman Fault, KFZ: Karataş-Osmaniye Fault Zone, MF: Malatya Fault, MRF: Main Recent Fault, MT: Muş Thrust, NAF: North Anatolian Fault, NEAF: North East Anatolian Fault, OF: Ovacık Fault, PSF: Pampak-Savan Fault, PTF: Paphos Transform Fault, RB: Rhodes Basin, SaF: Salmas Fault, Si: Simav Graben, SuF: Sultandağ Fault, TeF: Tebriz Fault, TF: Tatarlı Fault, TGF: Tuz Gölü Fault. Large black arrows show relative plate motions with respect to Eurasia (McClusky et al., 2000, 2003). Topography and bathymetry data are taken from USGS – NOAA / GTOPO30 and GEBCO-BODC (1997), respectively. Black circles with numbers represent the locations of earthquakes which are discussed as case studies in the text.

Table 1
Earthquake source parameters obtained from teleseismic P- and SH-waveform inversion. Earthquake epicenters are taken from ISC earthquake catalogue. Error limits are estimated from uncertainty tests. M_o: seismic moment, t_o: origin time, M_w: moment magnitude, h: focal depth of the earthquake. Earthquakes are classified into three major groups according to active tectonics, [1] E–W extension within overriding Aegean, [2] African–Aegean convergence, and [3] the subducting African plate.

Date (d.m.y)	Origin time (to) (h:m:s)	Lat. (°N)	Long. (°E)	Velocity model	Depth (km)			M_w	Strike (ϕ, °)	Dip (δ, °)	Rake (λ, °)	h (km)	M_o ($\times 10^{16}$ N m)	Related tectonics
					ISC	HRV	NEIC							
20.07.1996	00:00:41.57	36.13	27.05	A	26.8	15	14	6.1	210 ± 10	44 ± 5	−76° (+5, −10)	9 ± 2	204.4	1
22.02.2000	11:55:22.38	34.48	25.54	A	9.7	33	33	5.2	111 ± 10	72 ± 10	43 ± 10	7 ± 2	6.8	2
10.03.2000	22:01:45.63	34.26	26.01	A	10	15	10	5.4	140 ± 10	64 ± 10	71 ± 10	16 ± 2	14.6	2
05.04.2000	04:36:57.51	34.42	25.79	A	33	15	38	5.6	272 ± 5	36 ± 5	108 ± 5	4 ± 2	29.5	2
24.05.2000	05:40:36.05	35.97	21.99	A	19.9	38.3	33	5.5	263 (+5, −10)	58 ± 5	296 ± 10	13 ± 2	23.8	1
13.06.2000	01:43:14.69	35.12	27.06	A	9.8	15	10	5.3	43 ± 10	82 ± 10	9 ± 5	12 ± 2	9.7	1
01.05.2001	06:00:56.04	35.67	27.47	A	28.5	33	33	5.1	194 (+5, −10)	55 ± 5	−78 ± 5	10 ± 2	5.8	1
29.05.2001	04:43:57.06	35.38	27.74	A	11	46	20.7	5.0	142 ± 10	62 (+5, −10)	−137 ± 10	32 ± 2	4.6	1
23.06.2001	06:52:42.67	35.54	28.10	A	45.5	58.4	50.1	5.7	80 ± 5	87 ± 5	8 ± 10	44 ± 2	41.9	3
30.10.2001	21:00:05.41	35.86	29.77	A	5	-	51.1	5.2	102 ± 10	75 ± 10	159 ± 10	35 ± 2	9.0	3
26.11.2001	05:03:21.06	34.82	24.29	A	33	47.8	33	5.2	143 ± 10	57 ± 10	64 (+5, −10)	30 ± 2	7.2	2
22.01.2002	04:53:52.10	35.57	26.62	B	94.6	90.3	88	6.1	4 ± 5	41 ± 5	175 ± 5	82 ± 2	151.6	3
21.05.2002	20:53:30.18	36.63	24.27	B	106.7	100.4	97.1	5.8	267 ± 5	84 ± 5	180 ± 5	91 ± 2	52.7	3
06.06.2002	22:35:41.51	35.53	26.16	B	95.2	110.4	-	5.1	168 (+5, −10)	51 ± 5	5 ± 5	81 ± 2	5.1	3
12.10.2002	05:58:50.44	34.75	26.37	A	12.2	15	10	5.4	219 ± 10	29 ± 10	−4 ± 10	9 ± 2	18.0	1
17.10.2003	12:57:07.13	35.96	22.18	A	30	-	33.9	5.5	201 ± 10	13 ± 10	−30 ± 10	12 ± 2	24.8	1
07.02.2004	21:17:21.37	35.83	26.86	A	14.1	15.9	25	5.2	198 ± 10	12 ± 5	−70 ± 10	8 ± 2	6.9	1
17.03.2004	05:20:57.75	34.66	23.38	A	14.7	12	–	6.0	169 (−5, +10)	82 ± 5	8 (+5, −10)	35 ± 2	107.1	3
04.11.2004	06:22:37.56	35.96	23.14	B	70.1	92.1	-	5.1	46 ± 5	53 (−5,+10)	117 ± 10	67 ± 2	4.8	3
23.01.2005	22:36:07.39	35.84	29.66	A	42.4	24	10	5.6	128 ± 5	82 ± 5	149 ± 5	34 ± 2	35.6	3
30.01.2005	16:23:49.69	35.80	29.71	A	43	21.8	10	5.4	178 ± 10	69 ± 5	5 ± 5	27 ± 2	18.2	3
08.01.2006	11:34:54.64	36.27	23.26	B	58.4	64	66	6.5	62 (−5, +10)	57 ± 5	121 (+5, −10)	60 ± 2	825.5	3
03.02.2007	13:43:22.50	35.80	22.48	B	53	53.5	59.1	5.3	194 ± 5	71 ± 5	19 ± 10	57 ± 2	12.4	3
28.03.2008	00:16:20.54	34.79	25.34	A	48.9	59.1	45	5.5	242 (+5, −10)	24 ± 5	53 ± 5	44 ± 2	18.6	2
15.07.2008	03:26:36.55	35.92	27.80	B	64.9	35.5	52	6.1	94 ± 5	80 ± 5	30 ± 5	50 ± 2	204.9	3

boundaries such as Hellenic and Cyprus arcs in the past, and emphasized the importance of numerical tsunami simulation studies on estimating tsunami wave characteristics on coastal regions.

The Hellenic subduction zone, which is our study area, plays an important role on the evolution of the active tectonics of the Eastern Mediterranean region. Seismological observations along this zone are widely used to get a better understanding of tectonic processes and recent deformations. For example, the crustal and lithospheric structures have been hitherto examined by receiver functions, tomography studies, Rayleigh wave phase velocities, focal mechanism solutions and wide aperture seismic data (e.g., Benetatos et al., 2004; Biryol et al., 2011; Bohnhoff et al., 2001; Endrun et al., 2004; Karagianni et al., 2005; Spakman et al., 1988; Taymaz et al., 1990, 1991; Wortel and Spakman, 1992). They revealed a subducting slab that dips to the north beneath Crete. Further, GPS surveys (Cocard et al., 1999; Le Pichon et al., 1995; McClusky et al., 2000, 2003; Nyst and Thatcher, 2004; Reilinger et al., 2010; Skarlatoudis et al., 2009) provided crucial evidences to large-scale kinematics and movement patterns in the region. The overall rate of convergence was found as ~4 cm/year along the Hellenic subduction zone (McClusky et al., 2000). A well-developed Benioff zone was also identified by using earthquake activity to a depth of 150–180 km below the central Aegean (Papazachos et al., 2000) and the subducting lithosphere was followed down to about 1200 km by seismic

Table 2
Source region velocity–depth models used in teleseismic body waveform inversions. Velocity models are compiled from Makris and Stobbe (1984), Makris et al. (1983) and Taymaz et al. (1990).

Velocity model	Vp (km/s)	Vs (km/s)	Density (g/cm^3)	Thickness (km)
A (for shallow and intermediate earthquakes)	4.50	2.59	2.42	<10
	6.80	3.91	2.91	Half-space
B (for deep earthquakes)	6.50	3.70	2.8	>25
	7.80	4.50	3.3	Half-space

Table 3
Dynamic and kinematic earthquake source parameters obtained from inversions of slip distributions on fault planes. M_o: seismic moment, τ: total source duration, L: fault length, W: fault width, S: faulting area, D_{max}: maximum displacement, D_{av}: average displacement, △σ: stress drop.

Date (d.m.y.)	M_o ($\times 10^{16}$N m)	τ (s)	L (km)	W (km)	S (km^2)	D_{max} (cm)	D_{av} (cm)	△σ (bar)
20.07.1996	196.3	8–10	20	14	280	130	23.3	10
05.04.2000	38.2	6–8	11	10	110	40	11.5	8
24.05.2000	25.1	4	10	10	100	20	8.3	6
13.06.2000	12.3	2	5	5	25	50	16.4	24
01.05.2001	4.4	3	6.5	5.5	36	20	4.13	5
23.06.2001	34.3	6	15	12	180	10	6.3	4
22.01.2002	218.2	8	10	15	150	50	48	29
21.05.2002	52.8	4–8	8	11	88	30	20.0	16
06.06.2002	6.3	2	5	5	25	10	8.5	12
12.10.2002	16.7	10–12	15	14	210	10	6.2	1
17.03.2004	166.7	4–6	12	9	108	80	51.4	37
23.01.2005	41.6	4	8	11	88	20	15.77	12
08.01.2006	1056	6	24	24	576	120	61.1	19
03.02.2007	16.2	2	5.5	5.5	30.25	20	17.8	24
28.03.2008	28.8	3–6	6	10	60	20	16.3	15
15.07.2008	291.3	3–6	12	16	192	100	50.5	27

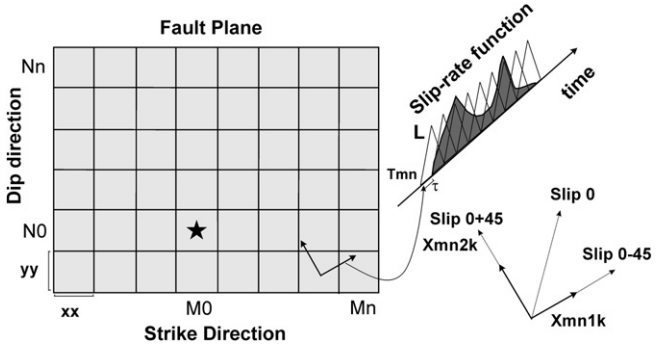

Fig. 2. Schematic representation of faulting area in slip distribution inversion. The star shows the initial break of rupture propagation. The rupture in each cell starts after T_{mn} time delay. Slip rate function is defined by L isosceles triangles with a rise time τ in seconds. Two components of slip vector with rakes slip 0 ± 45° (Tan and Taymaz, 2006; Yagi and Kikuchi, 2000; Yagi et al., 2004; Yolsal, 2008).

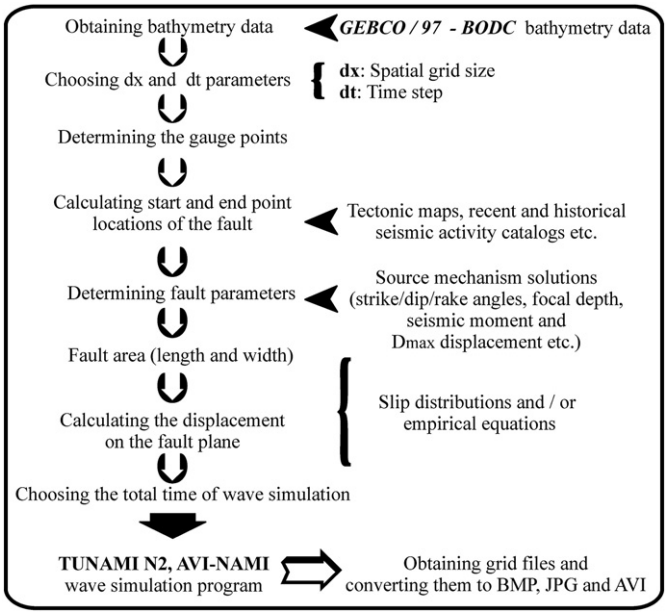

Fig. 3. Flow chart of processing steps in tsunami simulations (Imamura, 1995, 1996; Yalçıner et al., 2004; Yolsal, 2008).

tomography (Bijwaard and Spakman, 1998; Spakman et al., 1988). The Global CMT and other moment tensor catalogues, and earthquake source studies exhibited variety of faulting mechanisms in the region. For example, Taymaz et al. (1990) studied earthquake source mechanisms and classified them into four groups: [1] normal faults with a N–S strike in the overriding material above the subduction zone; [2] low-angle thrusts with an E–W strike at a depth of about 40 km; [3] high-angle reverse faults with shallow focal depths, and [4] earthquakes within the subducting lithosphere with approximately E–W P-axes. Benetatos et al. (2004) also found that the outer part of the Hellenic Arc, starting south of Zante Island and up to the coast of Turkey, is deforming through high-angle reverse and low-angle thrust faulting by studying earthquakes whose focal depths do not exceed ~40 km. They found NE–SW directed P-axes which are perpendicular to the trench in the western part and parallel to it in the eastern part. However, for deeper earthquakes ($h > 40$ km), they determined strike–slip faulting mechanisms with considerable amount of thrust components at the western and eastern edges of the Hellenic arc. Similarly, Bohnhoff et al. (2005) concluded that slab-pull is the dominant force within the subduction process, and it is responsible for the roll-back of the Hellenic arc. Recently, Shaw and Jackson (2010) suggested that the downgoing African plate deforms by arc-parallel contraction at all depths, and T-axes directions align down-dip within the descending slab. They also addressed the kinematic questions which are related to the eastern termination of the Hellenic subduction zone. Furthermore, Lorito et al. (2008) studied historical tsunamigenic earthquakes, constrained specifically rake angles of fault planes by using maps of principal stress and strain axes and GPS velocity fields.

It is well-known that tsunami waves are generally occurred when a destructive earthquake ($M > 7.0$) shows dip-slip mechanisms (i.e. normal or thrust faulting). Therefore, most of tsunami waves have been observed along oceanic trenches and shallow parts of subduction zones where convergent motions and large dip-slip (vertical) displacements are dominantly seen (Bilek, 2009; Bryant, 1991). The December 26, 2004 Sumatra earthquake (M_w~9.3) and related tsunami is one of the best examples of catastrophic earthquakes which occurred as a result of subduction process between Indo-Australian and Eurasian Plates in recent years. Due to the existence of several tsunamigenic zones in the Eastern Mediterranean, we highlighted the importance of numerical tsunami simulation studies on estimating tsunami wave propagations and wave amplitudes along the coastal locations.

The goal of this article is to study recent earthquakes, active deformations, kinematic and dynamic source parameters along the Hellenic subduction zone, and illustrate potential tsunamigenic sources in the Eastern Mediterranean region. Thus, source mechanisms, slip distributions and rupture propagations on fault planes of 25 earthquakes ($M_w \geq 5.0$; 2000–2008; Table 1) are analyzed. We specifically focus on earthquakes near Crete and Dodecanese (22°–29°N and 32°–36.5°E) Islands. Other Aegean earthquakes (e.g., Gulf of Gökova) will be discussed in elsewhere. Major extended tsunamigenic zones such as Hellenic and Cyprus arcs, Dodecanese islands and Levantine Basin are examined in order to understand the tsunami potential in the Eastern Mediterranean region.

2. Material and methods

In this section we briefly explained the methods of teleseismic waveform modeling and numerical tsunami simulations used in the present study.

2.1. Teleseismic body waveform inversion

Determination methods of source mechanisms aim at adjusting earthquake source parameters such as strike (ϕ), dip (δ) and rake (λ) angles of fault plane, focal (centroid) depth (h), source time function (STF) and seismic moment (M_o). They are commonly applied to earthquakes with $M_w > 5.0$ along with observations recorded at teleseismic distances ($30° \leq \Delta \leq 90°$). In this study, we used teleseismic P- and SH-body waveforms and MT5 inversion algorithm developed by McCaffrey and Abers (1988) and Nàbělek's (1984). This method is based on the weighted least-square sense and obtaining the minimum misfit between observed and synthetic seismograms (Benetatos et al., 2004; Jackson et al., 2002; Maggi et al., 2000; McCaffrey et al., 1991; Shaw and Jackson, 2010; Tan and Taymaz, 2006; Taymaz, 1990, 1996; Taymaz et al., 1990, 1991, 2007a, 2007b; Yolsal, 2008). Earthquake data were retrieved from Global Digital Seismographic Network (GDSN) of the Incorporated Research Institute of Seismology (IRIS). Both teleseismic long period (LP) P-, SH- and broad band (BB) P-waveforms were used. All records were converted to the displacement from velocity by de-convolving responses and then re-convolving them with the response of the WWSSN 15–100 long period instruments. We did not apply any filtering to the waveforms. Earthquake source was constrained to be double-couple. Synthetic waveforms were formed by combining direct P- and SH-waves with surface reflections pP, sP, and sS. Amplitudes were adjusted for geometrical spreading, and for attenuation using Futterman's (1962) operator, with $t^* = 1$ s for P- and $t^* = 4$ s for SH-waves. This method assumes that earthquake source can be represented as a point in space, although not in time. Time history of the displacement on the fault was represented by a source time function, described by a series of overlapping isosceles triangles, whose number and duration we defined. The best inversion result is referred to as the "minimum misfit solution". However, it is known that the covariance matrix associated with the minimum misfit solution usually underestimates the true uncertainties associated with source parameters. Hence, we followed the procedure described by Molnar and Lyon-Cáen (1989), Nelson et al. (1987), Tan and Taymaz (2006) and Taymaz et al. (1990, 1991) in which the inversion routine was used to perform experiments to test the robustness of the minimum misfit solutions. We looked into one parameter at a time by fixing it at a series of values either side of its value yielded by the minimum misfit solution, and allowing the other parameters to be found by the inversion routine. Then, we visually examined the quality of fitting between observed and synthetic seismograms to notice if it had deteriorated from the minimum misfit solution. In this way, we found the uncertainties in strike, dip and rake angles to be ± 5°–10°, and of focal depths to be ± 2 km

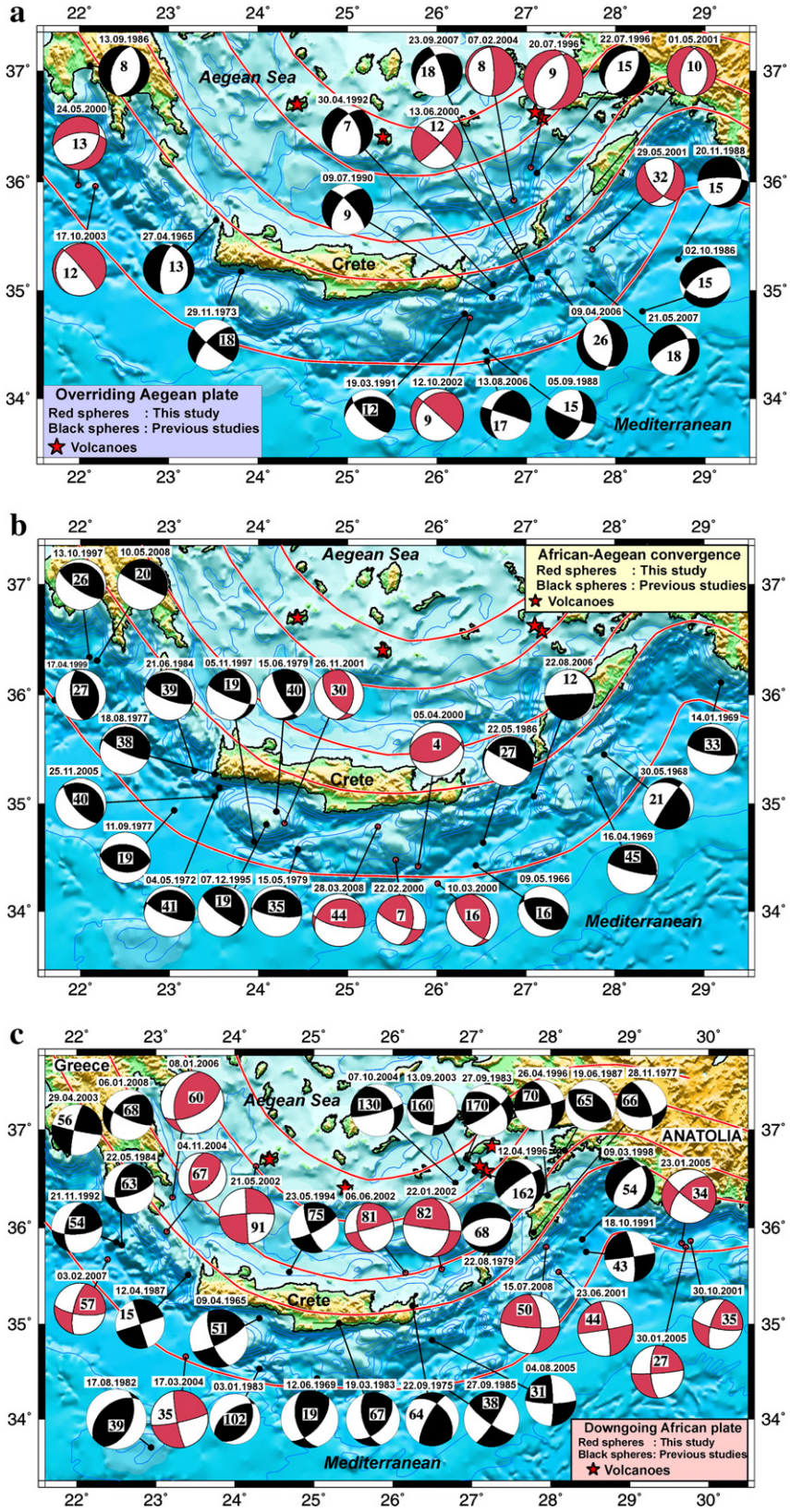

Fig. 4. a. Earthquake source mechanism solutions ($M_w \geq 5.0$) exhibiting E–W extension within the overriding Aegean plate. Red and black focal spheres present mechanisms obtained by this study and previous source studies (Table A1), respectively. Stars indicate volcanoes (Smithsonian Institute) and red continues lines are representative of elongation of the Hellenic subduction zone (Gudmundsson and Sambridge, 1998).b. Earthquake source mechanism solutions ($M_w \geq 5.0$) related to the African–Aegean convergence. Red and black focal spheres present mechanisms obtained by this study and previous source studies (Table A2), respectively. Stars indicate volcanoes (Smithsonian Institute) and red continues lines are representative of elongation of the Hellenic subduction zone (Gudmundsson and Sambridge, 1998).c. Earthquake source mechanism solutions ($M_w \geq 5.0$) concerned with the downgoing African plate. Red and black focal spheres present mechanisms obtained by this study and previous source studies (Table A3), respectively. Stars indicate volcanoes (Smithsonian Institute) and red continues lines are representative of elongation of the Hellenic subduction zone (Gudmundsson and Sambridge, 1998).

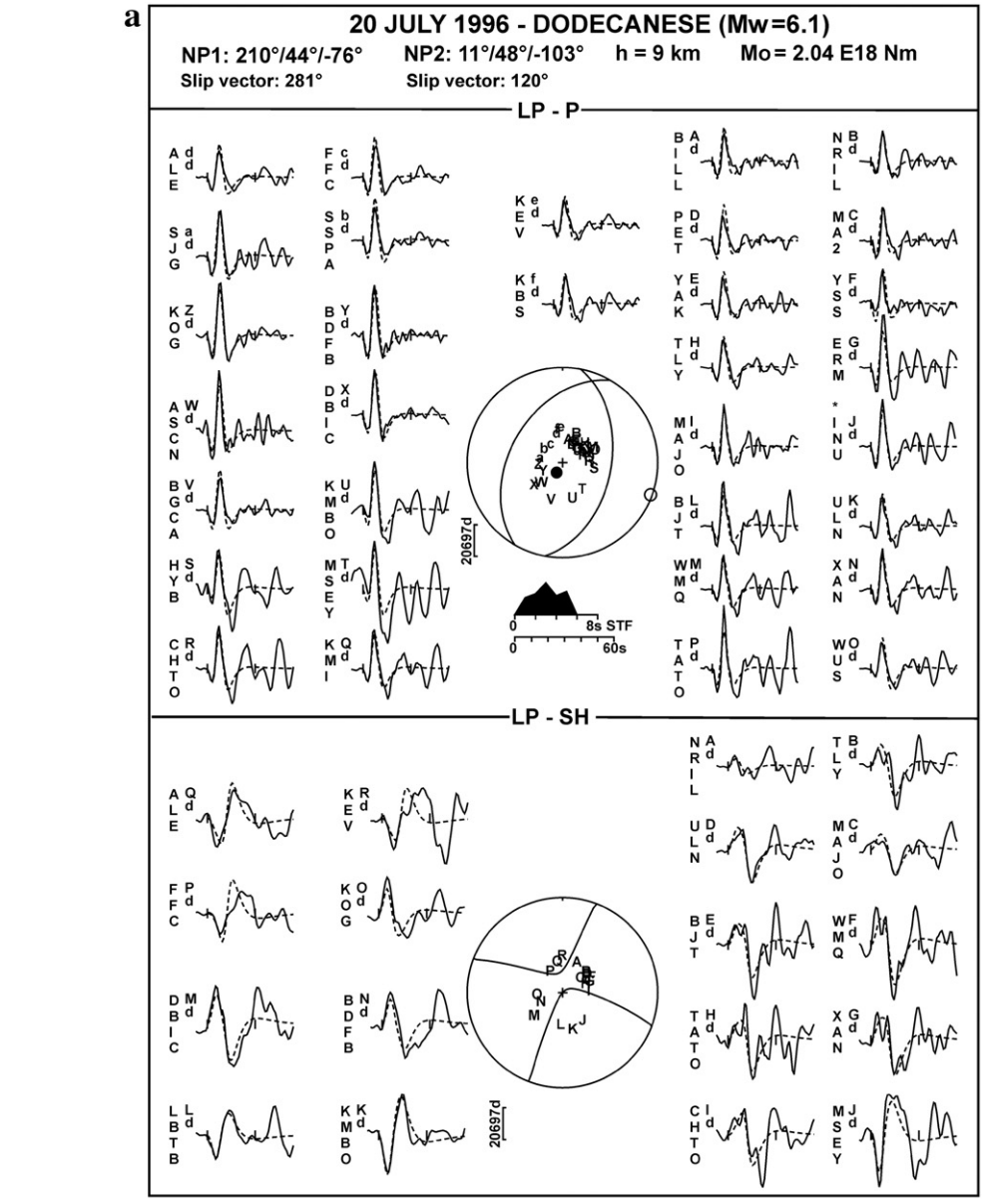
a
20 JULY 1996 - DODECANESE (Mw=6.1)
NP1: 210°/44°/-76° NP2: 11°/48°/-103° h = 9 km Mo= 2.04 E18 Nm
Slip vector: 281° Slip vector: 120°
LP - P
LP - SH
20697d
0 8s STF
0 60s

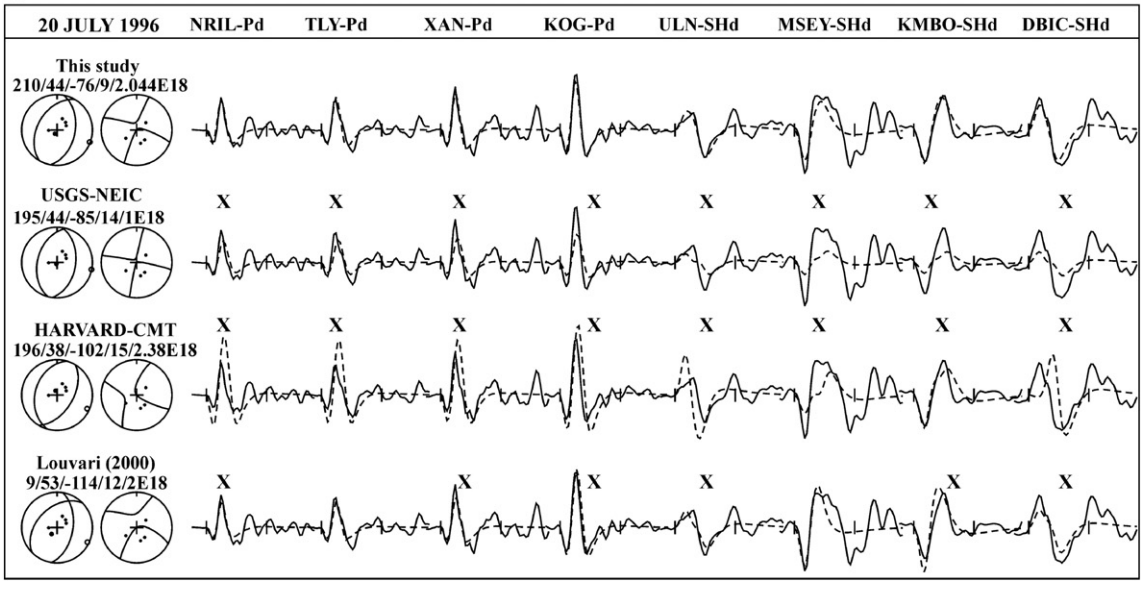
b
20 JULY 1996
NRIL-Pd
TLY-Pd
XAN-Pd
KOG-Pd
ULN-SHd
MSEY-SHd
KMBO-SHd
DBIC-SHd
This study
210/44/-76/9/2.044E18
USGS-NEIC
195/44/-85/14/1E18
HARVARD-CMT
196/38/-102/15/2.38E18
Louvari (2000)
9/53/-114/12/2E18

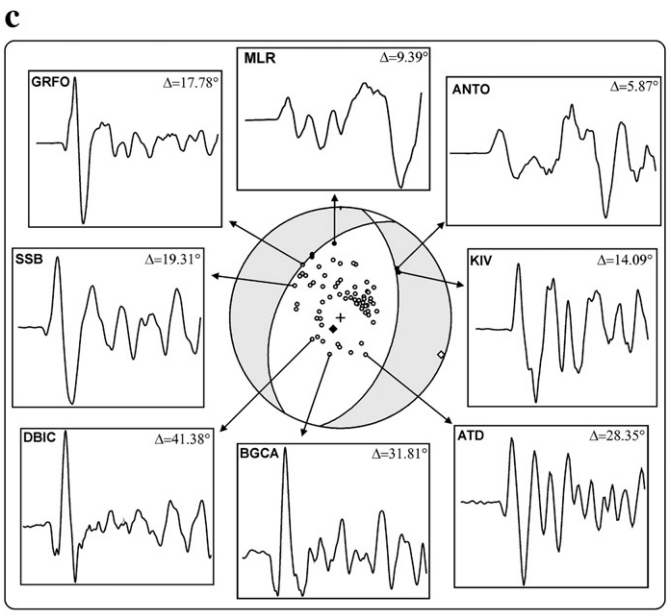
c
GRFO Δ=17.78°
MLR Δ=9.39°
ANTO Δ=5.87°
SSB Δ=19.31°
KIV Δ=14.09°
DBIC Δ=41.38°
BGCA Δ=31.81°
ATD Δ=28.35°

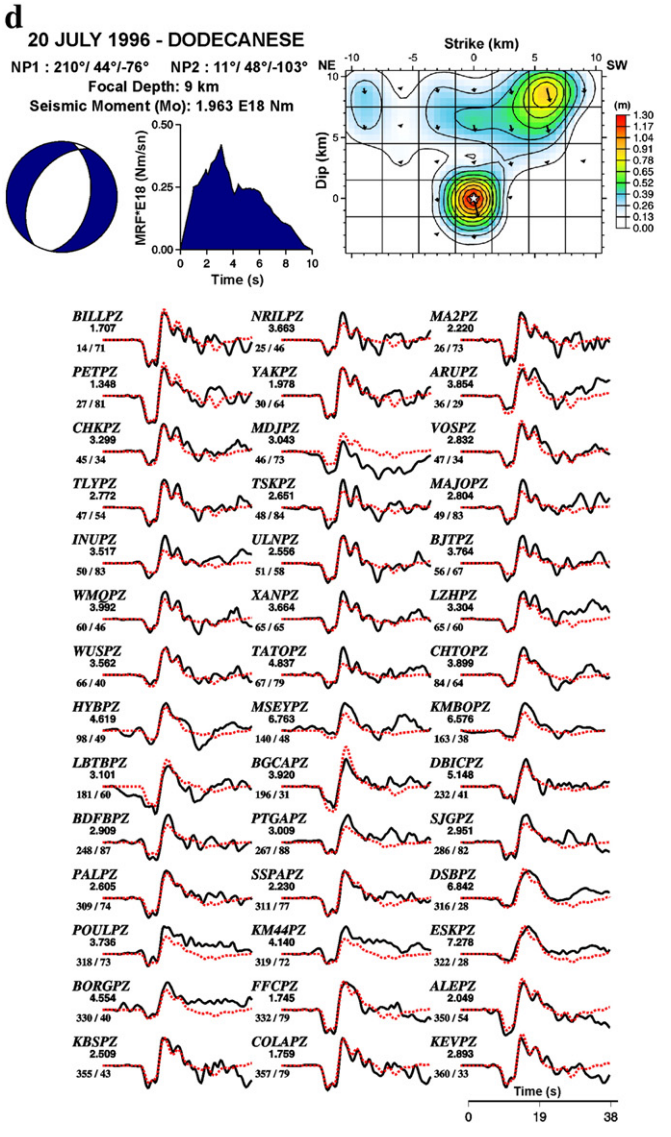
d
20 JULY 1996 - DODECANESE
NP1 : 210°/ 44°/-76° NP2 : 11°/ 48°/-103°
Focal Depth: 9 km
Seismic Moment (Mo): 1.963 E18 Nm
MRF*E18 (Nm/sn)
Time (s)
Strike (km)
Dip (km)
NE
SW
(m)
BILLPZ 1.707 14 / 71
NRILPZ 3.663 25 / 46
MA2PZ 2.220 26 / 73
PETPZ 1.348 27 / 81
YAKPZ 1.978 30 / 64
ARUPZ 3.854 36 / 29
CHKPZ 3.299 45 / 34
MDJPZ 3.043 46 / 73
VOSPZ 2.832 47 / 34
TLYPZ 2.772 47 / 54
TSKPZ 2.651 48 / 84
MAJOPZ 2.804 49 / 83
INUPZ 3.517 50 / 83
ULNPZ 2.556 51 / 58
BJTPZ 3.764 56 / 67
WMQPZ 3.992 60 / 46
XANPZ 3.664 65 / 65
LZHPZ 3.304 65 / 60
WUSPZ 3.562 66 / 40
TATOPZ 4.837 67 / 79
CHTOPZ 3.899 84 / 64
HYBPZ 4.619 98 / 49
MSEYPZ 6.783 140 / 48
KMBOPZ 6.576 163 / 38
LBTBPZ 3.101 181 / 60
BGCAPZ 3.920 196 / 31
DBICPZ 5.148 232 / 41
BDFBPZ 2.909 248 / 87
PTGAPZ 3.009 267 / 88
SJGPZ 2.951 286 / 82
PALPZ 2.605 309 / 74
SSPAPZ 2.230 311 / 77
DSBPZ 6.842 316 / 28
POULPZ 3.736 318 / 73
KM44PZ 4.140 319 / 72
ESKPZ 7.278 322 / 28
BORGPZ 4.554 330 / 40
FFCPZ 1.745 332 / 79
ALEPZ 2.049 350 / 54
KBSPZ 2.509 355 / 43
COLAPZ 1.759 357 / 79
KEVPZ 2.893 360 / 33
Time (s)

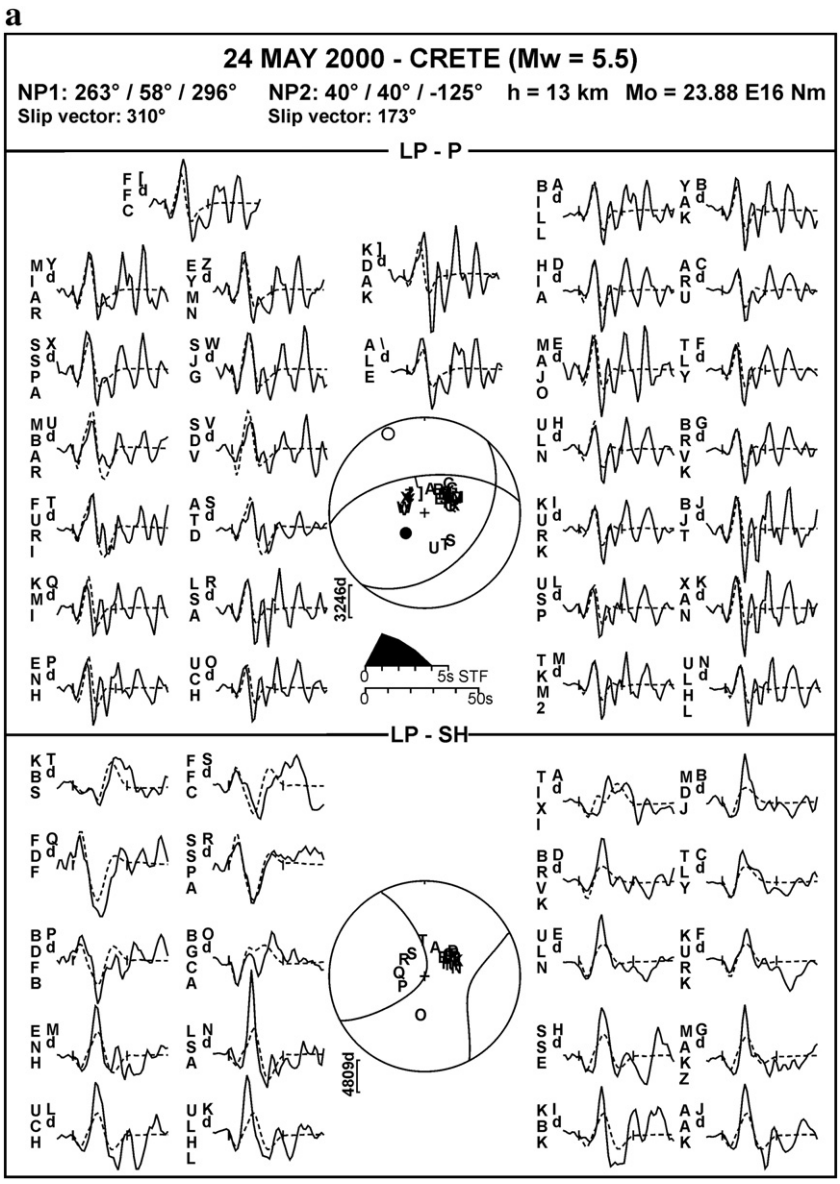

Fig. 6. a. Minimum misfit solution of the May 24, 2000 Crete earthquake (M_w: 5.5) determined by teleseismic long period P- and SH-waveform inversion. Header information is as in Fig. 5a.b. Focal mechanism, co-seismic slip distribution and total moment rate function of the May 24, 2000 earthquake and comparison of the observed (black) and synthetic (red) broad band P-waveforms used in slip distribution inversion. Header information is as in Fig. 5d.

depending on azimuthal distribution of stations and signal quality of waveforms. We estimated accurate earthquake focal depths (± 2 km) which were not well determined by moment tensor catalogues such as Harvard-CMT (Harvard University), USGS-NEIC (United States Geological Survey), ERI-CMT (Earthquake Research Institute), KOERI (Kandilli Observatory and Earthquake Institution), MEDNET-INGV (Mediterranean Network) and ETHZ-SED (Swiss Federal Institute of Technology Zurich). However, it is well-known that focal depths are essential in understanding the tectonic structure and seismogenic zone of a region and in better acquiring the

Fig. 5. a. Minimum misfit solution of the July 20, 1996 Dodecanese earthquake (M_w: 6.1) determined by teleseismic long period P- and SH-waveform inversion. The strike, dip, rake angles and slip vector azimuth of the first and second nodal planes (NP), focal depth (h) and seismic moment (M_o) are given. Observed and synthetic waveforms are shown by solid and dashed lines, respectively. The source time function (STF) is shown in the middle of the figure, and beneath it is the time scale used for the waveforms. Focal spheres are shown with P- (top) and SH- (bottom) nodal planes in lower hemisphere projection. Station positions are indicated by letter and are arranged alphabetically clockwise, starting from north. The P- and T-axes are marked by solid and open circles, respectively. * exhibit waveforms not used in inversion.b. Comparison of our minimum misfit solution with the source parameters reported by USGS-NEIC, Harvard-CMT catalogues and Louvari (2000). The top row shows waveforms from the minimum misfit solution. The stations are identified at the top of each column, with the type of waveform marked by P- and SH- and followed by the instrument type. At the start of each row are the P- and SH-focal spheres for the focal parameters represented by the five numbers (strike, dip, rake, depth and seismic moment), showing the positions on the focal spheres of the stations chosen. X show matches of observed to synthetic waveforms that are worse than in the minimum misfit solution.c. Distribution of P-wave first motion polarities of the July 20, 1996 earthquake recorded by seismic stations at teleseismic and regional distances. Lower hemisphere equal area projections are used. The station positions have been plotted with the same velocity model beneath the source used in our minimum misfit solution. Both nodal planes are those of the minimum misfit solution. Station names and epicentral distances are given near example waveforms. Filled circles are compressional first motions, opens are dilatational. First motions are only used here to examine the nodal planes constrain.d. Focal mechanism, co-seismic slip distribution and total moment rate function of the April 05, 2000 earthquake and comparison of the observed (black) and synthetic (red) broad band P-waveforms used in slip distribution inversion. The strike, dip and rake angles of the first and second nodal planes (NP) and focal depth (h) obtained from minimum misfit solution are given in the header. The white star indicates the focal depth obtained from minimum misfit solution. Station code and maximum amplitude are above the waveforms, station azimuth and distance below. The vertical scale given on the right-hand side shows the displacement values in meters.

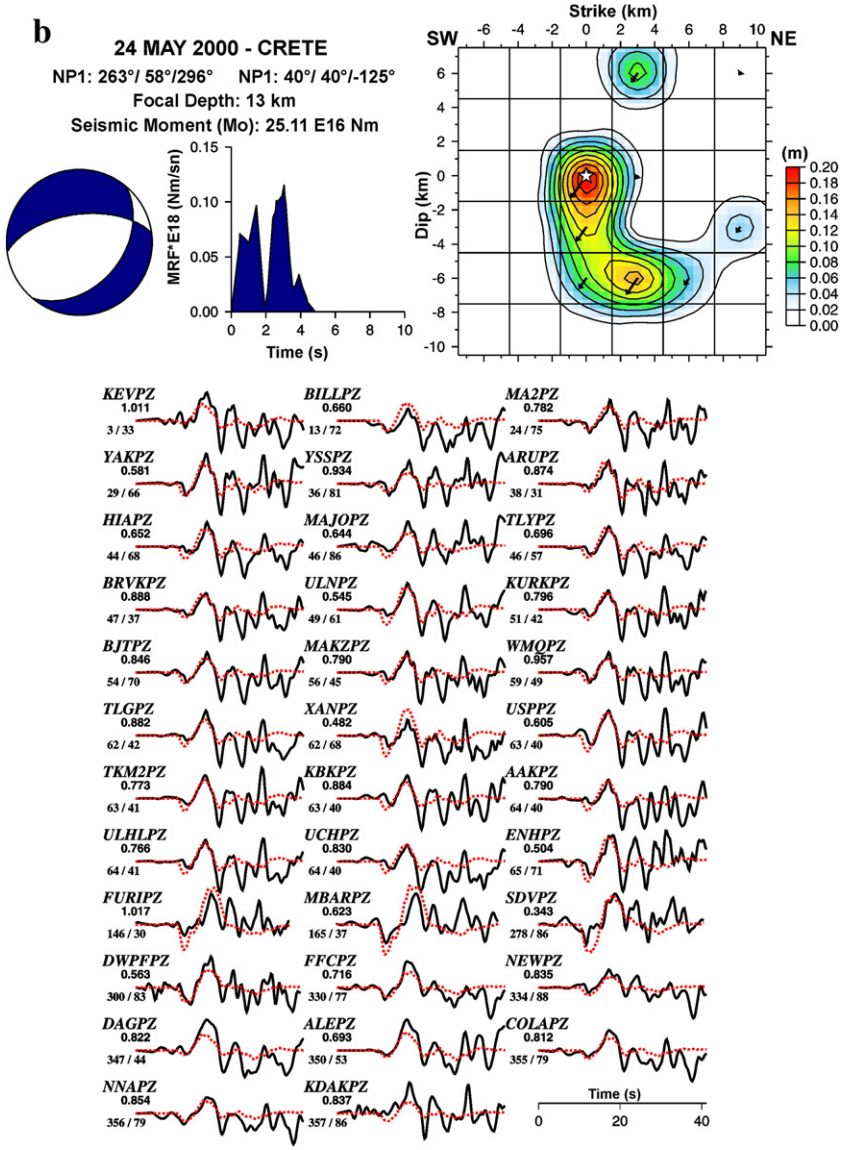

Fig. 6 (*continued*).

evaluation of earthquake hazard. Another important point is to be used appropriate velocity–depth structure at source, since the uncertainty in the velocity structure leads directly to an uncertainty in focal depth. We used a velocity–depth model at source reported by Makris and Stobbe (1984), Taymaz (1996), Taymaz et al. (1990) for our study area. Furthermore, for each sub-sea earthquakes, we added an overlying water layer of variable thickness depending on the earthquake epicenter and GEBCO-BODC (1997) bathymetry data (Smith and Sandwell, 1997a,b; Table 2). We also calculated earthquake moment magnitudes by using seismic moment (M_o) and Kanamori (1977) equation for all earthquakes.

2.2. Slip distribution and rupture propagation

Slip distribution inversions have been mostly used to reveal the earthquake source characteristics. We obtained rupture histories and slip distributions on fault planes of 16 earthquakes (Table 3) by using the slip inversion scheme given by Yagi and Kikuchi (2000) and Yoshida (1992). Initially, waveforms were windowed for 60 s, starting 10 s before the origin time. After band-pass filtering between 0.01 Hz and 1.0 Hz, all records were converted into ground displacement with a sampling time of 0.25 s as described by previous studies (e.g. Tan and Taymaz, 2006; Yagi and Kikuchi, 2000; Yagi et al., 2004). We assumed that faulting occurs on a single fault plane, and slip angle remains unchanged during the rupture. The rupture process were presented as a spatio-temporal slip distribution on a fault plane which was divided into M × N sub-faults with length *dx* and width *dy*. Then, slip rate function on each sub-fault was described by a series of triangle functions with a rise time (Fig. 2). To calculate Green's functions for teleseismic body waves, the method of Kikuchi and Kanamori (1991) were used. Arrival times were determined by using the Jeffreys–Bullen travel time table (Jeffreys and Bullen, 1940). Since increasing number of model parameters may cause the instability in inversion, we applied smoothing constraints to slip distributions with respect to time and space to prevent it.

Slip distribution models also help us calculate dimensions of faulting area (fault length and width), stress drop ($\Delta\sigma$), average (D_{av}) and maximum displacement (D_{max}) of earthquakes (Table 3). Furthermore, the recognition of irregular motions and the roughness of faulting surfaces such as asperities and barriers can be achieved. We choose a nodal plane which is consistent with the general geology, GPS motions and tectonic background of the region as a fault plane. Further, we tested the effects of choosing the accurate nodal plane by applying slip inversions using both alternative nodal plane parameters. We observed

differences mainly in rupture propagation directions and seismic moment values. But, maximum and average displacement values did not alter significantly. We also found different seismic moment (M_o) values from minimum misfit solutions and slip distribution models for the same earthquake. It is simply due to the usage of different seismic stations, type of the waveforms and variation in frequency contents of long period and broad band seismograms. For example, while obtaining source mechanism solutions we used long period P- and SH-waveforms, but for slip inversions we could only use broad-band P-waveforms due to the principle of inversion codes used in this study. The variation in seismic moment (M_o) slightly affects earthquake moment magnitude values. Further details can be found in the relevant studies done by Fukahata et al. (2003), Hartzell and Heaton (1983), Tan and Taymaz (2006), Yagi and Fukahata (2011), Yagi and Kikuchi (2000), Yagi et al. (2004), Yolsal (2008) and Yoshida (1992).

2.3. Numerical tsunami simulations

Several mathematical models mainly based on the resolution of bathymetry data and selected source model are developed in order to identify tsunami wave characteristics. It is critical to advance the capability of modeling tsunamis for the purposes of predicting arrival times, water surface fluctuations and describing wave interactions with bathymetrical structures. Faulting geometry (source depth, strike, dip, rake angles), amount of slip on the centroid and fault surface, fault area, seismic moment (energy), location (distance from shore and focal depth) and beach geometry (water depth and beach slope) are basic parameters for setting tsunami source model. First of all, it involves accurate estimation of the earthquake epicenter. Source parameters are vital to set initial and boundary conditions and to calculate the deformation of sea bottom, which in turn yields

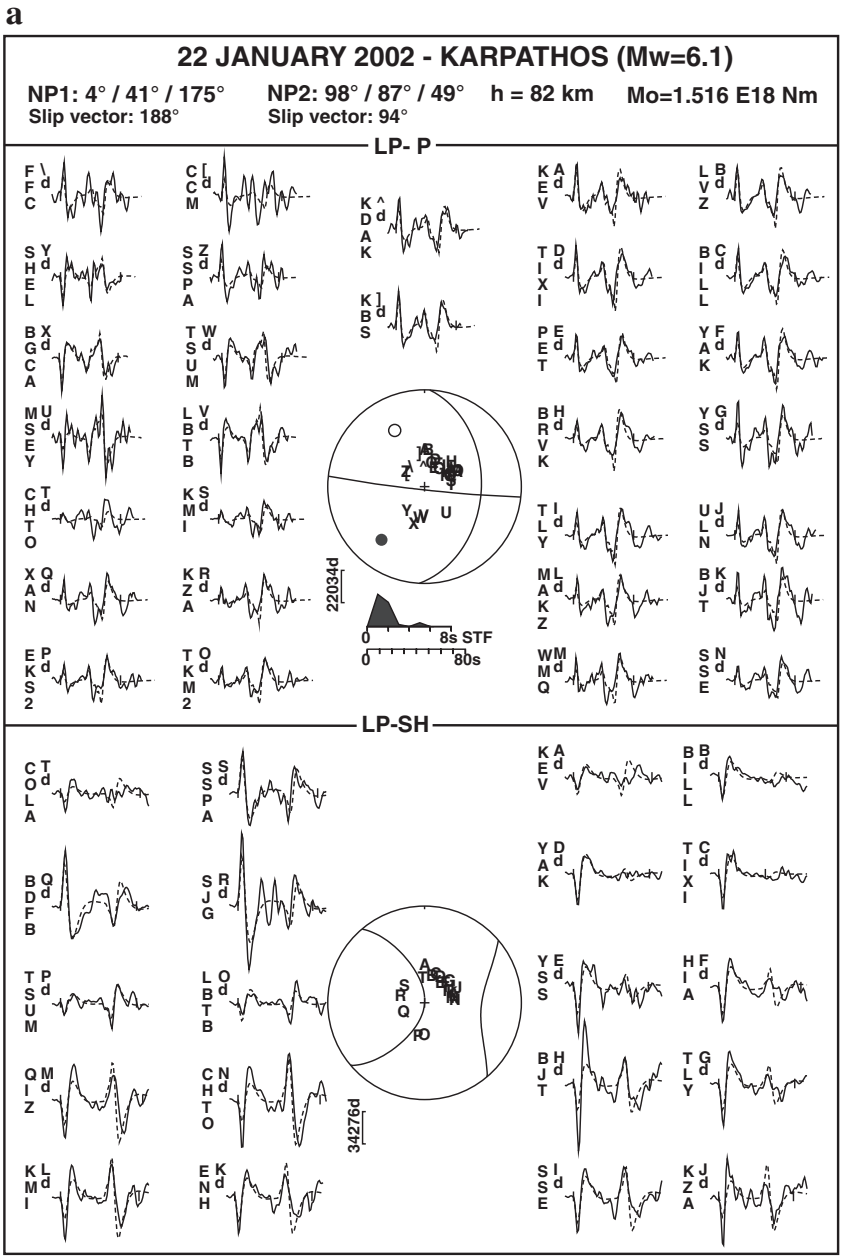

Fig. 7. a. Minimum misfit solution of the January 22, 2002 Karpathos earthquake (M_w: 6.1) determined by teleseismic long period P- and SH-waveform inversion. Header information is as in Fig. 5a.b. Focal mechanism, co-seismic slip distribution and total moment rate function of the January 22, 2002 earthquake and comparison of the observed (black) and synthetic (red) broad band P-waveforms used in slip distribution inversion. Header information is as in Fig. 5d.

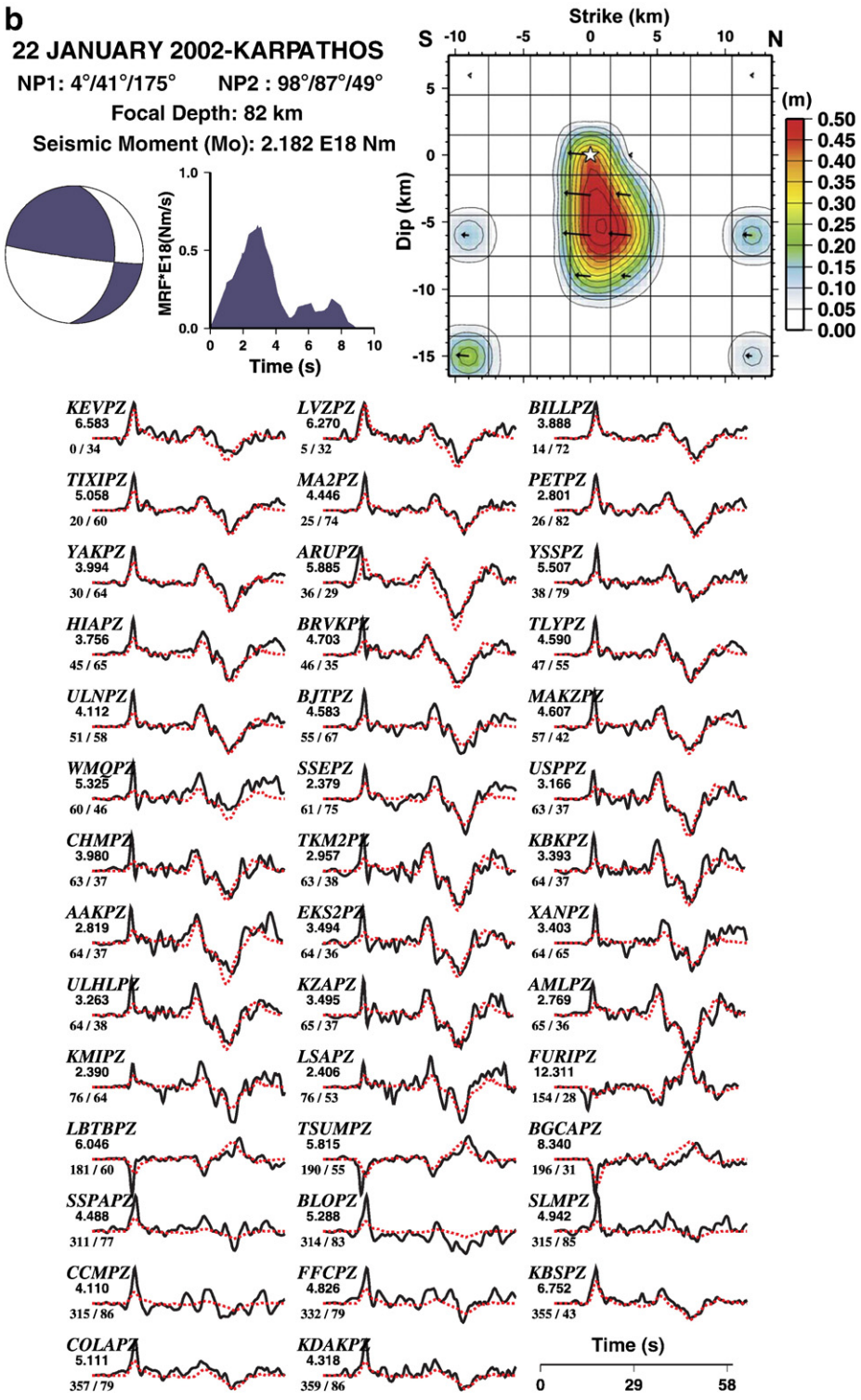

Fig. 7 (*continued*).

initial tsunami waveform (Geist, 2005; Gica et al., 2007; Yolsal and Taymaz, 2010). However, it could be sometimes hard due to the lack of verified catalogues, records and knowledge of historical earthquakes. Here, we used non-linear shallow water mathematical models (TUNAMI-N2 and AVI-NAMI) based on elastic dislocations of Okada (1985) and a given GEBCO-BODC (1997) bathymetry data (~1000 m and 2000 m grid). We calculated the generation, propagation and coastal amplifications of tsunami waves (Fig. 3). Related equations of mass conservation and momentum in three dimensions can be found in Goto et al. (1997), Imamura (1995, 1996) and Shuto et al. (1990). These numerical codes solve the governing equations by the finite difference technique with leap-frog scheme (Yalçıner et al., 2004; Yolsal, 2008; Yolsal and Taymaz, 2010; Yolsal et al., 2007). Water surface fluctuations and velocities at all locations can be computed even at shallow and land regions (Imamura, 1996) within the limitations of grid size. Time steps were adjusted as satisfying the CFL (Courant–Friedrichs–Lewy) stability condition. As an initial condition, the vertical displacement of water surface was

considered to be the same as the bottom deformation (Mansinha and Smylie, 1971). Non-linearity becomes important in many dynamic aspects when tsunami waves approach the shore. A typical Manning's bottom friction coefficient value of 0.025 was used. Details of numerical simulation steps (Fig. 3) are explained by Yalçıner et al. (2004); Yolsal (2008) and Yolsal et al. (2007).

3. Results

3.1. Earthquake source mechanisms and slip distributions

We have studied source mechanisms and rupture/slip distributions of 25 moderate earthquakes ($M_w \geq 5.0$; 2000–2008) occurred in the Eastern Mediterranean. However, among these earthquakes, one of them occurred on July 20, 1996 which we have included for its significance. Source mechanism solutions of all earthquakes are summarized in Fig. 4a,b,c and source parameters are listed in Tables 1, 3 and A1–A3. As case studies, we presented teleseismic waveform inversion results of only 6 Eastern Mediterranean earthquakes sampling different parts of the Hellenic subduction zone (Fig. 1b); June 20, 1996 Dodecanese (M_w: 6.1), May 24, 2000 Crete (M_w: 5.5), January 22, 2002 Karpathos (M_w: 6.1), January 08, 2006 Kythira (M_w: 6.5), March 28, 2008 Crete (M_w: 5.5) and July 15, 2008 Dodecanese (M_w: 6.1). Azimuthal distributions of teleseismic stations are mostly good enough to find the earthquake source parameters with minimum errors. In waveform inversion figures, straight and dashed lines are observed and synthetic waveforms, respectively. Strike, dip and rake angles are shown for both nodal planes (NP). M_o, h, and sv refer to seismic moment, focal depth and slip vector azimuth, respectively. The station code is shown to the left of each waveform, together with an upper-case letter that identifies its position on

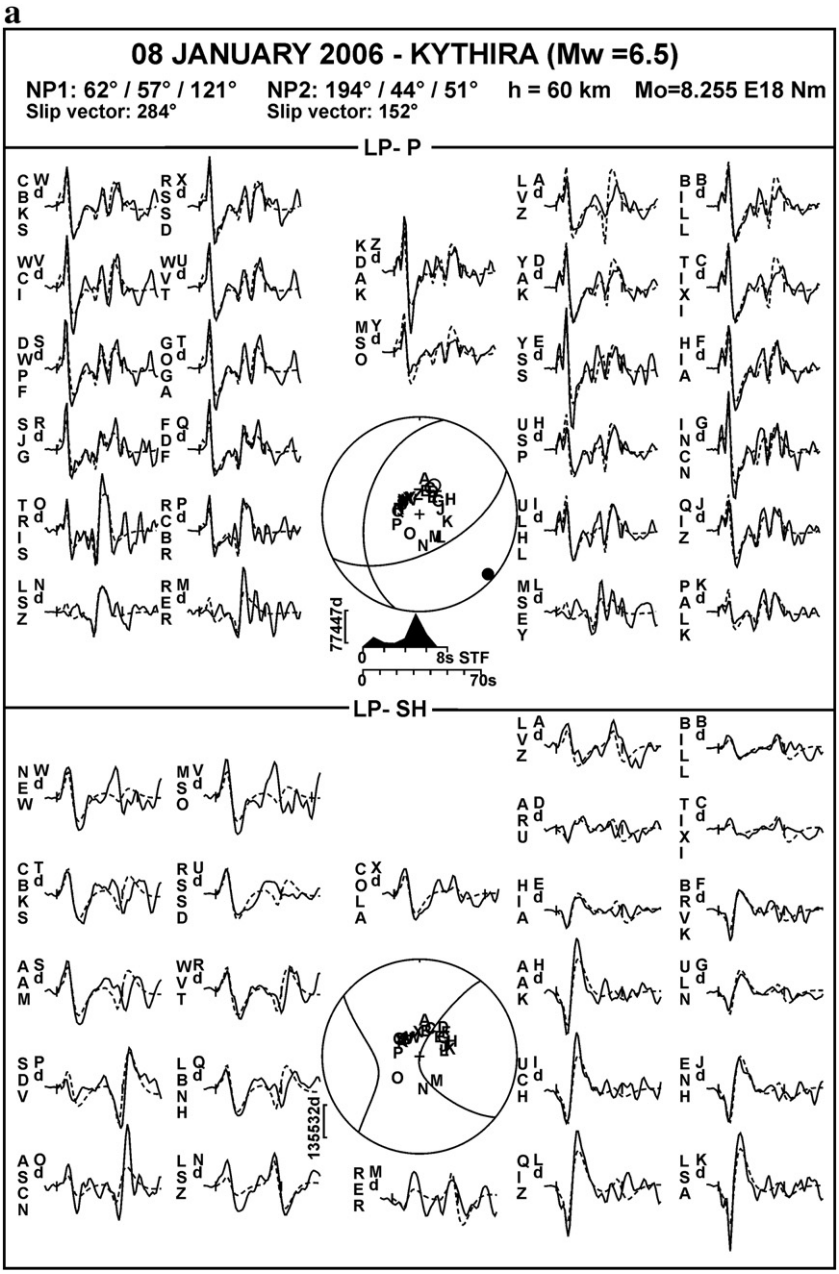

Fig. 8. a. Minimum misfit solution of the January 08, 2006 Kythira earthquake (M_w: 6.5) determined by teleseismic long period P- and SH-waveform inversion. Header information is as in Fig. 5a.b. Focal mechanism, co-seismic slip distribution and total moment rate function of the January 08, 2006 earthquake and comparison of the observed (black) and synthetic (red) broad band P-waveforms used in slip distribution inversion. Header information is as in Fig. 5d.

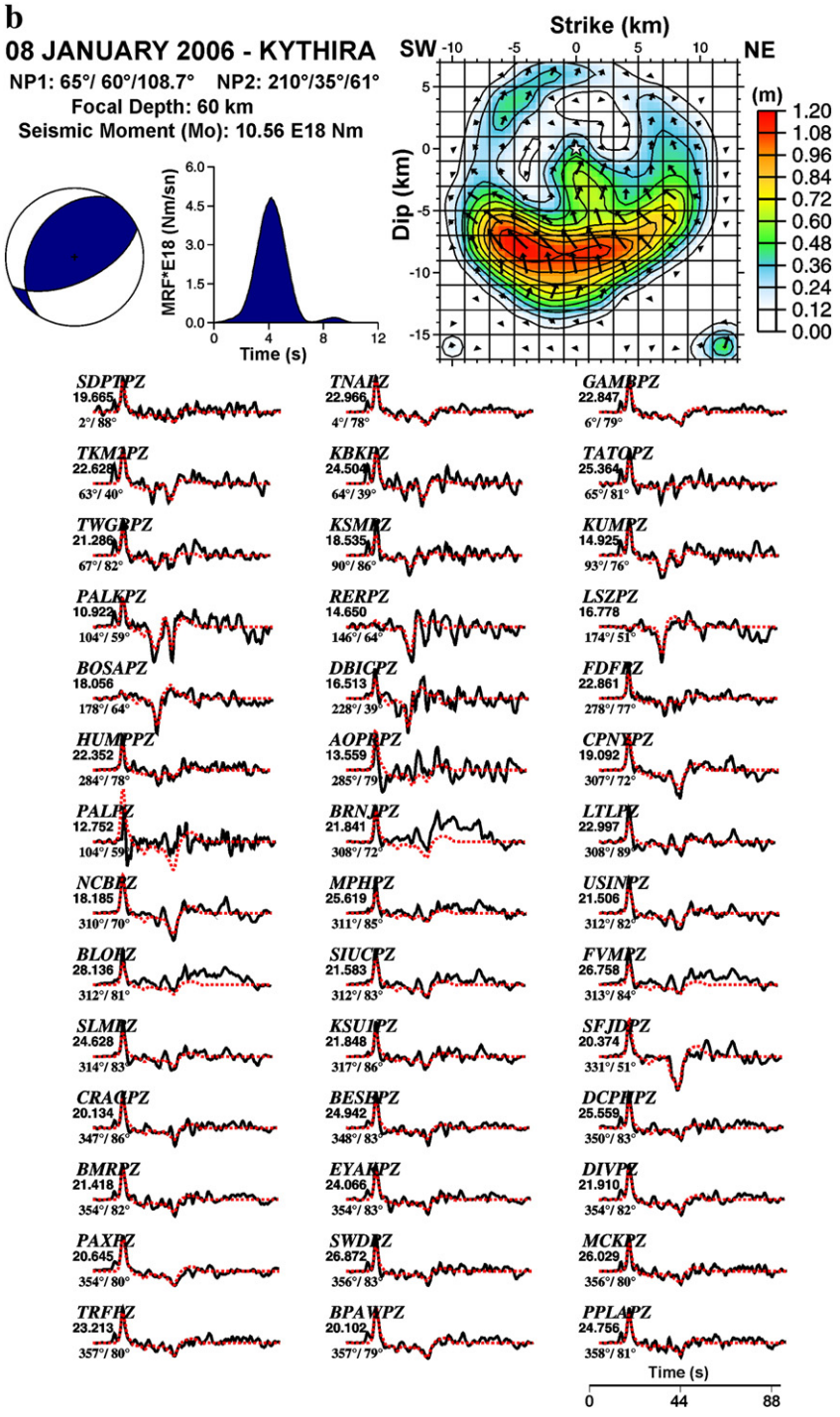

Fig. 8 (*continued*).

the focal sphere and a lower-case letter that identifies the type of instrument (d: long period, b: broad band). Focal spheres are shown with P- and SH-nodal planes in lower hemisphere projection. The vertical bar beneath the focal spheres indicates the scale in microns, with the lower-case letter identifying the instrument type as before. The source time function is shown in the middle of the figure, and beneath it is the time scale used for the waveforms. Station positions indicated by letters are arranged alphabetically clockwise, starting from north. * exhibits the waveforms not used in inversion.

For slip inversions, we adopted earthquake hypocenters reported by ISC (Table 1) earthquake catalogue and the faulting mechanism were taken from teleseismic P- and SH-waveform inversions obtained by this study. Rupture propagation velocity (V_r) was set to 3.2 km/s. Although the resolution of slip models are not too good due to the utilization of only teleseismic body wave and the lack of strong motion data, they give general view of rupture propagation on the fault plane and sizes of faulting area. However, Hartzell and Heaton (1983) pointed out that teleseismic waveforms constrain the timing or position of gross features on the fault, while the strong motion records resolve more of the details. We also calculated stress drop values ($\Delta\sigma = \frac{7 \times \pi^{3/2}}{16} \times \frac{Mo}{S^{3/2}}$; Aki, 1972; Kanamori, 1994; Kanamori and Anderson, 1975; Keilis-Borok, 1959) based on the assumption of circular crack model. At each slip model, star indicates

the location of initial break. The numbers below the station codes refer to maximum amplitude in microns. Source mechanism solutions of 19 earthquakes which are not given in the manuscript can be found in Supplementary Material Section.

3.1.1. Case studies

3.1.1.1. The July 20, 1996 earthquake (M_w: 6.1)—West of Rhodes Island. On July 20, 1996, a moderate-sized earthquake occurred in the western part of the Rhodes Island (No: 1 in Fig. 1b). In order to find earthquake source parameters, we used thirty two long period (LP) P- and eighteen SH-teleseismic body waveforms (Fig. 5a). Most of the seismograms were very well-modeled. Inversion result indicates normal faulting mechanism with small amount of strike slip component. The focal depth was found to be 9 ± 2 km. There are also another earthquakes (e.g., May 01, 2001—M_w: 5.1 and February 07, 2004—M_w: 5.2) which have the same faulting mechanisms and shallow focal depths in the same area. We suggested that these earthquakes might be related to graben systems (Mascle and Martin, 1990) developed on the overriding Aegean plate (Fig. 4a). T- Axes directions showed ~E–W extensional forces in the area. We compared the source parameters of the July 20, 1996 earthquake reported by several moment tensor catalogues (e.g., USGS-NEIC and HARVARD-CMT) and Louvari (2000). Source parameters given by Louvari (2000) were quite similar to our solution (Fig. 5b). But, small differences in dip and rake angles caused considerable misfits particularly on SH-waveforms. We also checked first motion polarities of P-waveforms recorded at regional and teleseismic stations (Fig. 5c) and applied uncertainty tests (see Appendix) to find the error limits of the minimum misfit solution. P-waveforms recorded by stations at regional distances especially have great importance since they help to constrain the nodal planes. For example, KIV ($\Delta = 14.09°$), ANTO ($\Delta = 5.87°$), GRFO ($\Delta = 17.78°$) and SSB ($\Delta = 19.31°$) stations locate close to nodal planes on the focal sphere and they clearly verified our faulting mechanism.

Further, the spatial and temporal slip distribution was obtained from the inversion of forty-two teleseismic broad band P-waveforms (Fig. 5d). The fault plane was divided into 7×5 sub-faults with

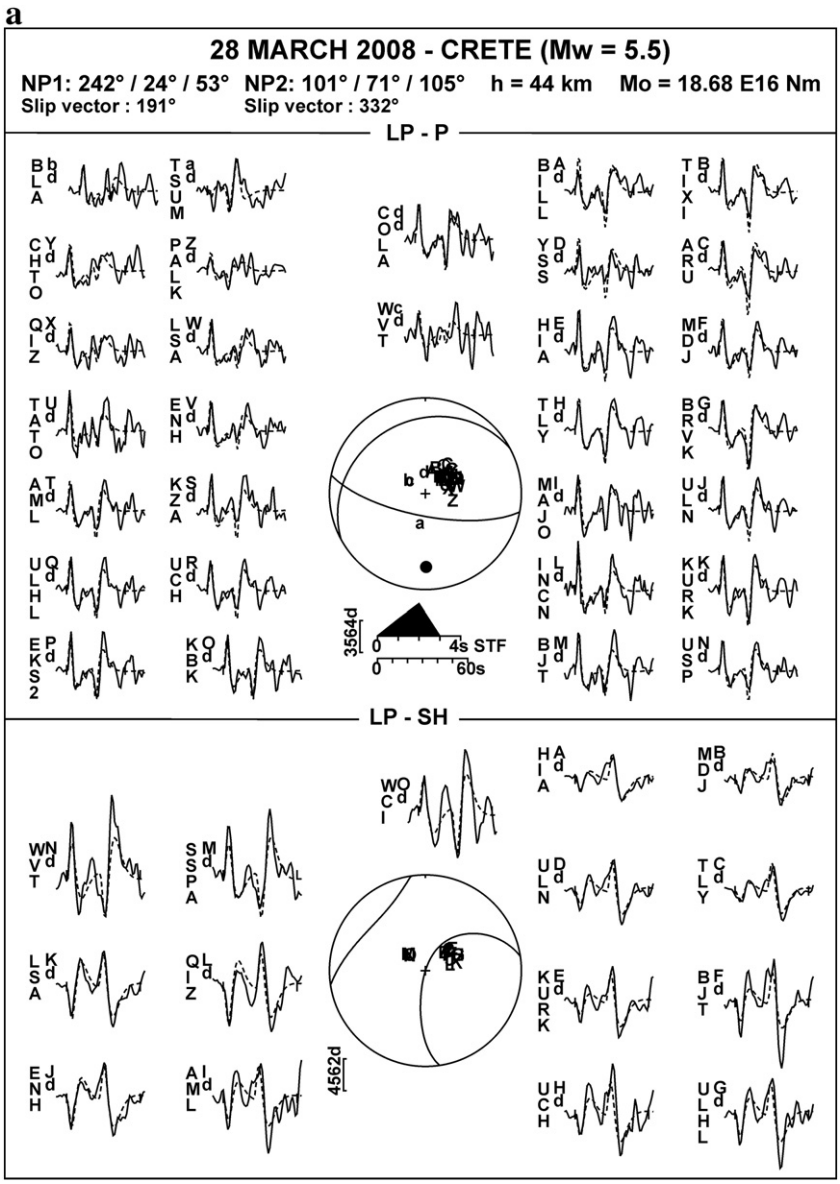

Fig. 9. a. Minimum misfit solution of the March 28, 2008 Crete earthquake (M_w: 5.5) determined by teleseismic long period P- and SH-waveform inversion. Header information is as in Fig. 5a.b. Focal mechanism, co-seismic slip distribution and total moment rate function of the March 28, 2008 earthquake and comparison of the observed (black) and synthetic (red) broad band P-waveforms used in slip distribution inversion. Header information is as in Fig. 5d.

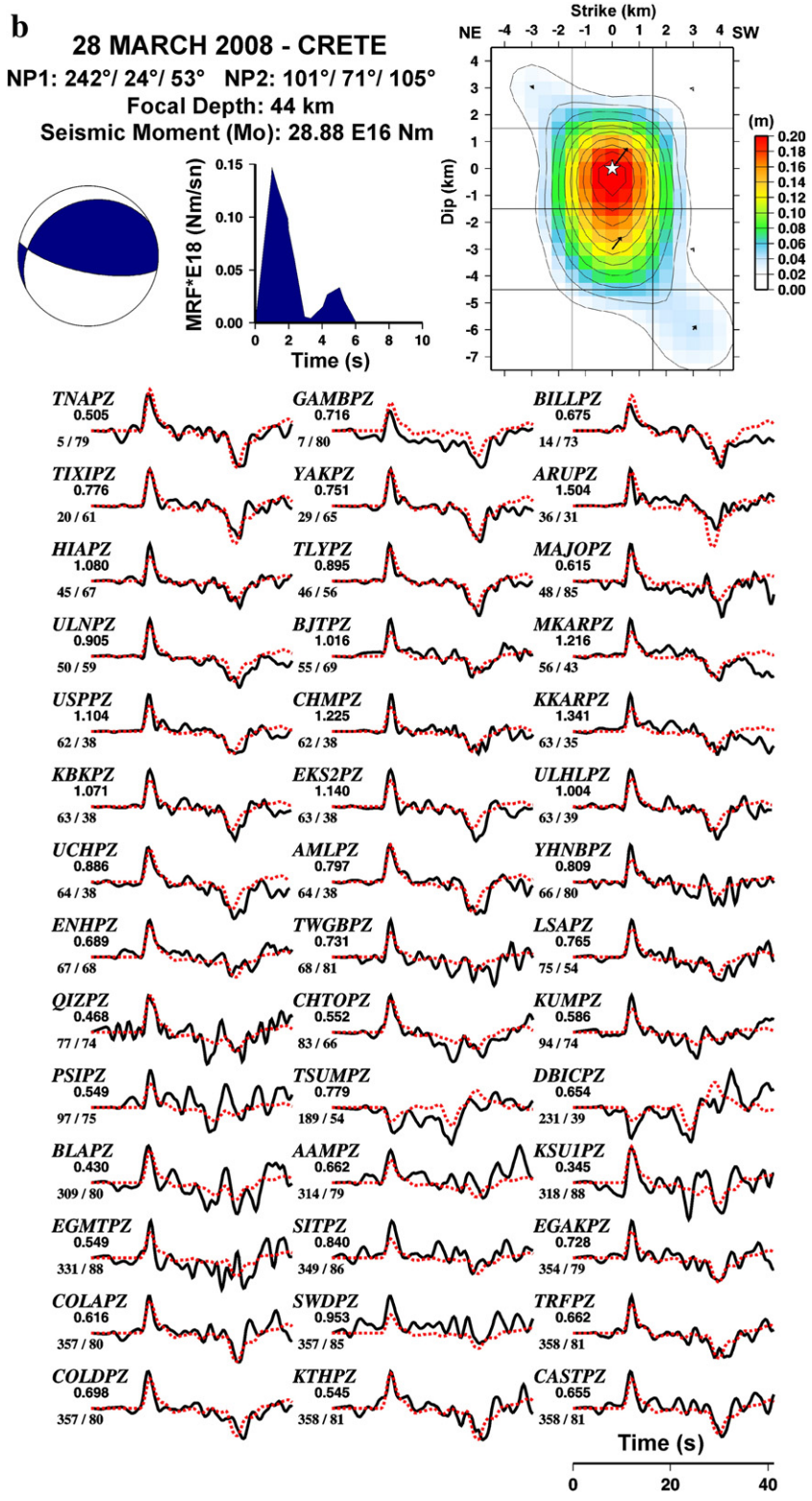

Fig. 9 (*continued*).

dimensions of 3×3 km^2. We determined simple and circular-shaped rupture at hypocenter. Maximum displacement was found to be ~1.3 m (Table 3). Slip model showed that rupture propagated along the dip direction of the fault. Rupture process occurred in two stages: [1] the rupture nucleated near the hypocenter, [2] then, it moved upwards about 10 km southwest from the epicenter. Source time functions (Fig. 5a,d) are relatively simple and reveal the earthquake duration of ~8 s. The fault length (L: 20 km), fault width (W: 14 km), average displacement (D_{av}: 23 cm) and stress drop ($\Delta\sigma$~10 bars) were also determined from the slip distribution model (Table 3).

3.1.1.2. The May 24, 2000 earthquake (M_w: 5.5)—Western part of the Hellenic Subduction Zone. Another moderate-sized earthquake (M_w: 5.5) occurred on May 24, 2000 at south of Greece (No: 2 in Fig. 1b). Twenty nine P- and twenty SH-waveforms were used in the inversion and normal faulting mechanism with considerable amount of strike

slip component was obtained (Fig. 6a). The focal depth was found to be 13 ± 2 km. Source time function has a simple shape and shows earthquake duration of ~4 s. On the contrary, Benetatos et al. (2004) indicated thrust faulting mechanism with strike slip component and a focal depth of 18 km for this earthquake. But, it is clearly seen that most of P-waveforms show dilatational first motion polarities at the center of the P-focal sphere, and they evidently support the normal faulting mechanism (Figs. 6a and A3).

Slip distribution model and comparison of observed and synthetic teleseismic waveforms are shown in Fig. 6b. Initially, we took a sufficiently broad faulting area (18 × 18 sub-faults) in order to see rupture propagation in a wide scale. Then, we selected the division which has 6 × 6 sub-faults with dimensions of 3 × 3 km^2. The moment–rate function was expanded by isosceles triangle functions, having 0.5 s rise time. We determined two major slip patches where high seismic moment releases were observed. Most of them largely occurred at the focal depth, and then slip moved downwards 6 km from the hypocenter. That is, rupture propagated mainly along the dip of the fault plane. Maximum and average displacement values (D_{max}: 20 cm; D_{av}: 8 cm), faulting area (S: 100 km^2), rupture duration (τ ~ 4 s) and stress drop (Δσ ~ 6 bars) were estimated parameters from the slip model (Fig. 6b and Table 3).

3.1.1.3. The January 22, 2002 earthquake (M_w: 6.1)—East of the Hellenic Subduction Zone. The earthquake epicenter located near the Karpathos Island in the eastern part of the Hellenic subduction zone (No: 3 in Fig. 1b). Minimum misfit solution shows strike slip faulting mechanism with a thrust component at a focal depth of 82 ± 2 km (Fig. 7a). Due to its faulting mechanism and focal depth, we suggested that this earthquake occurred in the downgoing African plate (Fig. 4c). Similar to the results of Benetatos et al. (2004), we obtained a T-axis direction showing down-dip extension same as the angle of Hellenic subduction zone (~35°) at this part of the region. We further constrained the minimum misfit solution by using the P-wave first motion polarities recorded at regional and teleseismic stations (Fig. A4).

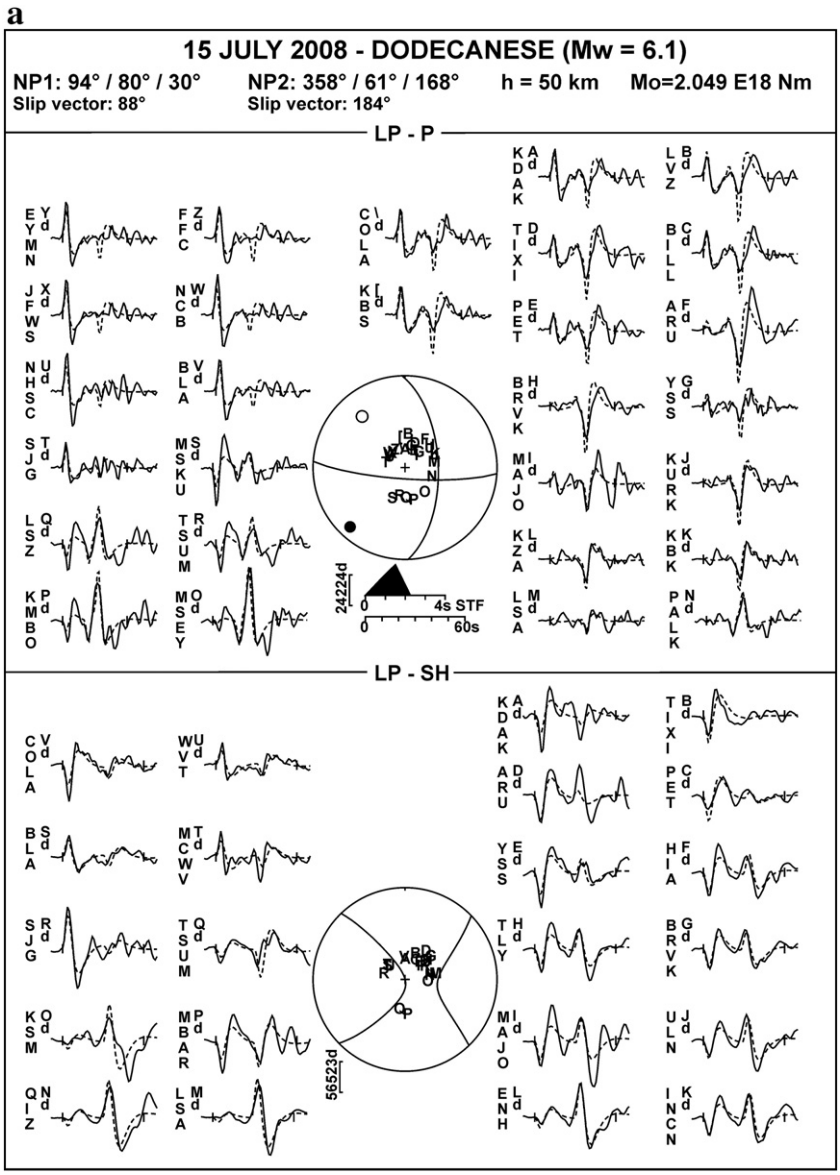

Fig. 10. a. Minimum misfit solution of the July 15, 2008 Dodecanese earthquake (M_w: 6.1) determined by teleseismic long period P- and SH-waveform inversion. Header information is as in Fig. 5a.b. Focal mechanism, co-seismic slip distribution and total moment rate function of the July 15, 2008 earthquake and comparison of the observed (black) and synthetic (red) broad band P-waveforms used in slip distribution inversion. Header information is as in Fig. 5d.

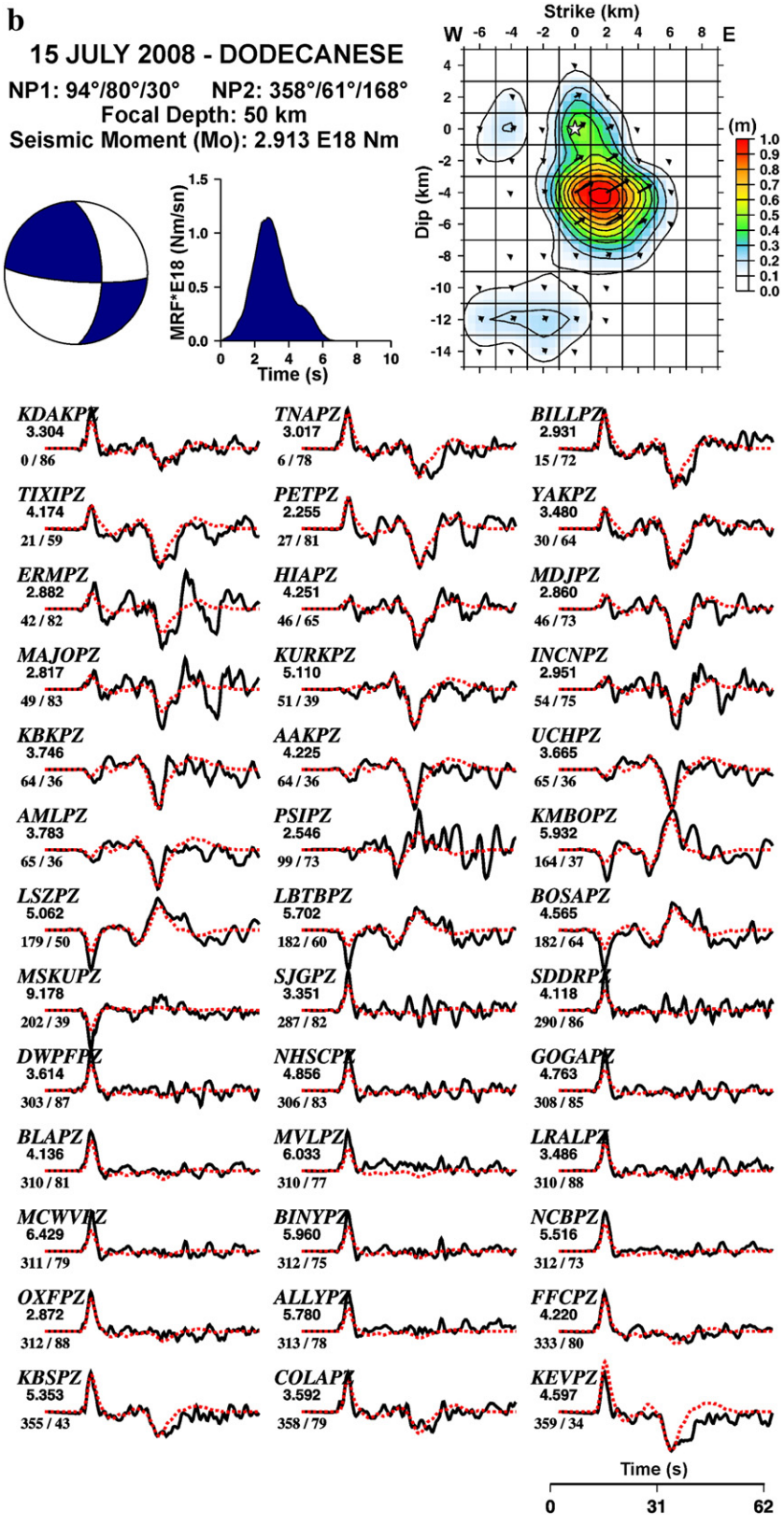

Fig. 10 (*continued*).

Observed and synthetic teleseismic broad band P-waveforms used in slip inversion are shown in Fig. 7b. We chose the nodal plane which has strike (ϕ: 4°), dip (δ: 41°) and rake (λ: 175°) angles as a fault plane in the inversion. This plane was divided into 8×8 sub-faults which have dimensions of 3×3 km^2. The moment–rate function was expanded by isosceles triangle functions, having 1 s rise time. Obtained source parameters were seismic moment (M_o: 2.1×10^{18}Nm), source duration (~8 s), fault length (L: 10 km), fault width (W: 15 km) and stress drop ($\triangle\sigma$~29 bars) (Table 3). We further determined that maximum displacement (D_{max}: 50 cm) occurred beneath ~6 km of the hypocenter.

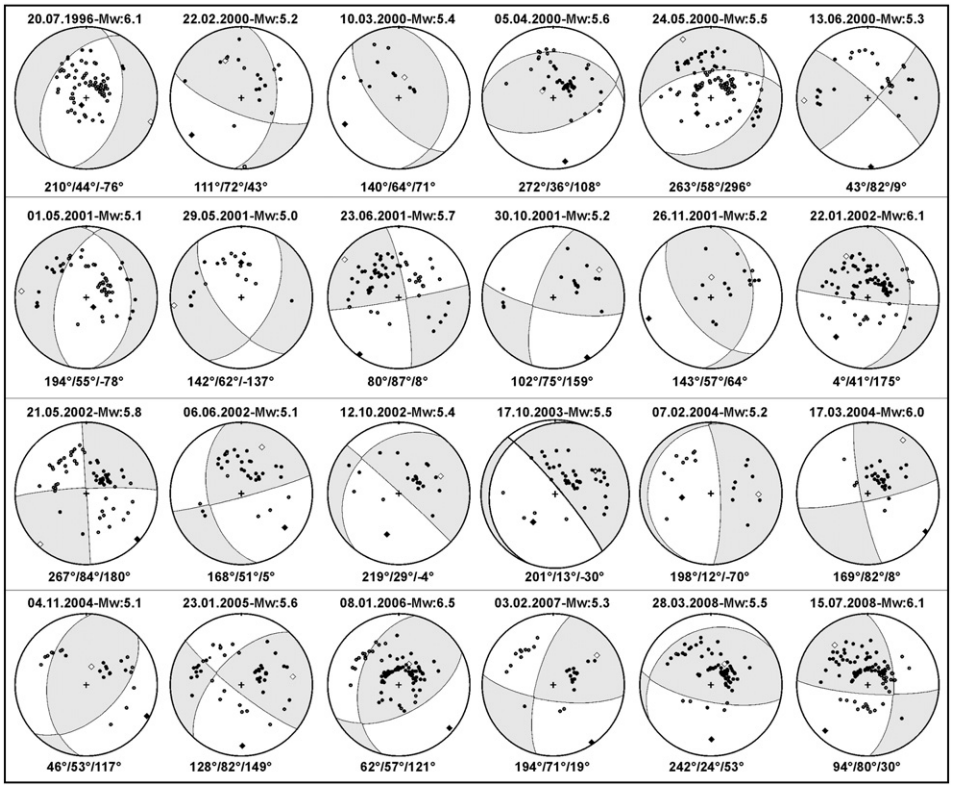

Fig. 11. Lower hemisphere equal area projections of the first motion polarity data recorded by stations at regional and teleseismic distances for all earthquakes studied in this article. Station positions of the focal sphere have been plotted using the same velocity model beneath the source used in our minimum misfit solution. Filled circles are compressional first motions, opens are dilatational. Nodal planes are those of the minimum misfit solutions. Above each focal sphere is the event's date (day, month, year) and moment magnitude (M_w). Strike, dip and rake angles of first nodal plane is also shown under focal spheres.

3.1.1.4. The January 08, 2006 earthquake (M_w: 6.5)—Kythira Island. On January 08, 2006, an intermediate-depth earthquake (No: 4 in Fig. 1b) occurred at the western part of the Hellenic subduction zone close to the island of Kythira (southern Greece). It was strongly felt in nearby regions and slight damage was especially observed in the village Mitata of Kythira Island (Karakostas et al., 2006; Konstantinou et al., 2006; Skarlatoudis et al., 2009; Taymaz et al., 2007c). The main earthquake and its aftershocks are directly related to the active Hellenic subduction zone. Many studies have been done in order to define source characteristics of this earthquake. For

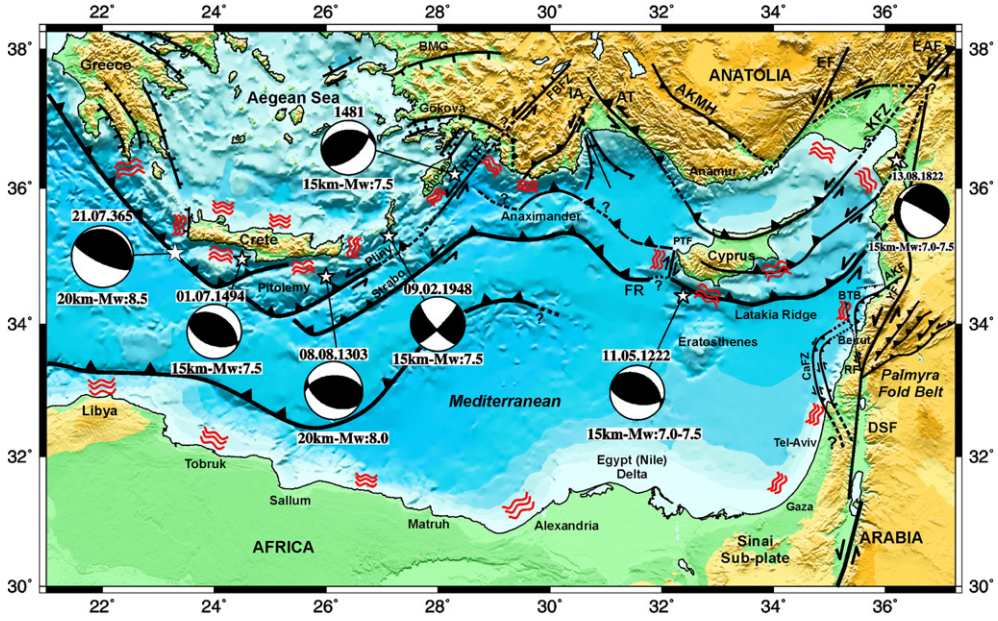

Fig. 12. A schematic sketch map of potential tsunamigenic regions and representative focal mechanism solutions of historical tsunamigenic Eastern Mediterranean earthquakes estimated from current source mechanisms, and by analogy of plate boundaries and tectonic motions. Coastal plains that are at tsunamigenic earthquake risk are marked with red wave-curves. AKF: Akkar Fault, AKMH: Aksu, Köprü, Manavgat Basins, AT: Aksu Thrust, BMG: Büyük Menderes Graben, BTB: Beirut–Tripoli Thrust, CaFZ: Carmel Fault Zone, DSF: Dead Sea Fault, EAF: East Anatolian Fault, EF: Ecemiş Fault, FR: Florence Rise, FBFZ: Fethiye-Burdur Fault Zone, IA: Isparta Angle, KFZ: Karataş Fault Zone, PTF: Paphos Transform Fault, RF: Roum Fault, RTF: Rhodes Transform Fault, YF: Yammouneh Fault (see references in Fig. 1b).

example, Ventouzi et al. (2007) pointed out a NE–SW trending of the aftershock sequence, in good agreement with the general stress field of the intermediate-depth earthquakes of the western Hellenic subduction zone. In addition, Skarlatoudis et al. (2009) obtained differences in attenuation patterns between the back-arc and along-arc records by using Acceleration-Sensor and Broad-band Velocity-Sensor records. We observed that a simple double-couple mechanism was adequate to model the details of body waveforms where clear depth phases of P- and SH- were quite helpful to distinguish the nodal planes. Minimum misfit solution from the teleseismic body waves was determined to be a reverse faulting mechanism with considerable amount of strike slip motion (for NP1 strike = 62°, dip = 57°, rake = 121°; for NP2 strike = 194°, dip = 44°, rake = 51°; $M_o = 8.255 \times 10^{18}$ N m). The source time function is rather simple and about 6–8 s (Fig. 8a). At this part of the region northwest – southeast compression follows the local trend of the Hellenic arc and northeast–southwest down-dip extension is parallel to the dip of the subducting slab (Kiratzi and Papazachos, 1995).

Rupture properties and slip histories on the fault plane were further obtained by carefully analyzing the details of broad band records (Fig. 8b). We selected the nodal plane which has a right-lateral strike slip component as a fault plane. The inversion of teleseismic waveforms showed that the seismic moment was released in two main slip patches on the fault propagating upwards with a rupture velocity of Vr = 3.2 km/s. We calculated rupture area and maximum displacement at the centroid to be A = 576 km^2 and D_{max} = 120 cm, respectively (see Table 3). The overall mechanism is in agreement with known regional stress field where compression is confirmed to be NW–SE along with the trend of the Hellenic trench at intermediate depths. The further details of this event were studied by analyzing near-field waveforms collected during EGELADOS experiment and supplemented with the observed near-field strong motion records (Skarlatoudis et al., 2009). Furthermore, Taymaz et al. (2007c) reported the uncorrected maximum accelerations of the nearest stations to be 0.13 g on the island of Kythira and 0.14 g on Agios Nikolaos, and 0.05 g on Crete Island.

3.1.1.5. The March 28, 2008 earthquake (M_w: 5.5)—South of Crete. This earthquake occurred at the south of Crete (No: 5 in Fig. 1b). We used thirty P- and fifteen SH-teleseismic waveforms to find a minimum misfit solution. Inversion result indicates thrust faulting mechanism with a small amount of strike slip component. We proposed that this earthquake occurred related to the African–Aegean convergence (Figs. 4b and 9a). The focal depth of 44 ± 2 km and seismic moment of 18.68×10^{16} N m was found (Table 1). Similarly, Shaw and Jackson (2010) reported 43 ± 4 km focal depth and they emphasized that this earthquake occurred on the subduction zone interface. Moment tensor catalogues such as Harvard-CMT, USGS-NEIC, MEDNET-INGV, ETHZ-SED reported earthquake source parameters indicating thrust faulting mechanism with strike slip component which is similar to our minimum misfit solution, but their reported focal depths are different. We checked P-wave first motion polarity distributions (Fig. A6) and observed ~±5°–10° errors in strike, dip and rake angles.

In slip distribution inversion, we used forty-two teleseismic broad band P-waveforms. We chose the low-angle and north-dipping nodal plane as a fault plane. Source orientation (strike, dip, rake = 242°, 24°, 53°) and earthquake epicenter reported by ISC (latitude = 34.79°N; longitude = 25.34°E) were adopted as initial inversion parameters. We divided the fault plane into 3 × 4 sub-faults, each of them has an area of 3 × 3 km^2. The slip rate function on each sub-fault was expanded into a series of three triangle functions with a rise time of 1 s. Slip model shows a uniform and circular-shaped rupture propagation on the fault plane (Fig. 9b). Maximum moment release occurred within ~3 s. It is consistent with teleseismic waveform modeling result (Fig. 9a,b). The maximum slip was obtained to be ~20 cm at the centroid and ~16 cm average over the faulting area (Table 3).

Table 4
Assumed source parameters of tsunamigenic Eastern Mediterranean earthquakes used in plausible tsunami scenarios. I_o: Intensity, t_o: origin time, M: Magnitude, L: Fault length, W: fault width, H: focal depth, D: displacement, and NP: Nodal Plane. P07: Papadopoulos et al. (2007); PF05: Papadopoulos and Fokaefs (2005); GC05a: Guidoboni and Comastri (2005a); S05: Sbeinati et al. (2005); A94: Ambraseys et al. (1994), Y08: Yolsal (2008).

Date	Mag.	Region	Reference
21 July 365	M > 8.0	Crete (35°N, 23°E)	
		NP1: 295°/15°/90°	P07, PF05
		NP2: 115°/75°/90°	A94, Y08
		L: 200 km, W:50 km; H: 20 km; D: 15 m	
08 August 1303		Crete	
		Lat: 35° 11′, Lon: 25° 38′	
	M_s: 8.0	NP1: 115°/45°/110°	GC05a
	I_o = X	NP2: 268°/48°/71°	P07, PF05, Y08
		L: 100 km, W:30 km; H: 20 km; D: 8 m	
3 May 1481	M ~ 7.5	Southern Aegea, Rhodes, Antalya	GC05a, Y08
17–18–19 December 1481		NP1: 50°/60°/70°	
28 February–03 April—23 May 1851		NP2: 266°/36°/121°	
		L: 70 km, W:30 km; H: 15 km; D: 3.5 m	
1 July 1494	I_o = VIII–IX	Crete	GC05a, Y08
		Lat: 35° 12′; Lon: 24° 55′	
		NP1: 110°/50°/80°	
		NP2:305°/41°/102°	
		L: 70 km, W:30 km; H: 15 km; D: 3.5 m	
09 February 1948	M_s: 7.1	Karpathos island, SE Aegea	P07, PF05, Y08
	I_o: IX	t_o: 12:58:13–Lat: 35° 30′; Lon: 27° 12′	
		NP1: 45°/80°/−15°	
		NP2: 138°/75°/−170°	
		L: 95 km, W:20 km; H: 15 km; D: 5 m	
11 May 1222	M_e = 6.0	Cyprus, lat: 34° 42′; lon: 32° 48′	GC05, Y08
	I_o = IX	NP1: 305°/35°/110°	
		NP2: 101°/57°/77°	
		L: 50 km, W:25 km; H: 15 km; D: 3 m	
13 August 1822	M_L 7.1; M_s 7.4	Syria, Iskenderun, Jerusalem, Beirut	S05, Y08
		NP1: 190°/20°/−20°	
		NP2: 299°/83°/−109°	
		L: 50 km, W:50 km; H: 15 km; D: 5 m	

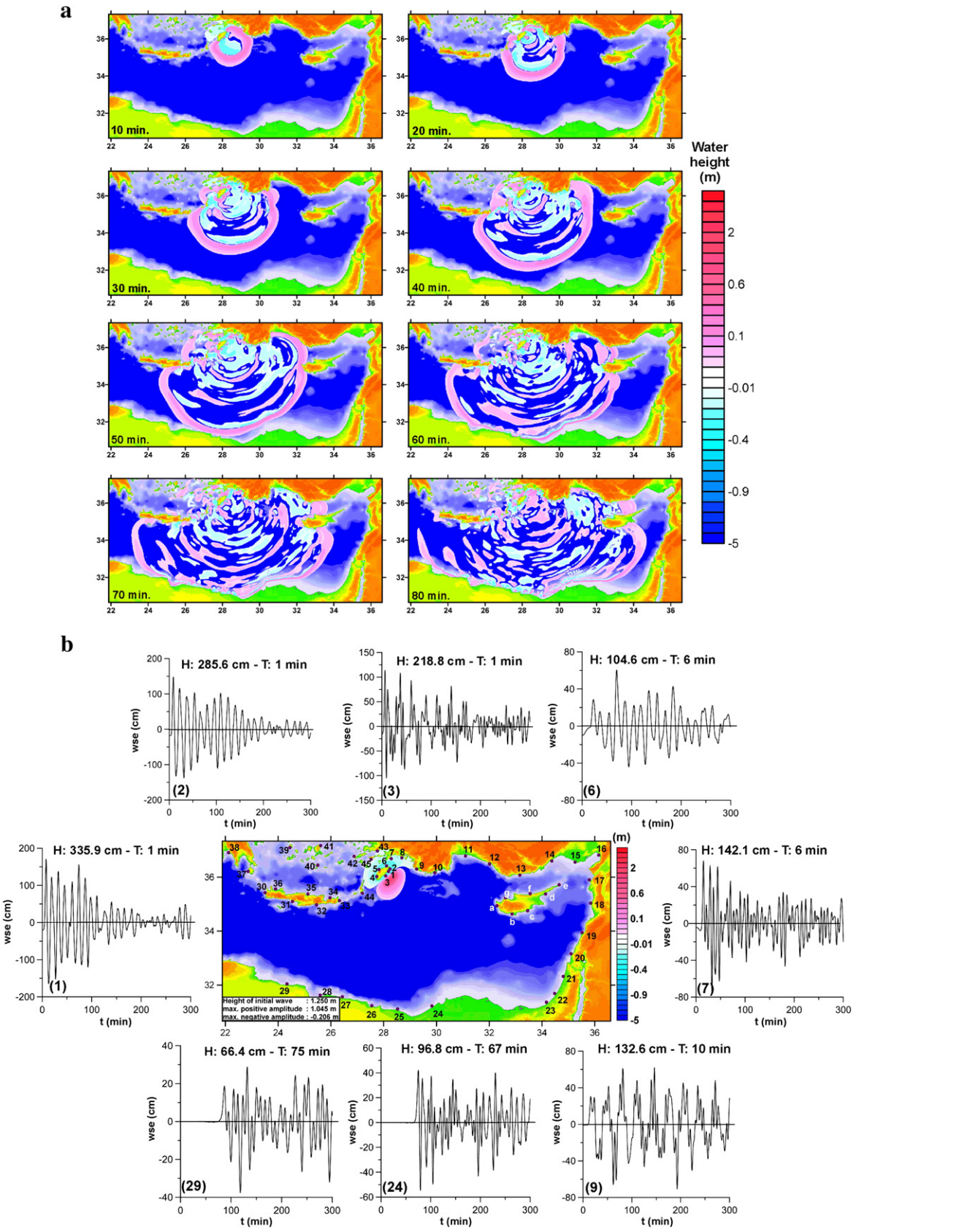

Fig. 13. a: Snapshots of sea states at different time steps (t = 10, 30, 50, 70 min) generated by non-linear shallow water theory for various times at 10 min intervals for 1481 Rhodes earthquakes. The color scale which is given on the right-hand side in meters shows the water height values.b. Computed tsunami records at selected locations for historical 1481 Rhodes earthquakes. The vertical and horizontal scales show water surface elevation (wse) in centimeters and tsunami simulation time (t) in minutes, respectively. Above each synthetic mareogram, the maximum synthetic wave heights (H) and theoretical arrival times (T) of the initial wave are given in centimeters and minutes, respectively. Letters and numbers indicate synthetic tsunami mareograms generated at pseudo-tide-gauge locations. The height of initial tsunami wave is given in the box in the lower left corner of the map.c. Distribution of maximum positive tsunami wave amplitudes along the north and south coasts of the Eastern Mediterranean and directivity of tsunami wave propagation during 1481 Rhodes earthquakes sequences.

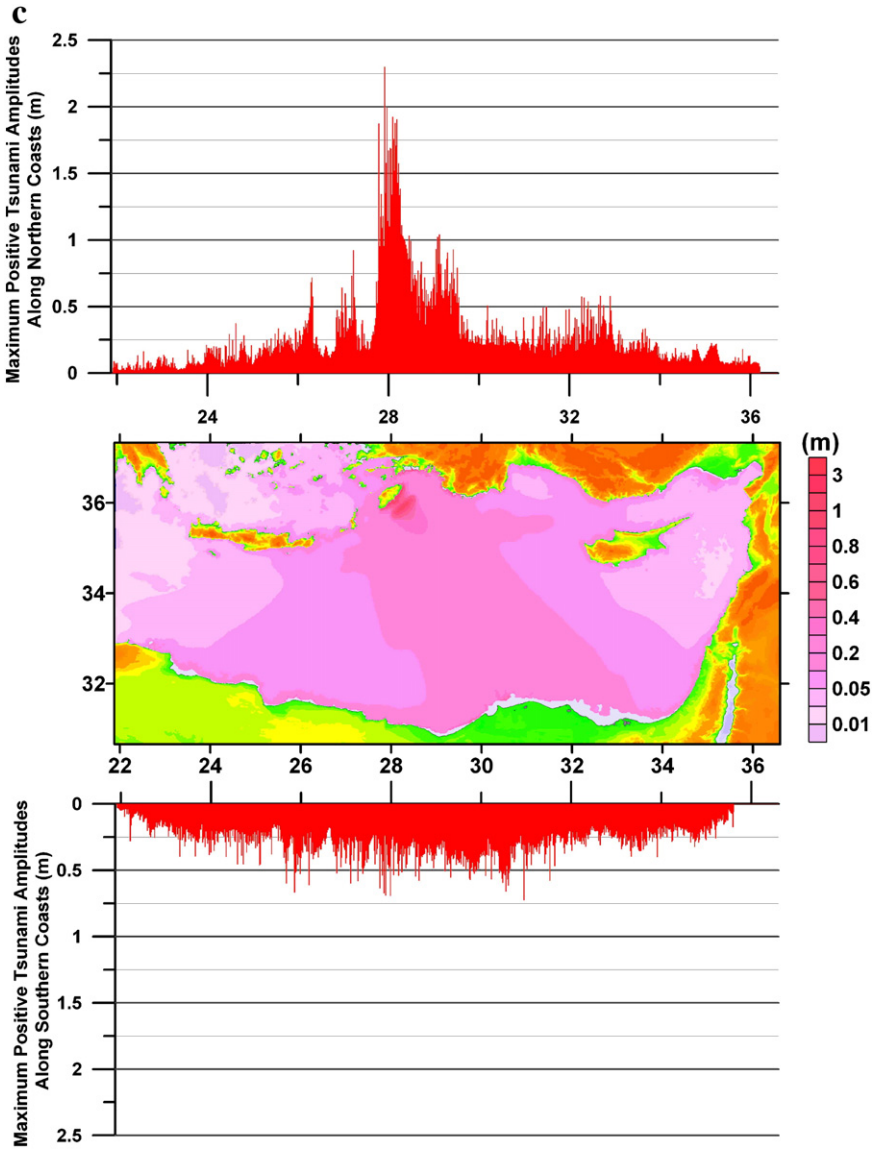

Fig. 13 (*continued*).

3.1.1.6. The July 15, 2008 earthquake (M_w: 6.1)—South East of Rhodes Island. This earthquake occurred at the southeastern part of the Rhodes Island (No: 6 in Fig. 1b). We used teleseismic long period twenty eight P- and twenty two SH-waveforms to determine the minimum misfit solution. Result indicates left-lateral strike slip faulting mechanism with thrust component (Fig. 4c). We found the seismic moment (M_o) and focal depth (h) to be 2.049×10^{18} N m and 50 km, respectively (Table 1). The depth phases were clearly seen on both P- and SH-waveforms. Further, we obtained source time function representing the main moment release in about 3 s (Fig. 10a). By using seismic moment value and Kanamori (1977) equation, we calculated earthquake moment magnitude (M_w) to be 6.1. Both uncertainty tests and P-wave first motion polarities (Fig. A7) revealed about $\pm5°$–10° errors in strike, dip and rake angles. Moment tensor catalogues reported similar source mechanism solutions, but their focal depths and seismic moment values were slightly different from each other. For example, Harvard-CMT and INGV-RCMT catalogues reported the focal depth as 42.2 km and 37 km, respectively.

We used thirty nine teleseismic broad band P-waveforms in slip distribution inversion (Fig. 10b). Resolution of the model has been further investigated by several synthetic tests performed using varied grid sizes. Finally, the fault plane was divided into 8×10 sub-faults, each having an area of 2×2 km^2. We chose a nodal plane which has strike, dip and rake angles as 94°, 80° and 30°, respectively as a fault plane (Fig. 10b and Table 1). Our slip model showed that rupture started at 4 km below the hypocenter, and propagated mainly along the dip direction of the fault towards the east. The effective rupture area was roughly estimated to be 12 km (length) $\times$ 16 km (width). The maximum displacement and seismic moment were found to be 1 m and 291.3×10^{16} N m, respectively. We also calculated the stress drop ($\Delta\sigma$~27 bars) and average displacement (D_{av}: 50.5 cm) from our slip inversion model (Table 3).

For all earthquakes studied in this article, P-wave first motion polarities recorded by regional and teleseismic stations are plotted in Fig. 11. As noticeably seen, our minimum misfit solutions are mostly in accordance with distributions of P-wave first motion polarities.

3.2. Simulation of selected historical tsunamis

Historical catalogues, documents, geological, coastal and archaeological evidences indicate many catastrophic earthquakes and associated tsunamis which demolished the Eastern Mediterranean coastal plains, especially Crete, Rhodes, Cyprus Dodecanese islands and Levantine Basin in the past (e.g., Ambraseys, 1962; Antonopoulos,

1980; Guidoboni and Comastri, 2005a, 2005b; Pirazzoli et al., 1982; Sbeinati et al., 2005; Soloviev et al., 2000; Stiros, 2001, 2010; Stiros and Drakos, 2006). Our approach combines updated knowledge on the regional tectonic setting and scenario-like calculations of expected tsunami impact. We have simulated tsunami wave propagations of historical 365 AD, 1303 and 1494 Crete and 1481 and 1948 Dodecanese Islands earthquakes which occurred along the Hellenic subduction zone in the Eastern Mediterranean region (Fig. 12 and Table 4). We emphasized the importance of joint examination of earthquake source parameters and tsunami simulation studies. Further, simulation results of historical 1222 Cyprus and 1822 Syria tsunamis were obtained, and given in Appendix (Figs. A8–A9). It is well-known that the choice of tsunami source is too important and usually requires a good knowledge of active tectonics and earthquake rupture mechanisms since it affects the overall characteristics of synthetic tsunami waves. In order to constrain earthquake source parameters (Table 4), we specifically used current plate boundaries, empirical seismological equations (Mai and Beroza, 2000; Tan and Taymaz, 2006; Wells and Coppersmith, 1994), focal mechanism solutions of Crete – Hellenic subduction zone earthquakes (e.g., Benetatos et al., 2004; Bohnhoff et al., 2005; Hatzfeld et al., 1993; Kiratzi and Louvari, 2003; Laigle et al., 2004; Louvari, 2000; Papazachos et al., 1999; Shaw and Jackson, 2010; Taymaz et al., 1990, 1991, 2004, 2007a, 2007b; Yolsal, 2008; Yolsal et al., 2007), moment tensor catalogues (e.g., Harvard-CMT, UGSG, MED-RCMT) and historical earthquake catalogues with verified documents (Ambraseys, 1962; Ambraseys et al., 1994; Antonopoulos, 1980; Fokaefs and Papadopoulos, 2006; Guidoboni and Comastri, 2005a, 2005b; Sbeinati et al., 2005). We briefly summarized the results of numerical wave simulations concerned with these major historical tsunamigenic earthquakes occurred in Eastern Mediterranean.

3.2.1. Dodecanese Islands Region

3.2.1.1. The May–December, 1481 earthquakes (M ~ 7.0–7.5)—Rhodes. Many tsunamigenic earthquakes have been reported in Dodecanese

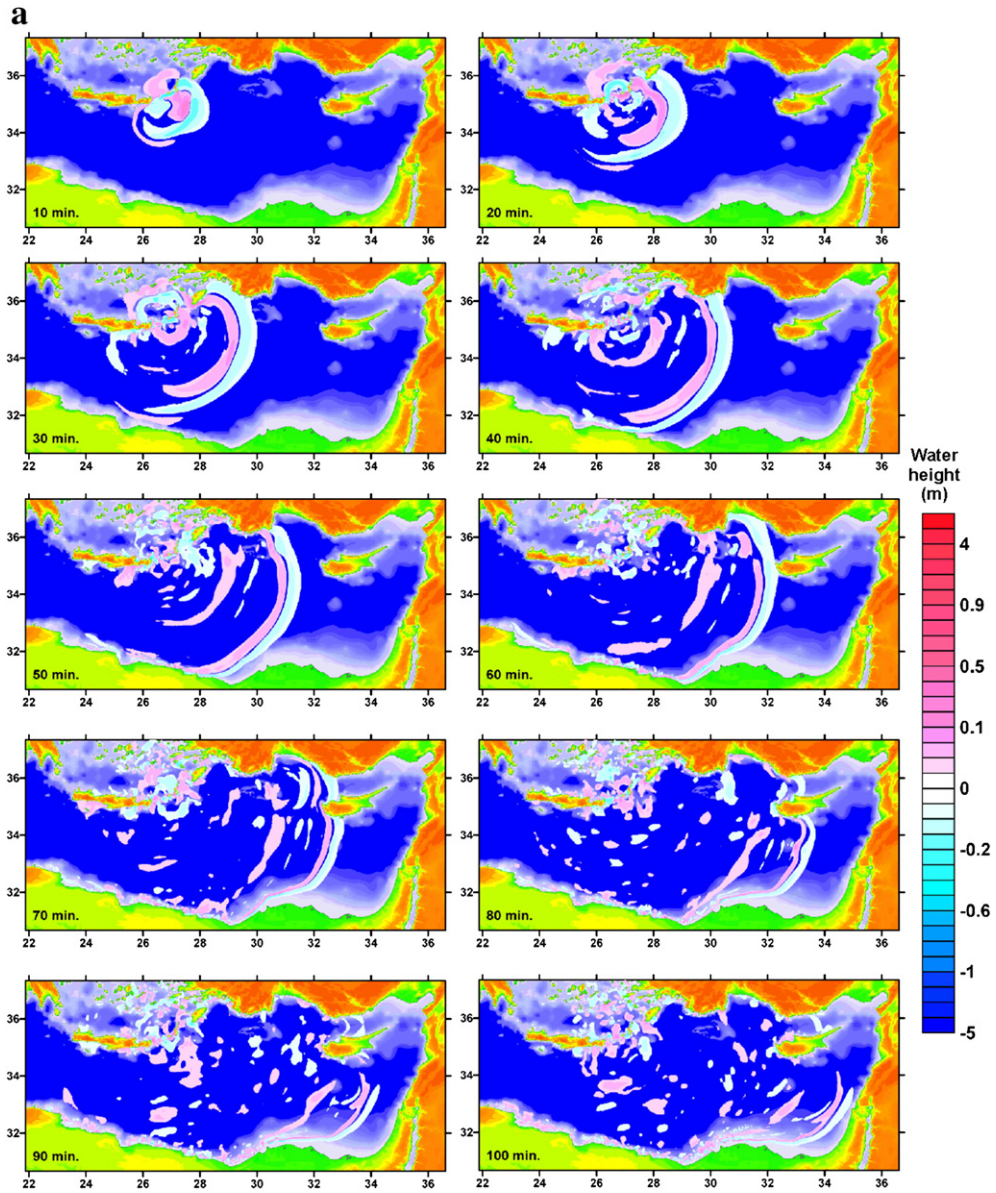

Fig. 14. a. Snapshots of sea states at different time steps (t = 10, 30, 50, 70, 90 min) generated by non-linear shallow water theory for various times at 10 min intervals for the February 09, 1948 Karpathos earthquake. The color scale which is given on the right-hand side in meters shows the water height values.b. Computed tsunami records at selected locations for the February 09, 1948 Karpathos earthquake. Header information is as in Fig. 13b.c. Distribution of maximum positive tsunami wave amplitudes along the north and south coasts of the Eastern Mediterranean and directivity of tsunami wave propagation during the February 09, 1948 Karpathos earthquake.

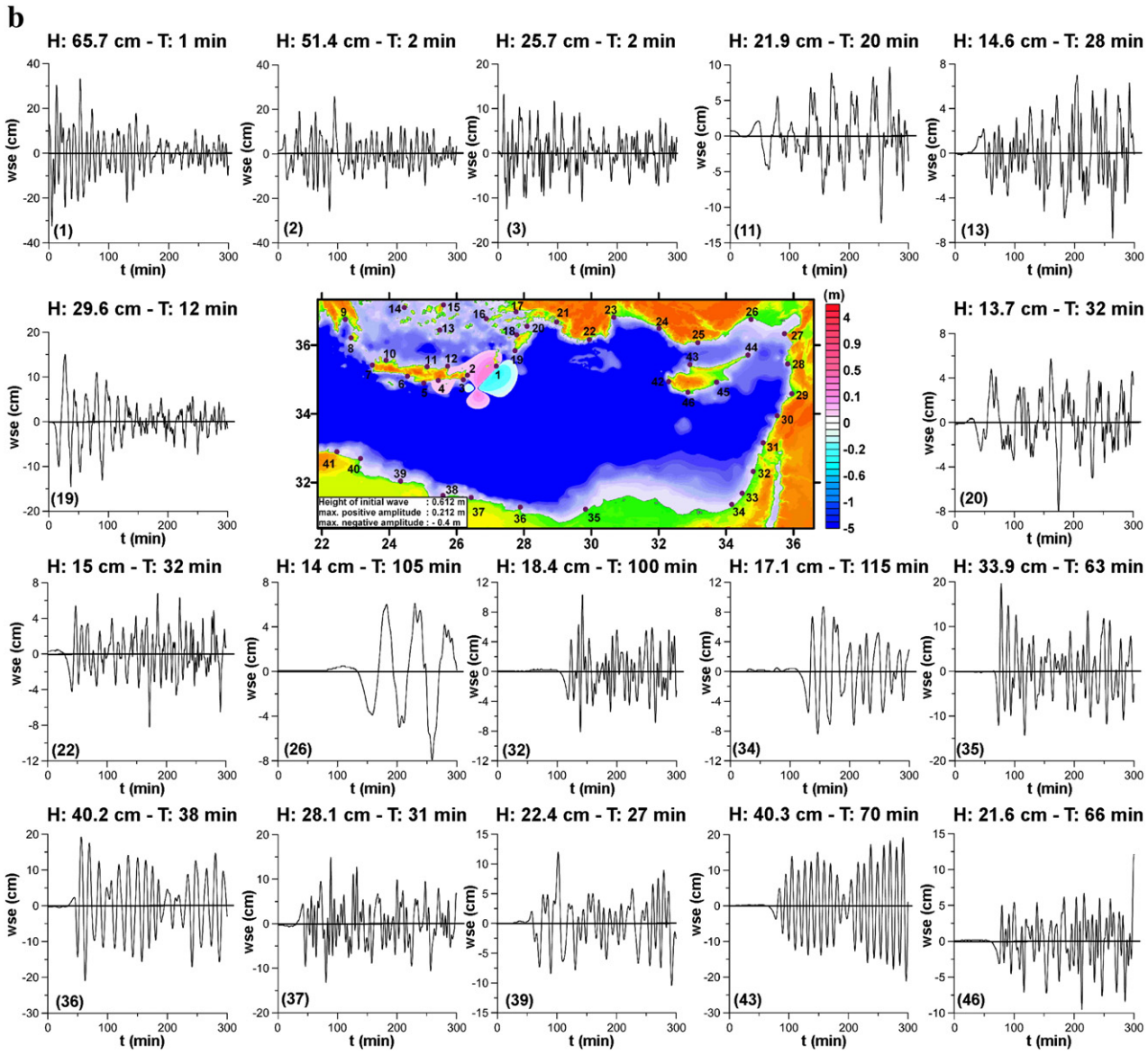

Fig. 14 (*continued*).

islands region (Fig. 12 and Table 4). The May–December, 1481 earthquake series are one of the best reported and well-known historical earthquakes. Coronelli and Parisotti (1688) reported that these earthquake series caused ~3 m high tsunami waves which flooded the coastal plains of Rhodes Island, and a ship was smashed in a reef and sank with all its crew. Ben Menahem (1979) expressed tsunami waves as far away as the Levantine coasts. In addition, Papadopoulos et al. (2004) found a sedimentary layer in Dalaman which shows 1473 ± 46 AD earthquake and related tsunami by using radiocarbon dating methods. We proposed a hypothetical tsunami scenario for this tsunamigenic earthquake by constraining the earthquake source parameters. These parameters and a representative fault plane solution are given in Table 4 and Fig. 12.

Snapshots of tsunami wave propagations for various times at 10 min intervals and computed water surface fluctuations within the limitations of the bathymetric grid size are plotted in Fig. 13a. Effects of tsunami waves are clearly seen when synthetic tsunami simulations at several sea states are compared. Simulation results (Fig. 13a,b) show that tsunami waves may reach SW Turkish coasts (e.g. Muğla and Antalya) in ~10–20 min, Libyan coastal plains in ~60 min, Cyprus in ~50 min and Alexandria–Nile Delta in ~70 min. The largest wave amplitudes are calculated near the earthquake epicenter (~3.5 m at location 1) and along Turkish coastal plains (~1.5 m at locations 7 and 9). However, tsunami waves had not large amplitudes so as to demolish the Cyprus and Levantine coasts (~20–30 cm) during the 1481 tsunami (Fig. 13b). Fig. 13c shows the distributions of computed maximum positive tsunami amplitudes and directions of tsunami wave propagation along the northern and southern coastal plains in Eastern Mediterranean. It is obviously seen that wave propagation is grown at the right angles to the major axis of tsunami source, that is, it propagated towards southeast direction. Consequently, anomalous sea wave amplitudes at Alexandria and African coastal plains (~1 m at location 24) were calculated (Fig. 13b,c).

3.2.1.2. The February 9, 1948 earthquake (M~7.0–7.5)—Karpathos Island. As reported by Galanopoulos (1960), the February 9, 1948 earthquake caused destruction near Pigadia, the main town of the Karpathos Island, *and* " … a huge seismic sea wave that penetrated inland 1 km" (Fig. 12). The first motion of tsunami wave was withdrawal (Papadopoulos et al., 2007). A few eye witnesses reported that first tsunami wave arrived to Karpathos Island coasts about 5 to 10 min after the earthquake and many vessels were violently

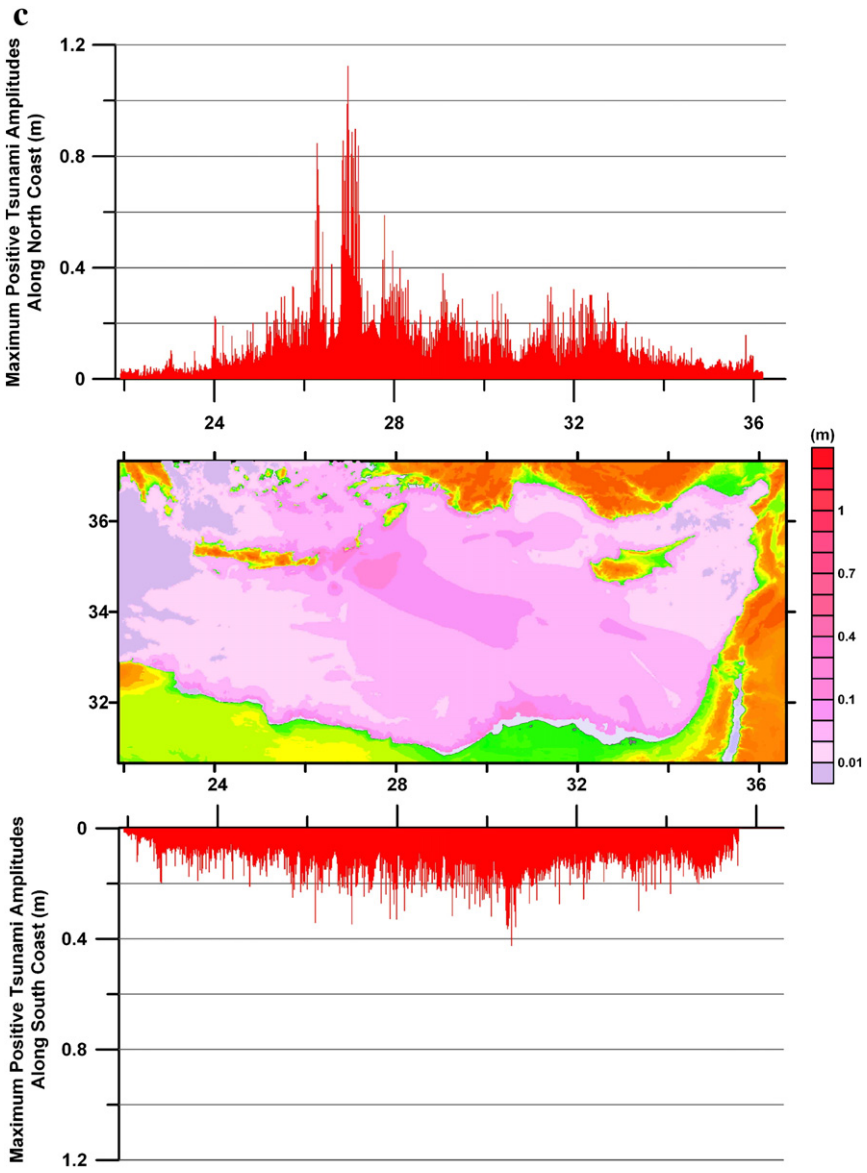

Fig. 14 (*continued*).

moved ashore and destructed. Field surveys revealed ~2.5 m tsunami wave heights in Pigadia and 250 m inland penetration at maximum to the west of this town (Papadopoulos and Fokaefs, 2005; Papadopoulos et al., 2007). Therefore, it is suggested that the earthquake epicenter was probably near the Karpathos Island, its magnitude was 7.1 and it had a shallow focal depth (Altınok and Ersoy, 2000; Papadopoulos, 2001). In the light of earthquake source mechanisms, current plate motions and tectonic boundaries near the Dodecanese Islands region, we constrained strike, dip and rake angles as 45°, 80° and −15°, respectively (Fig. 12 and Table 4) and we proposed a hypothetical tsunami scenario for this earthquake. The faulting area and vertical displacement were reckoned to be about 95 km (fault length) × 20 km (fault width) and 5 m (Table 4), respectively. Simulation results showed the height of initial tsunami wave to be 0.612 m. The crest and trough amplitudes were found as 0.212 m and −0.4 m, respectively. Initial wave height was less than the heights of other historical tsunamigenic earthquakes which had about the same magnitude. The reason was that the assumption of a large amount of strike slip component for this earthquake. Results also showed a NW–SE directed tsunami wave propagation. The most destructive tsunami waves were calculated along the coastal plains of the Karpathos Island (Fig. 14a,b,c). The distribution of maximum positive tsunami wave amplitudes exhibited ~1.2 m tsunami wave height along the northern coastal plains and ~40 cm along the southern coastal plains of Eastern Mediterranean (Fig. 14c). However, they were not too high when compared to heights of the other tsunamigenic Eastern Mediterranean earthquakes. Hence, we suggested that 1948 Karpathos tsunami was observed only near the earthquake source area and had local effects and destructions. These findings are in consistent with historical documents and records. Other Eastern Mediterranean coasts such as African, Levantine and Turkish coastal plains were not affected from tsunami waves related to 1948 tsunami (Fig. 14b,c).

3.2.2. Crete–Hellenic Arc region

3.2.2.1. The July 21, 365 earthquake (M~8.5)–W Crete. It is widely reported that a catastrophic earthquake, occurred near the western part of Crete on July 21, 365 (Fig. 12), destroyed a large area in Eastern Mediterranean. It particularly devastated all towns on Crete Island and most of Eastern Mediterranean coastal plains up to the

Nile Delta by killing thousands of people and hurling ships to inland. Many researchers and historians continue to debate the question whether ancient sources refer to a single catastrophic earthquake in 365 AD, or whether they represent a historical amalgamation of a number of earthquakes occurring between 350 AD and 450 AD (Stiros, 2001, 2010; Stiros and Drakos, 2006). Archaeological evidences pointed out that this earthquake mainly destroyed the ancient town of Kisamos, a wealthy Roman town in Western Crete. Hence, earthquake epicenter was assumed to be located at the western part of the Hellenic subduction zone (Fig. 12). In addition, Pirazzoli et al. (1992) presented two tsunami deposits correlated with 365 AD event near the ancient harbor of Phalasarna in the western Crete, which is presently 6–7 m above the water. Furthermore, uplift analysis indicated that 365 AD earthquake had a magnitude of ~8.5 (Fischer and Babeyko, 2007; Shaw et al., 2008). So far, many numerical tsunami studies related to this earthquake were done (e.g. Fischer and Babeyko, 2007; Lorito et al., 2008; Shaw et al., 2008) and destructive tsunami waves along Crete, Nile Delta, African and Adriatic coasts were reported. But they did not illustrate any synthetic tsunami wave amplitudes at pseudo tide-gauge locations along different parts of the Eastern Mediterranean Sea especially African, Arabian and Anatolian coastal plains. In order to demonstrate the overall effects of this tsunamigenic earthquake, we applied a hypothetical tsunami scenario and obtained synthetic wave amplitudes at several pseudo tide-gauge locations in Eastern Mediterranean (Figs. 12 and 15a,b,c).

Simulation of the 365 AD Crete earthquake-induced tsunami has been widely speculated with various debates based on diverse rupture parameters estimated (Fischer and Babeyko, 2007; Shaw et al., 2008). We suggested thrust faulting mechanism with a shallow focal depth for this earthquake in the light of previous focal mechanism solutions, current plate motions and tectonic structures along the Hellenic subduction zone (Benetatos et al., 2004; Kiratzi and Louvari, 2003; Laigle et al., 2004; Shaw and Jackson, 2010; Taymaz et al., 1990, 1991, 2007a, 2007b; Yolsal, 2008; Yolsal et al., 2007). We adopted the fault length, fault width, and vertical displacement as 200 km, 50 km and 15 m, respectively. Water surface fluctuations at all grid points were obtained and snapshots of tsunami wave propagations at 10 min intervals were displayed (Fig. 15a). The height of initial tsunami wave was calculated as

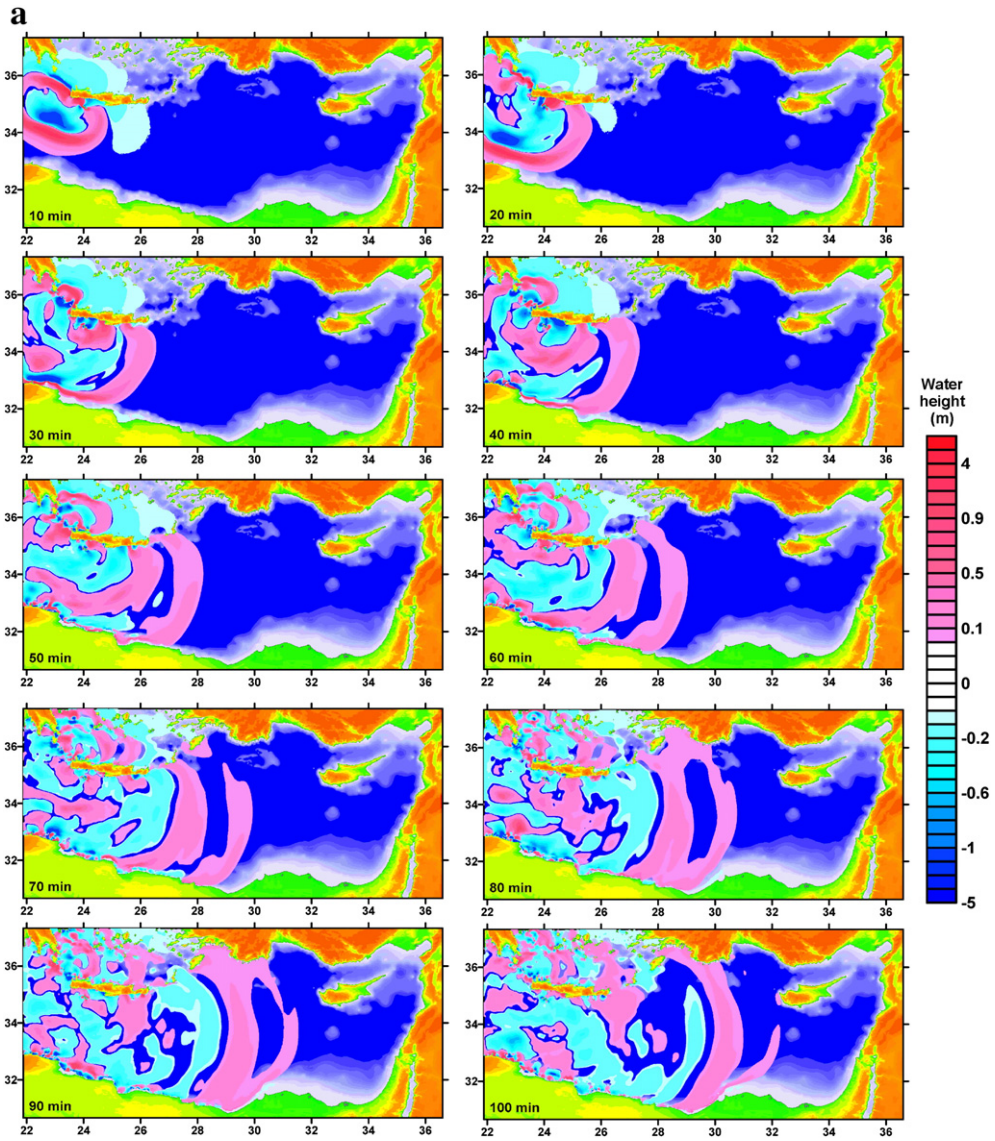

Fig. 15. a. Snapshots of sea states at different time steps (t = 10, 30, 50, 70, 90 min) generated by non-linear shallow water theory for various times at 10 min intervals for the July 21, 365 AD Crete earthquake. The color scale which is given on the right-hand side in meters shows the water height values.b. Computed tsunami records at selected locations for the July 21, 365 AD Crete earthquake. Header information is as in Fig. 13b.c. Distribution of maximum positive tsunami wave amplitudes along the north and south coasts of the Eastern Mediterranean and directivity of tsunami wave propagation during the July 21, 365 AD Crete earthquake.

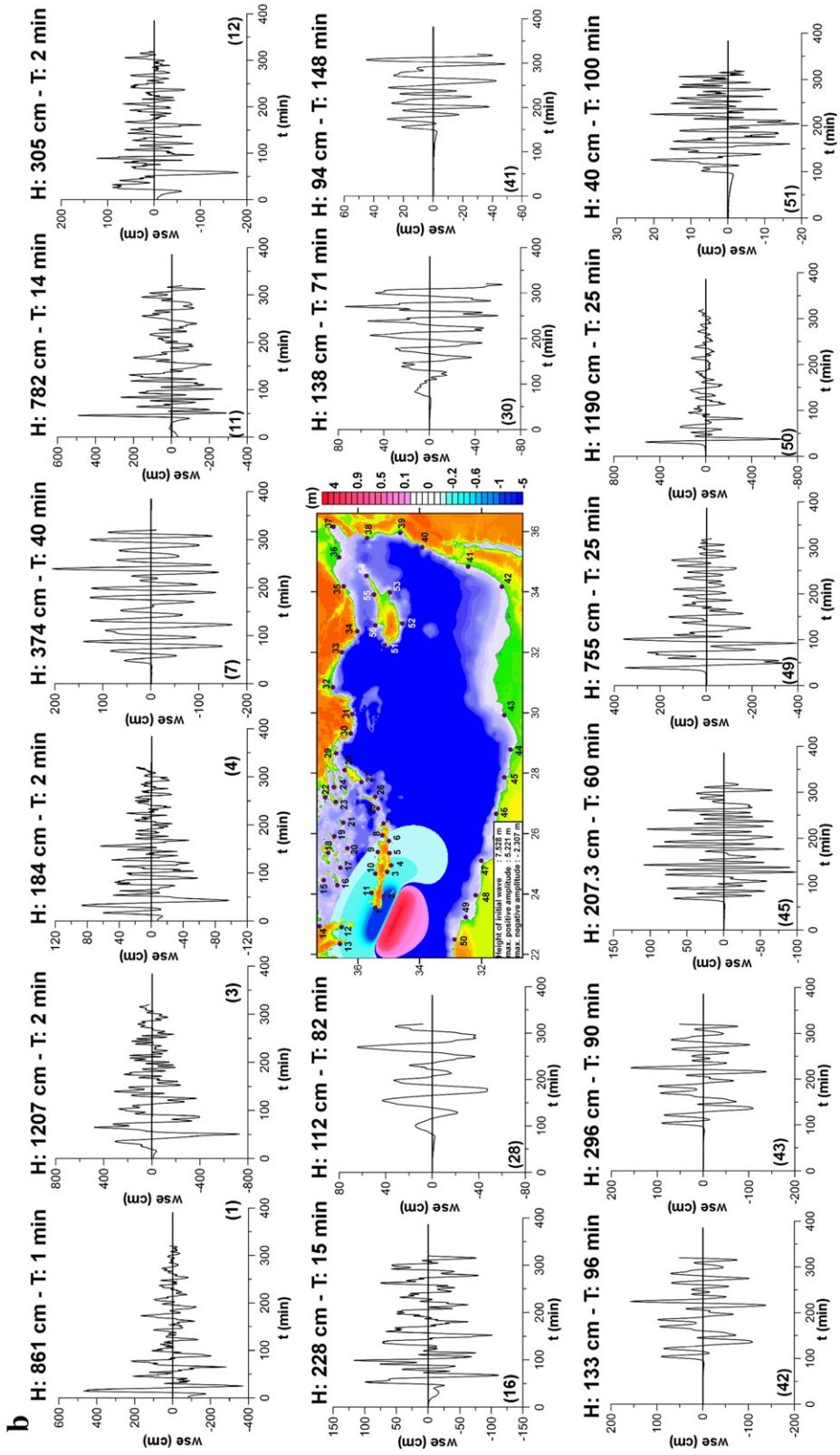

Fig. 15 (*continued*).

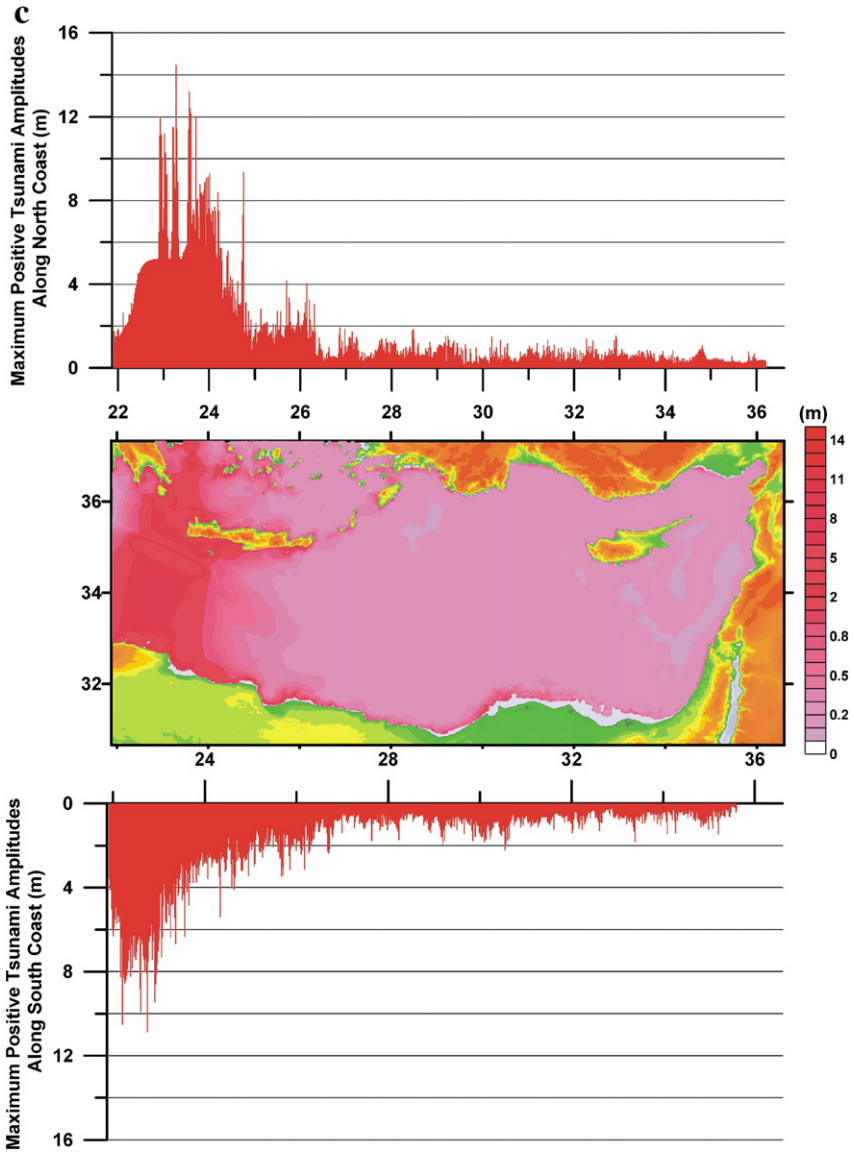

Fig. 15 (*continued*).

7.528 m (Fig. 15b). The computed water surface elevations (wse) and theoretical arrival times were presented at selected pseudo tide-gauge locations in Fig. 15b. We determined maximum tsunami wave heights near Crete (~12 m at location 3), Libyan–African coasts (~11 m at location 50), Alexandria–Nile Delta (~3 m at location 43), Fethiye (SW Turkey; ~1.5 m at location 30), Israel coasts (~1.5 m at location 42), Dodecanese islands (~1–2 m), Rhodes (~1 m at location 28) and Antalya, Alanya and SW Cyprus (~40–70 cm) (Fig. 15b,c). Finally, we suggest that our results are consistent with historical documents, reports, catalogues, observations, and they reflect catastrophic tsunami waves resulted from 365 AD earthquake along the Eastern Mediterranean coastal plains.

3.2.2.2. The 08 August 1303 earthquake (M~8.0)—SE Crete. This earthquake is known as one of the largest and best-documented seismic events in the Eastern Mediterranean Sea region throughout its history. It has been reported that the earthquake epicenter was possibly located near the eastern part of Crete, and it occurred related to the Hellenic subduction zone at a shallow focal depth (Fig. 12 and Table 4). Historical documents and trench analysis demonstrated that a large area including Crete, the Peloponnese, Rhodes, Antalya (SW Turkey), Cyprus, Alexandria–Nile Delta (Egypt) coastal plains had been seriously affected from this catastrophic earthquake (Altınok and Ersoy, 2000; Ambraseys, 1962; Ambraseys et al., 1994; Antonopoulos, 1980; Guidoboni and Comastri, 1997, 2005a, 2005b; Yolsal et al., 2007). Yolsal et al. (2007) suggested strike, dip and rake angles and source depth of this earthquake as 115°, 45°, 110°, 20 km, respectively. Furthermore, they also estimated the amount of vertical displacement and faulting area using empirical equations developed by Mai and Beroza (2000), Tan and Taymaz (2006), and Wells and Coppersmith (1994). Initial tsunami wave height was found to be 2.444 m. The details of tsunami simulations can be found in Yolsal (2008) and Yolsal et al. (2007). However, in this article we briefly summarized numerical simulation results of the August 08, 1303 Crete earthquake by showing tsunami wave propagation and the distribution of maximum positive tsunami wave amplitudes along the northern and southern coasts of Eastern Mediterranean (Fig. 16a,b). As seen in Fig. 16b, the largest wave amplitudes were calculated at the eastern part of Crete (~6 m). It was also observed that tsunami wave amplitudes should be destructive along the southern coastal plains such as Alexandria (Nile Delta) and Libyan coastlines (~1.5 m).

3.2.2.3. The July 01, 1494 earthquake (M~7.0–7.5)—S Crete. Another large tsunamigenic earthquake occurred at the vicinity of southern Crete on July 01, 1494 (Ambraseys, 1962; Ambraseys et al., 1994; Antonopoulos, 1980; Guidoboni and Comastri, 2005a; Papadopoulos, 2001; Soloviev et al., 2000) (Fig. 12). This earthquake was strong enough to create a local tsunami at the Candia (Iraklion) harbor. All the ships at anchor struck violently against each other to the extent that they seemed likely to break up. Historical documents also pointed out tsunami waves reaching to the Levantine Basin as far as Jaffa and Israel coasts. Guidoboni and Comastri (2005a) suggested an epicentral coordinates of 35.12′ N and 24.55′ E and an intensity of I_o = VIII–IX for this earthquake which corresponds to the earthquake magnitude of about M~7.5 (Table 4).

By taking into consideration of earthquake focal mechanism solutions, the geometry of the Hellenic subduction zone and current plate boundaries near the epicenter, we suggested earthquake source parameters indicating thrust faulting mechanism with a small amount of strike slip component. The strike, dip and rake angles were assumed to be 110°, 50° and 80°, respectively (Fig. 12 and Table 4). Similar to the other numerical tsunami simulations, we approximately calculated the faulting area (fault length and fault width) and vertical displacement for M~7.0–7.5 sized earthquakes by using several empirical seismological equations (Mai and Beroza, 2000; Tan and Taymaz, 2006; Wells and Coppersmith, 1994). We assumed the focal depth to be 15 km. The water surface fluctuations at all grid points were computed and displayed as snapshots of tsunami wave propagations at 10 min intervals in Fig. 17. The height of initial tsunami wave was calculated to be 1.281 m. We also demonstrated water surface elevations at selected pseudo tide-gauge locations (Fig. 17b). Distribution of computed maximum positive tsunami amplitudes along the northern and southern coastal plains (Fig. 17c) showed NE–SW directed wave propagations so as to be at right angles to the major axis of tsunami source, as was predicted in theoretical models (see Pelinovsky, 1996). Hence, we obtained largest wave amplitudes (Fig. 17b) near Crete (~1 m at locations 1 and 2) and African coasts (~2 m at locations 46 and 48). We observed that other parts of Crete were not severely affected by tsunami waves. There were also no significant tsunami wave amplitudes at Cyprus (~12 cm at location a), Alexandria–Egypt, Turkish and Levantine coastal plains (see Fig. 17b,c).

4. Summary and discussion

This study exhibits that present-day deformation along the Hellenic subduction zone is mainly driven by a convergence between the African and Aegean plates. It also shows that seismic deformation is not uniformly distributed throughout the region. The topography and bathymetry along the Hellenic subduction zone reflect deformation styles such as extensions and compressions. We observe major effects of tectonic structures which are related to complex tectonic evolution and deformation patterns on earthquake source parameters and tsunami wave characteristics. During the period of 2000–2008, there were no catastrophic earthquakes in the study area; earthquakes are generally moderate size ($5.0 \leq M_w \leq 6.5$; Table 1). Most of our observations are

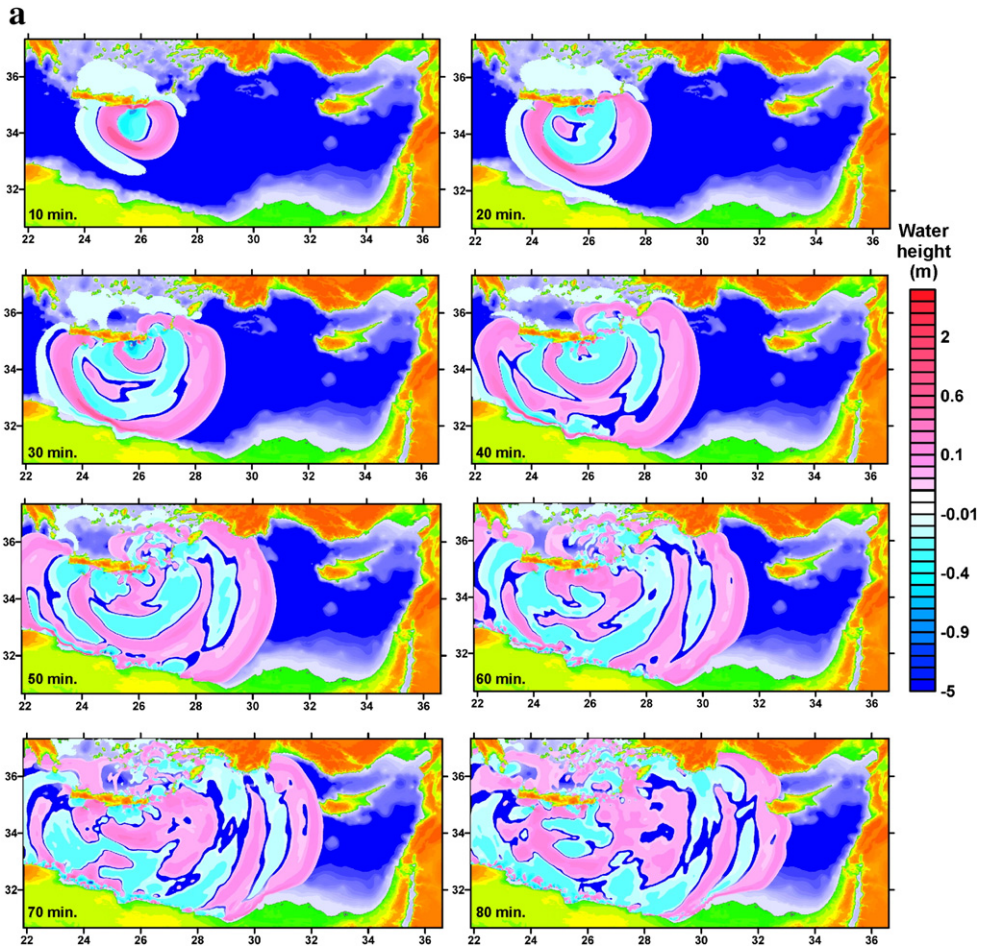

Fig. 16. a. Snapshots of sea states at different time steps (t = 10, 30, 50, 70 min) generated by non-linear shallow water theory for various times at 10 min intervals for the August 08, 1303 Crete earthquake. The color scale which is given on the right-hand side in meters shows the water height values.b. Distribution of maximum positive tsunami wave amplitudes along the north and south coasts of the Eastern Mediterranean and directivity of tsunami wave propagation during the August 08, 1303 Crete earthquake.

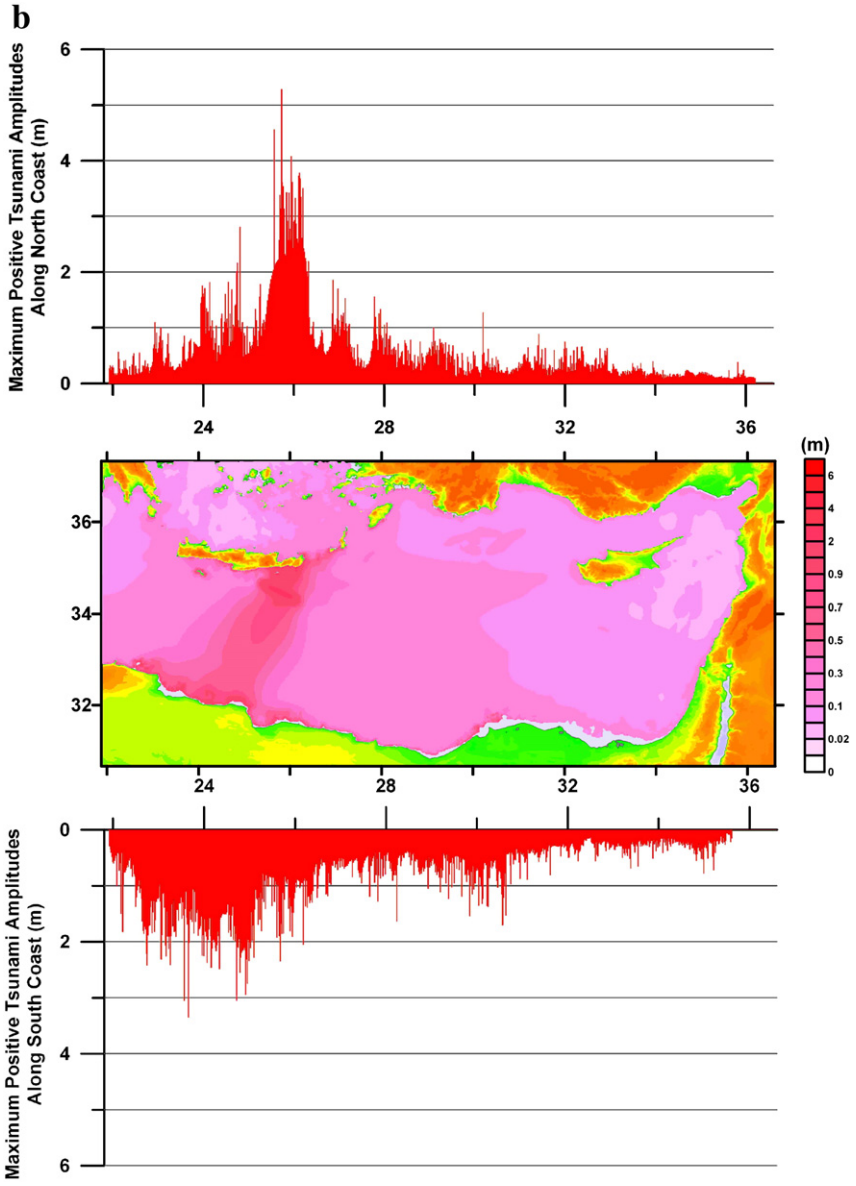

Fig. 16 (*continued*).

concerned with the southern part of the Aegean and Eastern Mediterranean Seas since intense earthquake activity is mainly concentrated along the Hellenic subduction zone. We calculated low stress drop values ($\Delta\sigma < 30$ bars) indicating typically interplate seismic activity. Similar to previous seismological studies (e.g. Benetatos et al., 2004; Bohnhoff et al., 2005; Louvari, 2000; Papazachos and Kiratzi, 1996; Shaw and Jackson, 2010; Taymaz et al., 1990, 1991), we confirm and therefore classify earthquakes into three major categories: [1] focal mechanisms of earthquakes exhibiting E–W extension within the Aegean overriding plate; [2] earthquakes related to the African–Aegean convergence; and [3] focal mechanisms of earthquakes lying within the subducting African plate (Fig. 4a,b,c). Below we summarize current active tectonics and tsunami potential on the Hellenic subduction zone along with source mechanisms, slip distributions, rupture propagations, earthquake activity and numerical tsunami simulation results. Furthermore, various tectonic models as indicated by local geology, geodesy (GPS, InSAR as such), paleoseismology, and geophysics (gravity, magnetic, seismic refraction and reflection) help us to conclude the overall tectonic activity of the region.

[1] *Overriding Aegean Plate and the eastern part of the Hellenic subduction zone:* Source parameters of earthquakes occurred in the east of the Hellenic subduction zone mostly indicate normal faulting mechanisms with left-lateral transtensional components and shallow focal depths (h ~ 8–10 km) (e.g., July 20,1996; October 12, 2002; May 01, 2001; February 07, 2004 earthquakes). We suggest that source mechanisms and focal depths of these earthquakes expose the overriding Aegean plate (Fig. 4a). This area consists of the Ptolemeus, Pliny and Strabo deep-sea depressions. T-axes directions show E–W and NW–SE extensional forces. Shaw and Jackson (2010) emphasized that GPS vectors manifest the largest divergence in azimuth between 25°E–29°E, and support the dominant extension which occurs rapidly in the east of the subduction zone based on the observations of Reilinger et al. (2006). Farther north–west, similar to the eastern part of the Hellenic arc, we find normal faulting mechanisms with small amounts of strike slip components (e.g., May 24, 2000 and October 17, 2003 earthquakes) along the inner part of the shallow crustal layer ($h < 15$ km; Fig. 4a). These earthquakes might be related to thick unconsolidated sediments on the downgoing African plate and aseismic interface deeper than ~45 km due to the thermal and dewatering effects (Shaw and Jackson, 2010).

While we observe the dominant extensional motion in the east and west of the Hellenic arc, we cannot find any evidence of normal faulting earthquakes at south of Crete. We also suggest that dominant source mechanisms dramatically change from normal to strike slip faulting mechanisms with thrust components towards the east of Rhodes (e.g., June 23, 2001; October 30, 2001; January 23–30, 2005 and July 15, 2008 earthquakes). These earthquakes have relatively deeper focal depths (~35–40 km). We propose that they probably occurred on the downgoing African plate (Fig. 4c). Further, we determine slip distributions of earthquakes which have simple and circular-shaped ruptures with short source durations. Ruptures generally propagated along dip directions of fault planes.

[2] *African–Aegean convergence:* Shaw and Jackson (2010) reported that earthquakes along the Hellenic Subduction Zone account for less than 10% of the African–Aegean convergence. However, the number of moderate-sized earthquakes is good enough to define the geometry and depth of the subduction interface. In this study, source parameters of earthquakes related to the convergence between African and Aegean plates (h<45 km) show that the outer part of the Hellenic Subduction Zone, especially the south of Crete, is deforming by thrust faulting mechanisms with strike slip components (e.g., February 22, 2000; April 05, 2000 and March 28, 2008 earthquakes; Fig. 4b). P-axes directions mostly present N–S and NE–SW compressional motions. These shallow-depth thrust faulting mechanisms are also responsible for catastrophic tsunamis such as tsunamigenic 365 AD earthquake. The March 28, 2008 (M_w 5.5) earthquake is a good example reflecting the African–Aegean convergence in the study region. It shows north-dipping low-angle thrust faulting mechanism with a small amount of left-lateral strike slip component at south of Crete. Teleseismic slip and rupture models generally exhibit seismic moment releases and large displacement values mainly occurred at focal depths. They have uniform rupture propagations on faulting

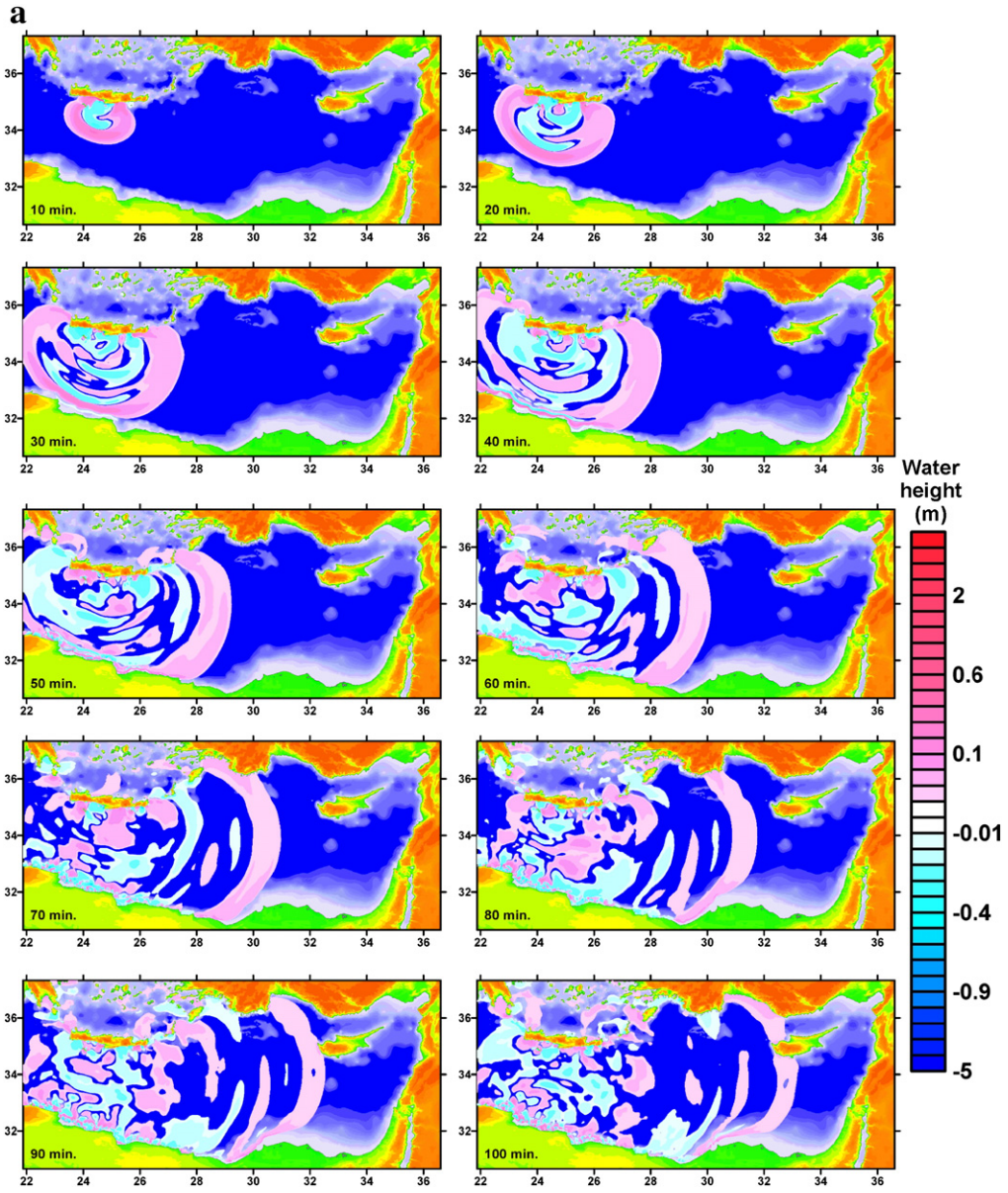

Fig. 17. a. Snapshots of sea states at different time steps (t = 10, 30, 50, 70, 90 min) generated by non-linear shallow water theory for various times at 10 min intervals for the July 01, 1494 Crete earthquake. The color scale which is given on the right-hand side in meters shows the water height values.b. Computed tsunami records at selected locations for the July 01, 1494 Crete earthquake. Header information is as in Fig. 13b.c. Distribution of maximum positive tsunami wave amplitudes along the north and south coasts of the Eastern Mediterranean and directivity of tsunami wave propagation during the July 01, 1494 Crete earthquake.

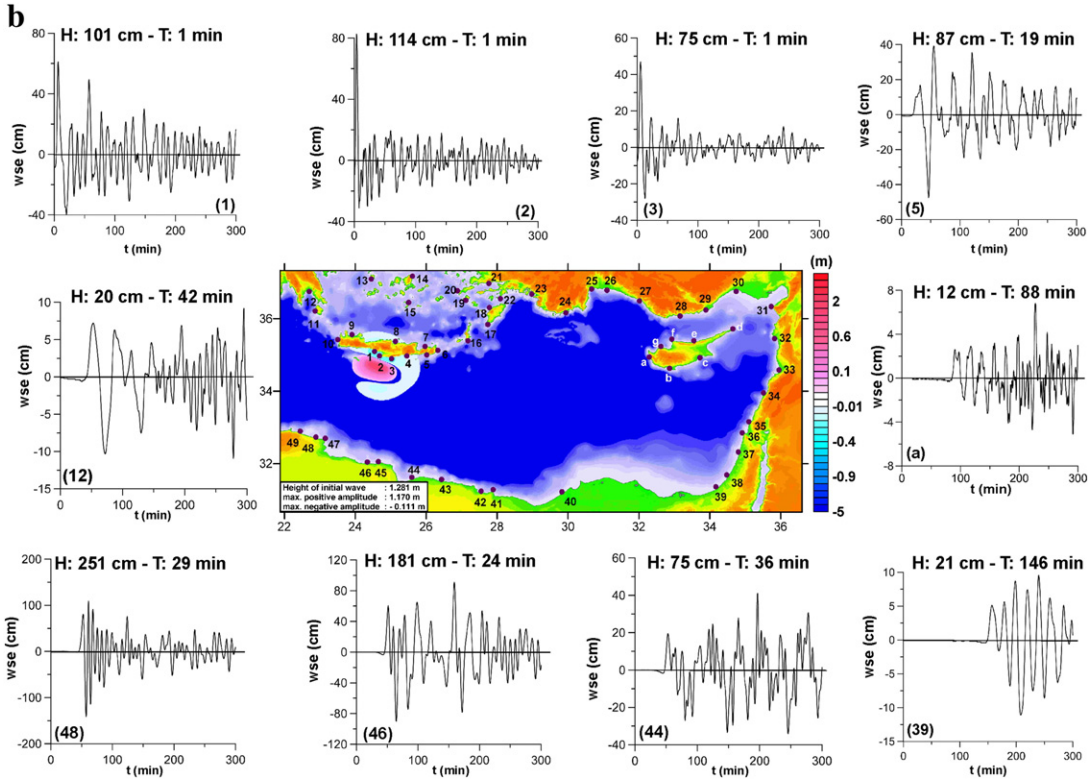

Fig. 17 (*continued*).

planes. The overall source time functions for complete ruptures show that most of the seismic energy is released in the first 5–10 s (Table 3).

[3] *Earthquakes in the subducting African Plate:* Earthquake source studies are important to define the position and depth of the subducting African plate. Along the Hellenic Subduction Zone, deep-focus earthquakes ($h > 45$ km) are mostly related to the downgoing African plate and they show mainly strike slip faulting mechanisms with considerable amount of thrust components (e.g., January 22, 2002 and May 21, 2002 earthquakes; Table 1). We summarize the earthquakes whose depths, locations and mechanisms make it likely they occurred within the subducting lithosphere in Fig. 4c. These earthquakes exhibit down-dip extension which is parallel to the dip of the subducting African plate and they have T-axes aligned ~N–S, indicating the expected pull of the subducting slab (Taymaz et al., 1990). Source mechanisms generally have P- axes parallel to the local strike of the subduction zone at south of Crete and they expose the along-strike shortening of the African lithosphere which may be related to the strong curvature of the Hellenic subduction zone. Similarly, Shaw and Jackson (2010) pointed out that earthquakes ($h < 410$ km) where seismically-active slabs did not penetrate as deep as 670 km generally had down-dip T-axes. Our results display the similar faulting geometry and T-axes directions which are consistent with previous seismological studies. Additionally, at north western part of Crete Island, there are earthquakes indicating dominantly thrust faulting mechanisms (e.g., November 04, 2004 and January 08, 2006 earthquakes) at about 60–65 km focal depth. They occurred on a fracture zone called as right-lateral strike slip Kythira fault. This zone is vertical to the boundary of African and Aegean plates along the south-western section of the Hellenic arc. It is known that this part of the Eastern Mediterranean lithosphere reflects high deformation rate and it accounts for over 60% of the seismic-energy release in Europe. Papazachos (1996) suggested that deformation in this area could lead to earthquakes as large as M_w 8.3. Rupture propagations are not too simple and uniform for these earthquakes. For example, slip inversion model of the January 08, 2006 showed complex slip distributions along dip of the fault plane. Seismic moment of this earthquake was released in two main slip patches on the fault which propagate upwards direction.

[4] Numerical tsunami studies clearly reveal the importance of seismological studies which are related to earthquake source mechanisms, focal depth, bathymetry data and geomorphology of any adjacent land for identifying the large-earthquake-prone regions along the subduction zones. Our results indicate non-uniform wave propagations in Eastern Mediterranean Sea correlated with the complex sea bottom and coastal topography. We observe that tsunami waves reach all Eastern Mediterranean coastal plains at most in 3 hours. But sea wave disturbances may continue for a long time due to the reflections and refractions from the bathymetrical features, islands, bays, and coastal plains. We suggest that future oceanographic and marine geophysical research should aim to improve the resolution of bathymetric maps, particularly for the details of continental shelf, and those of seamounts. Simulations also expose that damaging historical tsunami waves in the eastern (e.g., 1303 and 1481) and western Hellenic arc (e.g., 365 AD, 1494) are able to threaten especially the coastal plains of the Crete, SW Turkey, Dodecanese, Cyprus, Levantine, and Nile Delta regions, consistent with the historical catalogues, documents, and reported field observations. Thus special care should be considered in the evaluation of the tsunami risk assessment for these regions (Fig. 12). However, synthetic tsunami wave amplitudes calculated for Cyprus and Levantine Basin tsunamigenic earthquakes are not high enough to demolish SW Turkey, African, Dodecanese and Crete Islands coasts. They have especially local effects, only damaged the regions nearby earthquake epicenters. Hence, we think that the Cyprus Island acts as a

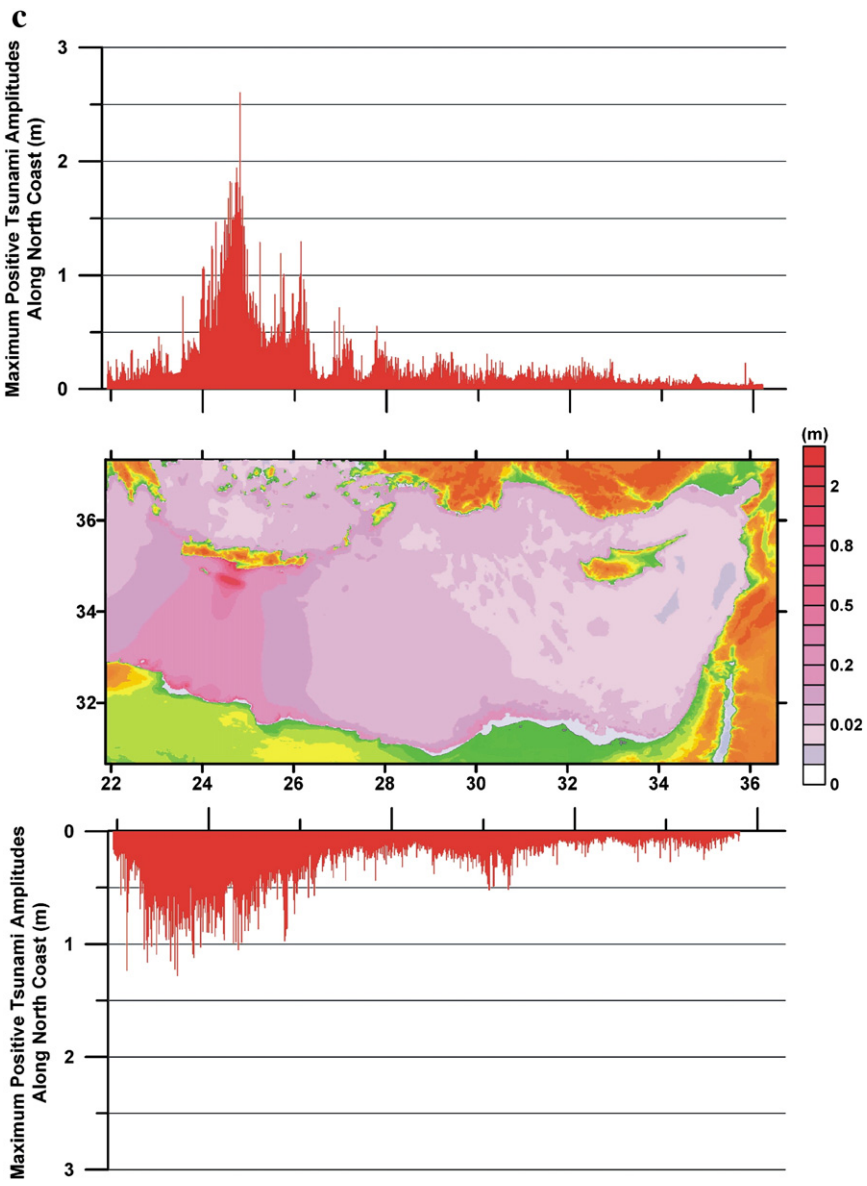

Fig. 17 (*continued*).

natural barrier for tsunami waves in case of the occurrence of earthquakes along the Cyprus Arc and Levantine Basin (Figs. A8-A9 in Appendix).

Finally, we conclude that complexities of the Eastern Mediterranean region are correlated with structural variations and intense deformations. We emphasize the importance of combined seismological results on tsunami studies as they are used to set initial boundary conditions for numerical simulations, and suggest that tsunami simulations can be further improved by implementing better geophysical, seismological and geological observations in the future.

Acknowledgements

This work is part of Ph.D. Thesis by Yolsal (2008). We would like to thank İstanbul Technical University Research Fund (İTÜ-BAP), Turkish National Scientific, Technological Foundation (TÜBİTAK), Turkish Academy of Sciences (TÜBA) in the framework for Young Scientist Award Program for their support (TT-TÜBA-GEBIP 2001-2-17), and Alexander von Humboldt-Stiftung (AvH). Generic Mapping Tools (GMT; Wessel and Smith, 1998) and SAC2000 softwares (Goldstein and Snoke, 2005; Goldstein et al., 2003) were used to prepare figures and to process conventional earthquake data, respectively. Authors also thank to Nobuo Shuto, Fumihiko Imamura, Andrey Zaytsev, Anton Chernov, Efim Pelinovsky, Andrey Kurkin and Ahmet C. Yalçıner for their precious efforts and supports for developments of the numerical simulation codes, namely TUNAMI-N2 and AVI-NAMI. Careful reviews by two anonymous referees resulted in considerable improvement to an earlier version of this manuscript. We are particularly indebted to *Editor-In-Chief* Hans Thybo for his judicious insightful remarks.

Appendix A

In Appendix, we summarize earthquakes which are previously reported by other studies and Harvard-CMT moment tensor catalogue (Tables A1–A3). We could not find source mechanism parameters of several earthquakes occurred during 2000–2008 listed in these tables, due to the lack of P- and SH-waveform data that have good signal/noise ratio. As an example of uncertainty analysis, we demonstrated the tests for strike, dip, rake angles and focal depth

Table A1
Source parameters of earthquakes occurred within the overriding Aegean plate along the eastern and western parts of the Hellenic Subduction Zone reported by previous studies. L88: Lyon-Caen et al. (1988); T90: Taymaz et al. (1990); HRV-CMT: Harvard-CMT; KL03: Kiratzi and Louvari (2003); B04: Benetatos et al. (2004); and SJ10: Shaw and Jackson (2010). M_w: moment magnitude, M_o: seismic moment, t_o: origin time, h: focal depth of the earthquake.

Date (d.m.y)	Origin time (to) (h:m:s)	Lat. (°N)	Long. (°E)	M_w	Strike (°)	Dip (°)	Rake (°)	h (km)	Ref.
27.04.1965	14:09:05	35.65	23.53	5.4	191	65	−79	13	L88
29.11.1973	10:57:44	35.18	23.81	5.8	224	67	10	18	T90
13.09.1986	17:24:34	37.07	22.14	5.8	196	51	−90	8	L88
02.10.1986	10:12:45	34.81	28.30	5.2	99	37	−53	15	HRV-CMT
05.09.1988	20:03:25	34.44	26.55	5.2	15	55	−11	15	HRV-CMT
20.11.1988	21:01:06	35.29	28.70	5.4	24	32	−152	15	HRV-CMT
09.07.1990	11:22:18	34.94	26.62	5.2	217	56	−21	9	KL03
19.03.1991	12:09:22	34.79	26.31	5.5	261	30	40	12	KL03
30.04.1992	11:44:39	35.06	26.63	5.8	214	52	−47	7	KL03
22.07.1996	01:44:37	36.08	27.12	5.0	223	36	−78	15	HRV-CMT
09.04.2006	23:27:19	35.17	27.24	5.3	144	36	−117	26	HRV-CMT
13.08.2006	10:35:12	34.35	26.56	5.1	197	43	−1	17	SJ10
21.05.2007	16:39:10	35.06	27.74	5.0	1	39	−146	18	HRV-CMT
23.09.2007	00:54:29	35.11	27.06	5.3	234	41	−23	18	HRV-CMT

Table A2
Source parameters of earthquakes occurred related to the African–Aegean convergence reported by previous studies. Mc72: McKenzie (1972); T90: Taymaz et al. (1990); HRV-CMT: Harvard-CMT; B04: Benetatos et al. (2004); and SJ10: Shaw and Jackson (2010). M_w: moment magnitude, M_o: seismic moment, t_o: origin time, h: focal depth of the earthquake.

Date (d.m.y)	Origin time (to) (h:m:s)	Lat. (°N)	Long. (°E)	M_w	Strike (°)	Dip (°)	Rake (°)	h (km)	Ref.
09.05.1966	00:42:53	34.43	26.44	5.5	132	46	110	16	T90
30.05.1968	17:40:26	35.45	27.88	6.0	314	25	119	21	Mc72
14.01.1969	23:12:06	36.11	29.19	6.3	100	74	82	33	Mc72
16.04.1969	23:21:06	35.23	27.72	5.5	104	80	85	45	Mc72
04.05.1972	21:39:57	35.15	23.56	6.2	112	74	98	41	T90
18.08.1977	09:27:40	35.27	23.51	5.5	114	79	96	38	T90
11.09.1977	23:19:19	34.94	23.05	5.9	276	47	89	19	T90
15.05.1979	06:59:22	34.58	24.44	5.7	253	17	65	35	T90
15.06.1979	11:34:16	34.93	24.20	5.6	150	75	70	40	T90
21.06.1984	10:43:40	35.30	23.28	6.0	110	72	83	39	T90
22.05.1986	19:52:22	34.64	26.52	5.3	118	86	99	27	B04
07.12.1995	18:00:54	34.81	24.09	5.1	344	16	126	19	SJ10
13.10.1997	13:39:36	36.34	22.10	6.3	300	18	86	26	SJ10
05.11.1997	12:22:50	34.65	23.95	5.1	358	26	153	19	SJ10
17.04.1999	08:17:56	35.95	21.71	5.3	172	59	95	27	SJ10
25.11.2005	09:30:55	35.07	23.51	5.2	300	23	72	40	SJ10
22.08.2006	09:23:21	35.07	27.09	5.1	5	10	8	12	HRV-CMT
10.05.2008	20:53:04	36.31	22.19	5.4	329	4	122	20	HRV-CMT

Table A3
Source parameters of earthquakes lying within the subducting African Plate reported by previous studies. T90: Taymaz et al. (1990); HRV-CMT: Harvard-CMT; P01: Parke (2001); B04: Benetatos et al. (2004); and SJ10: Shaw and Jackson (2010). M_w: moment magnitude, M_o: seismic moment, t_o: origin time, h: focal depth of the earthquake.

Date (d.m.y)	Origin time (t_o) (h:m:s)	Lat. (°N)	Long. (°E)	M_w	Strike (°)	Dip (°)	Rake (°)	h (km)	Ref.
09.04.1965	23:57:02	35.06	24.31	6.1	63	76	157	51	T90
12.06.1969	15:13:30	34.43	25.04	6.0	163	50	44	19	T90
22.09.1975	00:44:56	35.19	26.25	5.6	209	75	131	64	T90
28.11.1977	02:59:09	35.95	27.78	5.6	88	51	32	66	B04
22.08.1979	20:12:47	35.89	27.38	5.3	64	31	−106	68	B04
17.08.1982	22:22:19	33.70	22.94	6.3	230	45	109	39	T90
03.01.1983	00:12:25	34.53	24.31	5.1	30	36	70	102	HRV-CMT
19.03.1983	21:41:41	35.01	25.32	5.6	44	51	139	67	T90
27.09.1983	23:59:38	36.71	26.93	5.4	312	46	162	170	HRV-CMT
22.05.1984	13:57:04	35.82	22.57	5.1	188	44	32	63	B04
27.09.1985	16:39:46	34.40	26.54	5.8	125	77	9	38	T90
12.04.1987	02:47:20	35.51	23.41	5.1	252	90	180	15	HRV-CMT
19.06.1987	18:45:42	36.79	28.18	5.2	121	41	88	65	B04
18.10.1991	14:04:55	35.75	28.45	5.2	82	88	13	43	B04
21.11.1992	05:07:21	35.85	22.50	5.9	194	53	28	54	P01
23.05.1994	06:46:15	35.54	24.69	6.7	64	77	163	75	P01
12.04.1996	15:39:10	36.58	27.04	5.2	235	80	−52	162	B04
26.04.1996	07:01:27	36.33	27.96	5.3	343	54	174	70	B04
09.03.1998	11:21:18	35.88	28.40	5.1	10	33	−116	54	HRV-CMT
29.04.2003	01:51:20	36.93	21.73	5.1	193	81	4	56	HRV-CMT
13.09.2003	13:46:14	36.61	26.87	5.2	97	40	10	160	HRV-CMT
07.10.2004	01:05:12	36.46	26.79	5.5	334	40	166	130	HRV-CMT
04.08.2005	10:45:28	34.83	26.50	5.0	90	80	7	31	HRV-CMT
06.01.2008	05:14:21	37.25	22.70	6.0	218	45	20	68	SJ10

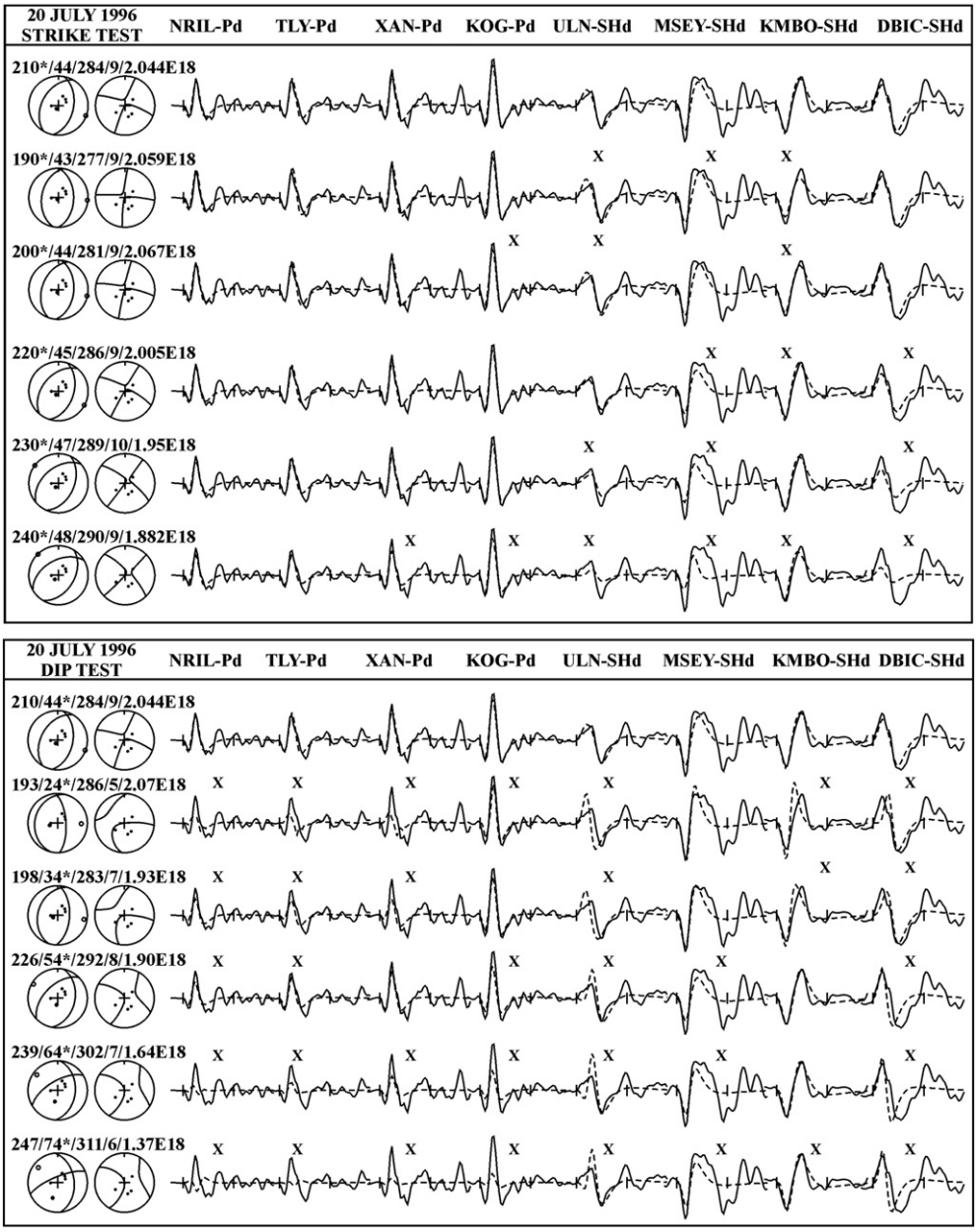

Figure A1. An example of uncertainty tests for strike and dip angles of the July 20, 1996 Dodecanese earthquake. The top row shows selected waveforms from the minimum misfit solution. The stations are identified at the top of each column, with the type of waveform marked by P- and SH- and followed by the instrument type. At the start of each row are the P and SH focal spheres for the focal parameters represented by the five numbers (strike, dip, rake, depth and seismic moment), showing the positions on the focal spheres of the stations chosen. X show matches of observed to synthetic waveforms that are worse than in the minimum misfit solution. Fixed strike and dip angles are marked by *.

belong to the July 20, 1996 Dodecanese Islands (M_w 6.1) earthquake (Figs. A1, A2).

We also illustrated distributions of P-wave first motion polarities of five Eastern Mediterranean earthquakes discussed individually in the text (see Section 3.1.1). P-waveforms are recorded by seismic stations at teleseismic and regional distances. Black and white circles show up (compressional) and down (dilatational) P-wave polarities, respectively. They are used to further constrain the inversion solutions (Figs. A3–A7).

In addition, we briefly explained numerical tsunami simulation results of tsunamigenic 1222 Cyprus Arc (Fig. A8) and 1822 Levantine Basin (Fig. A9) earthquakes. Thus, we demonstrated the effects of tsunamigenic earthquakes occurred at different parts of the study region on Eastern Mediterranean coastal plains.

The May 11, 1222 earthquake—Paphos, Cyprus

According to historical and archaeological documents, Limassol, Nicosia and especially Paphos where the castle collapsed, were severely affected from the 1222 tsunamigenic Cyprus earthquake (Fig. 12; Table 4). There were many victims and loses. This earthquake was felt in regions as far as Alexandria (Altınok and Ersoy, 2000; Ambraseys, 1962; Ambraseys et al., 1994; Calvi, 1941). We briefly presented tsunami wave propagations of the 1222 Paphos earthquake in this article to discuss the importance of the Cyprus Arc and different tectonic complexities on tsunami studies (Fig. A8). Yolsal et al. (2007) proposed a hypothetically tsunami scenario for this earthquake. They used current plate boundaries and focal mechanism solutions of earthquakes occurred along the Cyprus Arc in order to estimate source parameters.

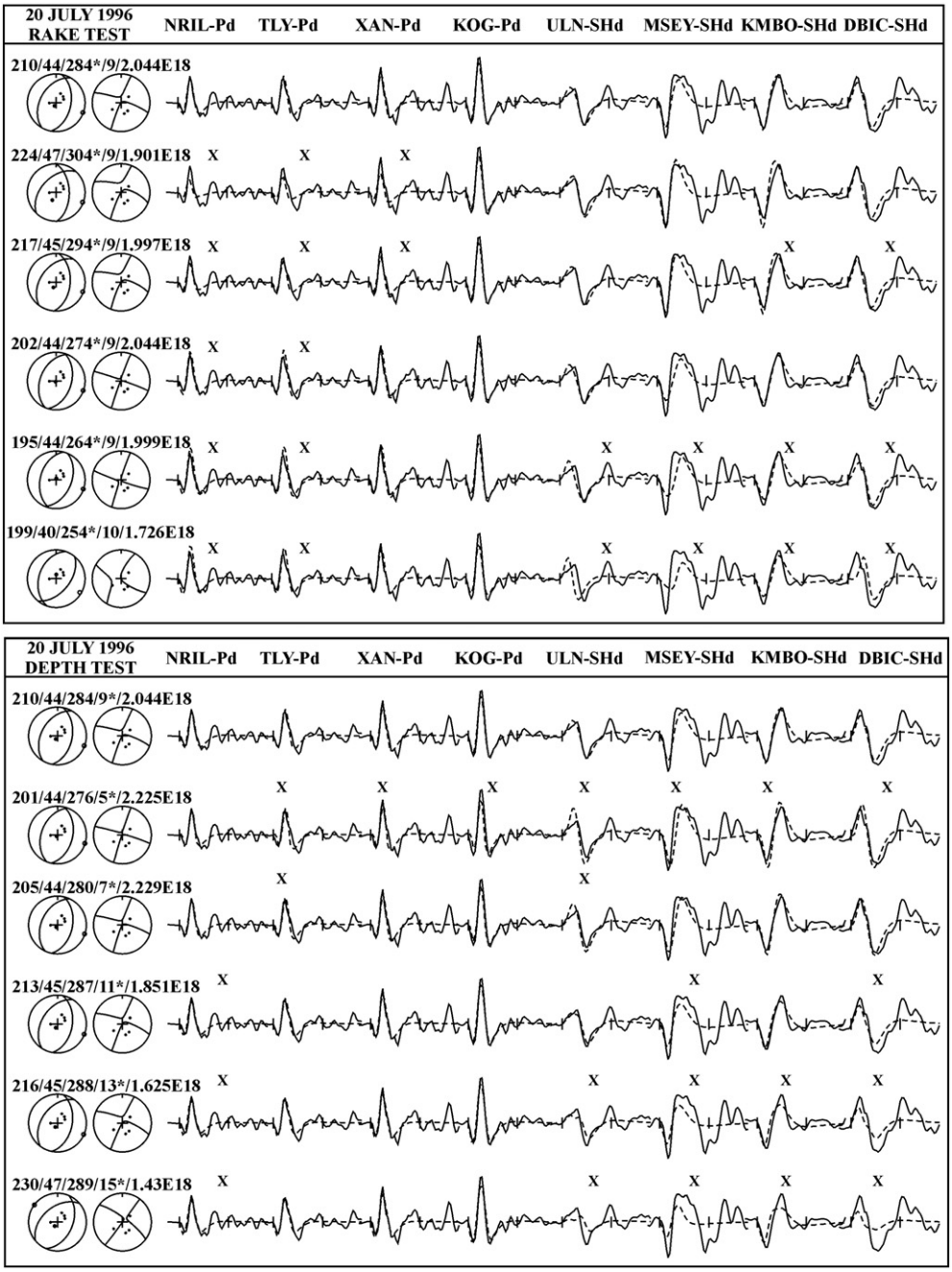

Figure A2. An example of uncertainty tests for rake angle and focal depth of the July 20, 1996 Dodecanese earthquake. Fixed rake angle and focal depth are marked by *. Header information is as in Fig. A1.

Their results showed the effects of bathymetric features of the Nile Delta, and hence they suggested that the Nile Delta acts as a natural barrier to slow down tsunami waves at shallower depths (<500 m) as a result of interferences of refractions and diffractions of sea waves. According to the numerical simulation, tsunami waves propagated towards SW direction. Most destructive waves were calculated near the Cyprus Island. Maximum positive tsunami amplitudes were found to be about 2.5 m along the northern coastal plains of the Eastern Mediterranean Sea. At the southern coastal plains, the more destruction observed at Alexandria–Egypt coasts with ~1 m maximum tsunami wave amplitudes (Fig. A8).

The August 13, 1822 earthquake—Syria

This earthquake is known as the largest event along the Dead Sea Fault Zone in historical past (Fig. 12; Table 4). Historical documents reported that it was felt from the Black Sea to Gaza, and it was followed by an aftershock sequence that lasted almost 2.5 years. It destroyed the regions between Gaziantep and Antakya in Turkey and Aleppo and Khan Sheikhun in NW Syria (Sbeinati et al., 2005). In addition, Poirier and Taher (1980) suggested that this event (I_o: X–XI) destroyed 60% of Aleppo and generated sea waves in İskenderun Gulf. Plassard and Kogoj (1981) demonstrated intensity (I_o) ~ V in Lebanon, and destruction in Antakya, Aleppo and Lattakia with tsunami waves. In this study, we assumed a magnitude of M ~ 7.0–7.5 and normal faulting mechanism with a small amount of strike slip component for the 1822 Syria earthquake by using active tectonic structures, earthquake source parameters and geological knowledge of the region. Related parameters and a representative fault mechanism solution are shown in Fig. 12 and Table 4. Initial tsunami wave was calculated to be 2.053 m

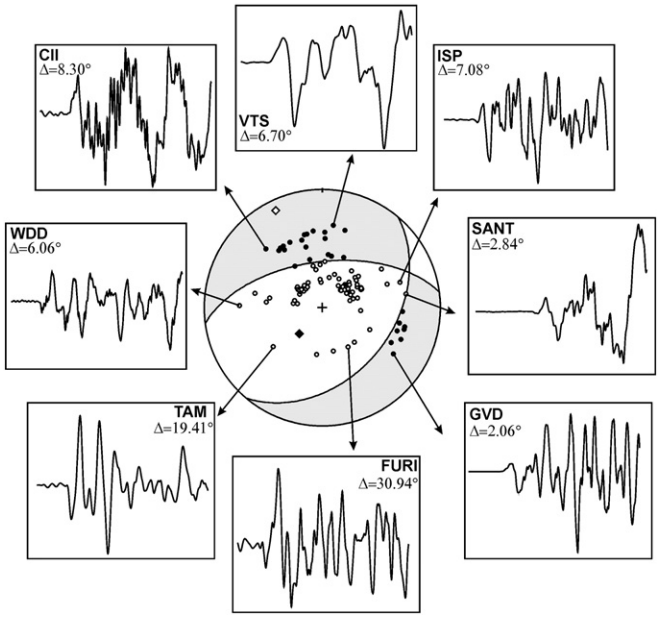

Figure A3. Distribution of P-Wave first motion polarities of the May 24, 2000 earthquake recorded by seismic stations at teleseismic and regional distances. Lower hemisphere equal area projections are used. The station positions have been plotted with the same velocity model beneath the source used in our minimum misfit solution. Both nodal planes are those of the minimum misfit solution. Station names and epicentral distances are given near example waveforms. Filled circles are compressional first motions, opens are dilatational.

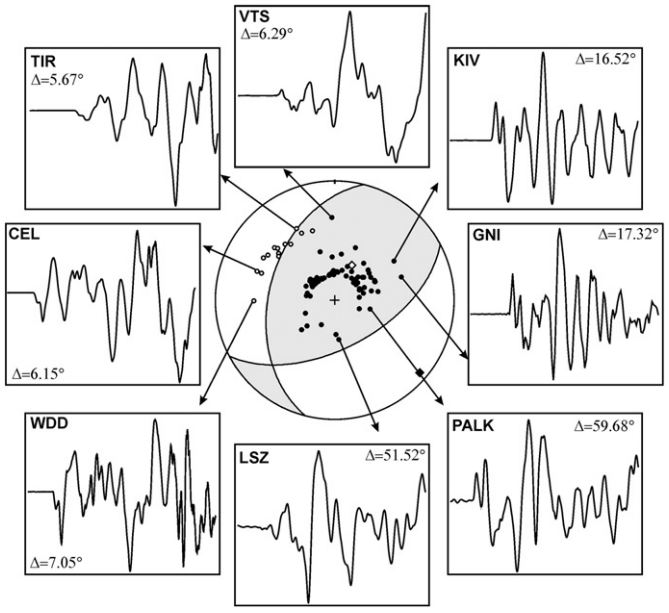

Figure A5. Distribution of P-Wave first motion polarities of the January 08, 2006 earthquake recorded by seismic stations at teleseismic and regional distances. Header information is as in Fig. A3.

which obtained by the summation of trough (0.806 m) and crest (−1.247 m) amplitudes. According to numerical simulation results (Fig. A9), tsunami waves in the Iskenderun Gulf propagated towards the eastern part of Cyprus where destructive tsunami waves were observed. Maximum positive tsunami amplitudes were calculated as about 3 m along Antakya coasts and ~2.5 m along Adana coasts. We also obtained ~1.75 m wave heights along the Lattakia (Cyprus) and Syria coastal plains. However, the other Eastern Mediterranean coastal plains such as SW Anatolia, the Nile Delta and African coastal plains were not affected too much from tsunami waves since the wave energy did not propagate as far away and dissipated due to natural bathymetrical barriers such as the Cyprus Island (Fig. A9).

Appendix B. Supplementary data

Supplementary data to this article can be found online at doi:10.1016/j.tecto.2012.02.019.

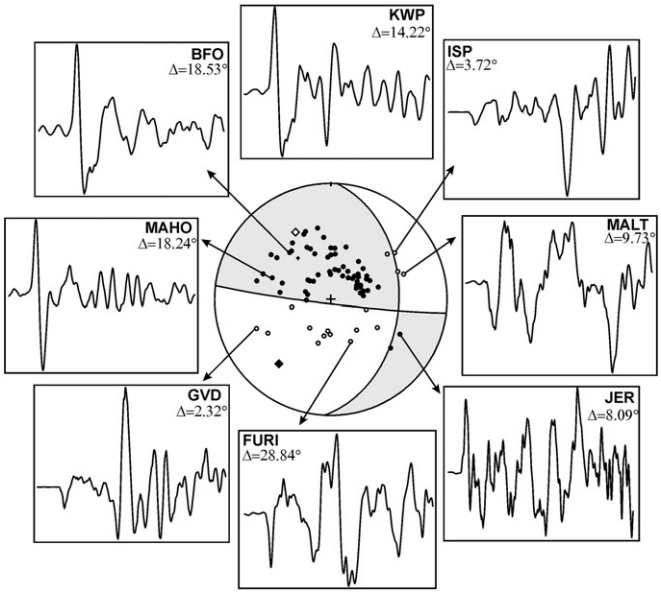

Figure A4. Distribution of P-Wave first motion polarities of the January 22, 2002 earthquake recorded by seismic stations at teleseismic and regional distances. Header information is as in Fig. A3.

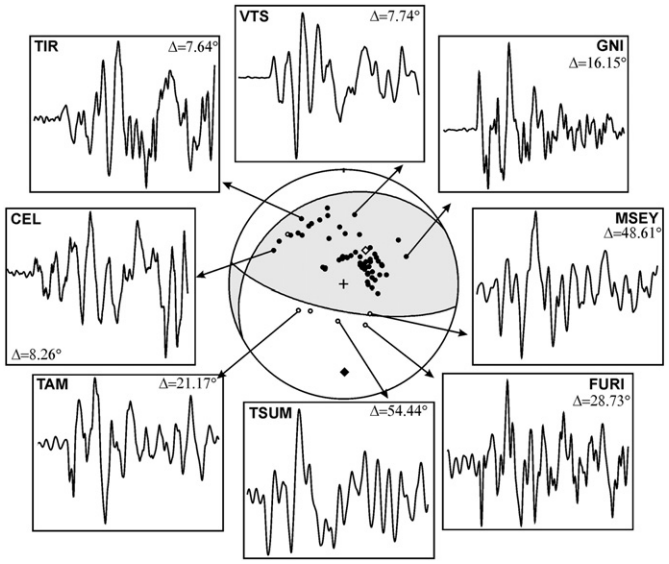

Figure A6. Distribution of P-Wave first motion polarities of the March 28, 2008 earthquake recorded by seismic stations at teleseismic and regional distances. Header information is as in Fig. A3.

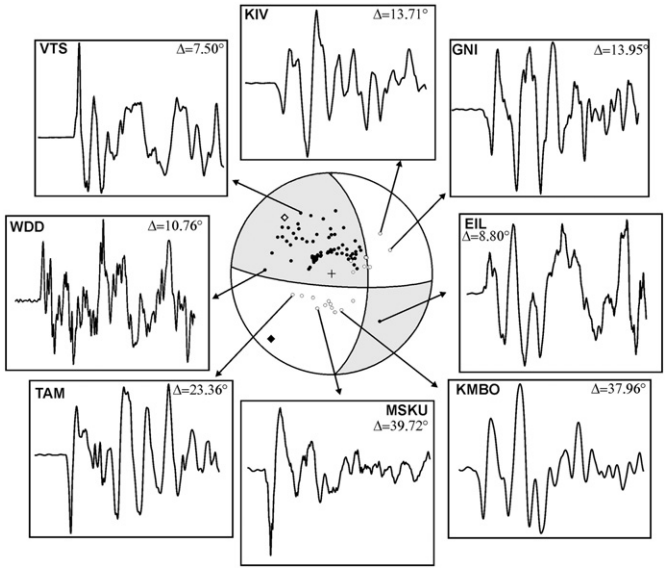

Figure A7. Distribution of P-Wave first motion polarities of the July 15, 2008 earthquake recorded by seismic stations at teleseismic and regional distances. Header information is as in Fig. A3.

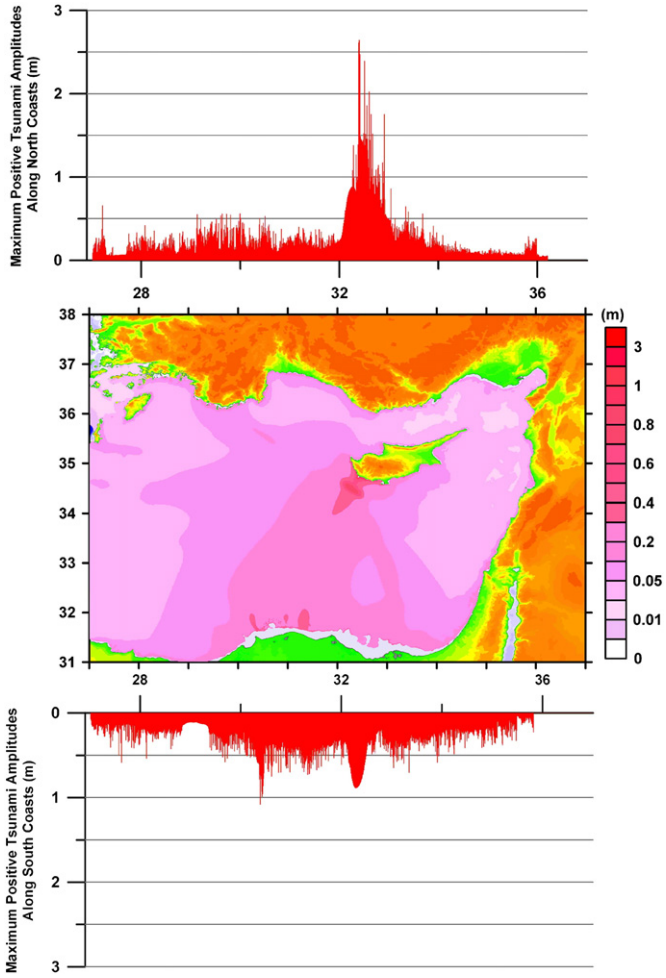

Figure A8. Distribution of maximum positive tsunami wave amplitudes along the north and south coasts of the Eastern Mediterranean and directivity of tsunami wave propagation during the tsunamigenic May 11, 1222 Cyprus earthquake.

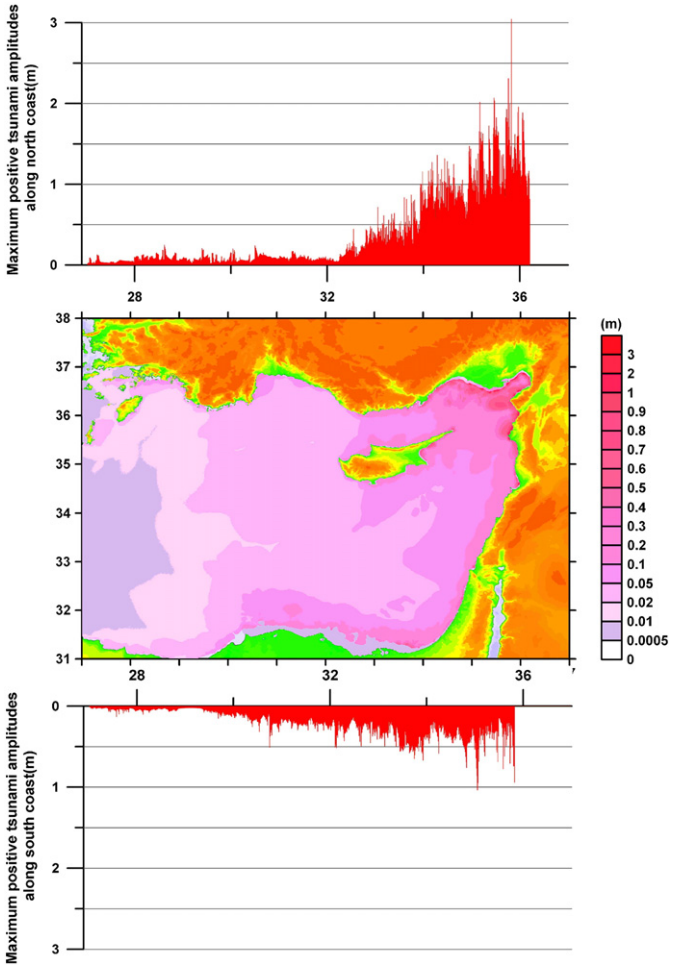

Figure A9. Distribution of maximum positive tsunami wave amplitudes along the north and south coasts of the Eastern Mediterranean and directivity of tsunami wave propagation during the tsunamigenic August 13, 1822 Syria earthquake.

References

Aki, K., 1972. Earthquake mechanism. Tectonophysics 13, 423–446.

Aksu, A.E., Hall, J., Yaltırak, C., 2008. Miocene-Recent evolution of Anaximander Mountain and Finike Basin at the junction of Hellenic and Cyprus Arcs, Eastern Mediterranean. Marine Geology. doi:10.1016/j.margeo.2008.04.008.

Altınok, Y., Ersoy, Ş., 2000. Tsunamis observed on and near the Turkish coast. Natural Hazards 21, 185–205.

Ambraseys, N.N., 1962. Data for the investigation of the seismic sea waves in the Eastern Mediterranean. Bulletin of the Seismological Society of America 52, 895–913.

Ambraseys, N.N., 2009. Earthquakes in the Mediterranean and Middle East: A Multidisciplinary Study of Seismicity up to 1900. Cambridge University Press, ISBN-13: 9780521872928, 968 pages, Cambridge, U.K.

Ambraseys, N.N., Melville, C.P., Adam, R.D., 1994. The Seismicity of Egypt, Arabia and the Red Sea: A Historical Review. Cambridge University Press, Cambridge, UK.

Ambraseys, N.N., Synolakis, C., 2010. Tsunami Catalogs for the Eastern Mediterranean, Revisited. Journal of Earthquake Engineering 14 (3), 309–330.

Antonopoulos, J., 1980. Data from investigation on seismic sea-waves events in the Eastern Mediterranean from the birth of Christ to 1980 AD (6 parts). Annali di Geofisica 33, 141–248.

Bécel, A., Laigle, M., de Voogd, B., Hirn, A., Taymaz, T., Galve, A., Shimamura, H., Murai, Y., Lépine, J.-C., Sapin, M., Özalaybey, S., 2009. Moho, crustal architecture and deep deformation under the North Marmara Trough, from the SEISMARMARA Leg 1 offshore-onshore reflection-refraction survey. Tectonophysics 467 (1–4), 1–21. doi:10.1016/j.tecto.2008.10.022.

Bécel, A., Laigle, M., de Voogd, B., Hirn, A., Taymaz, T., Yolsal-Cevikbilen, S., Shimamura, H., 2010. North Marmara Trough architecture of basin infill, basement and faults, from PSDM reflection and OBS refraction seismics. Tectonophysics 490, 1–14.

Ben Menahem, A., 1979. Earthquake catalogue for the Middle East (92 B.C. to 1980 A.D.). Bollettino di Geofisica Teorica ed Applicata 21, 245–313.

Benetatos, C., Kiratzi, A., Papazachos, C., Karakaisis, G., 2004. Focal mechanisms of shallow and intermediate depth earthquakes along the Hellenic Arc. Journal of Geodynamics 37, 253–296.

Bijwaard, H., Spakman, W., 1998. Closing the gap regional and global travel time tomography. Journal of Geophysical Research 103, 30055–30078.
Bilek, S.L., 2009. Seismicity along the South American subduction zone: review of large earthquakes, tsunamis, and subduction zone complexity. Tectonophysics. doi:10.1016/j.tecto.2009.02.037.
Bilham, R., 2008. Tsunamigenic Middle Earth. Nature Geoscience 1, 211–212.
Biryol, C.B., Beck, S.L., Zandt, G., Özacar, A.A., 2011. Segmented African lithosphere beneath the Anatolian region inferred from teleseismic P-wave tomography. Geophysical Journal International 184 (3), 1037–1057.
Bohnhoff, M., Makris, J., Papanikolaou, D., Stavrakakis, G., 2001. Crustal investigation of the Hellenic subduction zone using wide aperture seismic data. Tectonophysics 343, 239–262.
Bohnhoff, M., Harjes, H.-P., Meier, T., 2005. Deformation and stress regimes in the Hellenic subduction zone from focal mechanisms. Journal of Seismology 9, 341–366.
Bryant, E.A., 1991. Natural Hazards. Cambridge University Press, UK, pp. 58–85.
Calvi, V.S., 1941. Erdbebenkatalog der Türkei und Einiger Benaehbarter Gebiete, Report No. 276. MTA Institute, Ankara, Turkey.
Cocard, M., Kahle, H.-G., Peter, Y., Geiger, A., Veis, G., Felekis, S., Paradissis, D., Billiris, H., 1999. New constrains on the rapid crustal motion of the Aegean region: recent results inferred from GPS measurements (1993–1998) across the West Hellenic Arc, Greece. Earth and Planetary Science Letters 172, 39–47.
Coronelli, P., Parisotti, V., 1688. Isola di Rodi geografica, storica, antica e moderna. Venice.
Endrun, B., Meier, T., Bischoff, M., Harjes, H.-P., 2004. Lithospheric structure in the area of Crete constrained by receiver functions and dispersion analysis Rayleigh phase velocities. Geophysical Journal International 110, 347–360.
Fischer, K.D., Babeyko, A., 2007. Modelling the 365 AD Crete earthquake and its tsunami. Geophysical Research Abstracts, Vol. 9. European Geosciences Union 2007, Vienna, Austria.
Fokaefs, A., Papadopoulos, G.A., 2006. Tsunami hazard in the Eastern Mediterranean: strong earthquakes and tsunamis in Cyprus and the Levantine Sea. Natural Hazard. doi:.
Fukahata, Y., Yagi, Y., Matsu'ura, M., 2003. Waveform inversion for seismic source processes using ABIC with two sorts of prior constraints: comparison between proper and improper formulations. Geophysical Research Letters 30. doi:10.1029/2002GL016293.
Futterman, W., 1962. Dispersive body waves. Journal of Geophysical Research 67, 5279–5291.
Galanopoulos, A.G., 1960. Tsunamis observed on the coasts of Greece from antiquity to present time. Annali di Geofisica 13, 369–386.
Ganas, A., Parsons, T., 2009. Three-dimensional model of Hellenic Arc deformation and origin of the Cretan uplift. Journal of Geophysical Research 114, B06404. doi:10.1029/2008JB005599.
GEBCO-BODC, 1997. General Bathymetric Chart of the Oceans, Digital Version. Distributed on CD-ROM by the British Oceanographic Data Centre, Birkenhead.
Geist, E.L., 2005. Rapid tsunami models and earthquake source parameters: far-field and local applications. ISET Journal of Earthquake Technology Paper No. 460, 42 (4), pp. 127–136.
Gica, E., Teng, M.H., Asce, M., Liu, P.L.-F., Asce, F., Titov, V.V., Zhou, H., 2007. Sensitivity analysis of source parameters for earthquake generated distant tsunamis. Journal of Waterways, Port, Coasts and Ocean Engineering 133 (6), 429–441.
Goldstein, P., Snoke, A., 2005. SAC Availability for the IRIS Community. Incorporated Institutions for Seismology Data Management Center Electronic Newsletter.
Goldstein, P., Dodge, D., Firpo, M., Minner, L., 2003. SAC2000: signal processing and analysis tools for seismologists and engineers. In: Lee, W.H.K., Kanamori, H., Jennings, P.C., Kisslinger, C. (Eds.), Invited contribution to "The IASPEI International Handbook of Earthquake and Engineering Seismology. Academic Press, London.
Goto, C., Ogawa, Y., Shuto, N., Imamura, F., 1997. Numerical method of tsunami simulation with the leap-frog scheme (IUGG/IOC Time Project). IOC Manual, 35. UNESCO.
Gudmundsson, O., Sambridge, M., 1998. A regionalized upper mantle (RUM) seismic model. Journal of Geophysical Research 103, 7121–7136.
Guidoboni, E., Ebel, J.E., 2009. Earthquakes and Tsunamis in the Past: A Guide to Techniques in Historical Seismology. Cambridge University Press, ISBN-13: 9780521837958, 602 pages, Cambridge, UK.
Guidoboni, E., Comastri, A., 1997. The large earthquake of 8 August 1303 in Crete: seismic scenario and tsunami in the Mediterranean area. Journal of Seismology 1, 55–72.
Guidoboni, E., Comastri, A., 2005a. Catalogue of Earthquakes and Tsunamis in the Mediterranean area from the 11th to the 15th Century. INGV-SGA, Bologna, p. 1037.
Guidoboni, E., Comastri, A., 2005b. Two thousand years of earthquakes and tsunamis in the Aegean area (from 5th BC to 15th century). International Symposium on the Geodynamics of Eastern Mediterranean: Active Tectonics of the Aegean Region, Abstract Book, p. 242. Kadir Has University, 15–18 June, 2005, İstanbul, Turkey.
Hall, J., Aksu, A.E., Yaltırak, C., Winsor, J.D., 2008. Structural architecture of the Rhodes Basin: a deep depocentre that evolved since the Pliocene at the junction of Hellenic and Cyprus Arcs, Eastern Mediterranean. Marine Geology. doi:10.1016/ j.margeo.2008.02.007.
Hartzell, S.H., Heaton, T.H., 1983. Inversion of strong ground motion and teleseismic waveform data for the fault rupture history of the 1979 Imperial Valley, California earthquake. Bulletin of the Seismological Society of America 73, 1553–1583.
Hatzfeld, D., Besnard, M., Makropoulos, K., Hatzidimitriou, P., 1993. Microearthquake seismicity and fault plane solutions in the southern Aegean and its geodynamic implications. Geophysical Journal International 115, 799–818.
Imamura, F., 1995. Tsunami numerical simulation with the staggered leap-frog scheme (Numerical Code of TUNAMI-N1). School of Civil Engineering, Aslan Inst. Tech. and Disaster Control Research Center, Tohoku University.
Imamura, F., 1996. Review of tsunami simulation with a finite difference method. In: Yeh, H., Liu, P., Synolakis, C. (Eds.), Long-Wave Runup Models. World Sci., New York, pp. 25–42.
Jackson, J., Priestley, K., Allen, M., Berberian, M., 2002. Active tectonics of the Alpine–Himalayan Belt between western Turkey and Pakistan. Geophysical Journal of the Royal Astronomical Society 77, 185–264.
Jeffreys, S.H., Bullen, K.E., 1940. Seismological Tables. British Assoc. Advancement Sci., Gray – Milne Trust, London.
Kanamori, H., 1977. The energy release in great earthquakes. Journal of Geophysical Research 82, 2921–2987.
Kanamori, H., 1994. Mechanics of earthquakes. Annual Review of Earth and Planetary Sciences 22, 207–237.
Kanamori, H., Anderson, D.L., 1975. Theoretical basis of some empirical relations in seismology. Bulletin of the Seismological Society of America 65 (5), 1073–1095.
Karagianni, E.E., Papazachos, C.B., Panagiotopoulos, D.G., Suhadolc, P., Vuan, A., Panza, G.F., 2005. Shear velocity structure in the Aegean area obtained by inversion of Rayleigh waves. Geophysical Journal International 160, 127–143.
Karakostas, C., Makarios, T., Lekidis, V., Salonikios, T., Sous, T., Makra, T., Anastasiadis, A., Klimism, N., Dimitriou, P., Margaris, B., Papaioannou, C., Theodulidis, N., 2006. The Kythera (Greece) earthquake of January 8, 2006: preliminary report on strong motion data, geotechnical and structural damage. Earthq. Eng. Res. Inst. 21 pp.
Keilis-Borok, V.I., 1959. On the estimation of the displacement in an earthquake source and source of dimensions. Annali di Geofisica 12, 205–214.
Kikuchi, M., Kanamori, H., 1991. Inversion of complex body waves—III. Bulletin of the Seismological Society of America 81, 2335–2350.
Kiratzi, A., Louvari, E., 2003. Focal mechanisms of shallow earthquakes in the Aegean Sea and surrounding lands determined by waveform modeling: a new database. Journal of Geodynamics 36, 251–274.
Kiratzi, A., Papazachos, C., 1995. Active deformation of the shallow part of the subducting lithospheric slab in the southern Aegean. Journal of Geodynamics 19, 65–78.
Konstantinou, I.K., Kalogeras, I.S., Melis, N.S., Kourouzidis, M.C., Stavrakakis, G.N., 2006. The 8 January 2006 earthquake (M_w 6.7) offshore Kythira Island, southern Greece: seismological, strong motion, and macroseismic observations of an intermediate-depth event. Seismological Research Letters 77, 544–553.
Laigle, M., Sachpazi, M., Hirn, A., 2004. Variation of seismic coupling with slab detachment and upper plate structure along the western Hellenic subduction zone. Tectonophysics 391 (1–4), 85–95.
Laigle, M., Becel, A., do Voogd, B., Hirn, A., Taymaz, T., Özalaybey, S., members of SEISMARMARA Leg1 Team, 2008. A first deep seismic survey in the Sea of Marmara: Deep basins and whole crust architecture and evolution. Earth and Planetary Science Letters 270 (3–4), 168–179. doi:10.1016/j.epsl.2008.02.031.
Le Pichon, X., Angelier, J., 1981. The Aegean Sea. Philosophical Transactions of the Royal Society of London, Series A 300, 357–372.
Le Pichon, X., Chamot-Rooke, N., Lallemant, S., Noomen, R., Veis, G., 1995. Geodetic determination of the kinematics of central Greece with respect to Europe. Journal of Geophysical Research 100, 12,675–12,690.
Lorito, S., Tiberti, M.M., Basili, R., Piatanesi, A., Valensise, G., 2008. Earthquake-generated tsunamis in the Mediterranean Sea: scenarios of potential threats to Southern Italy. Journal of Geophysical Research 113, B01301. doi:10.1029/2007/JB004943.
Louvari, E., 2000. A detailed seismotectonic analysis of the Aegean and the surrounding area, PhD Thesis, Aristotle University of Thessaloniki, 374 pp.
Lyon-Caen, H., Armijo, R., Drakopoulos, J., Baskoutass, J., Delibassis, N., Gaulon, R., Kouskouna, V., Latoussakis, J., Makropoulos, K., Papadimitriou, P., Papanastassiou, D., Pedotti, G., 1988. The 1986 Kalamata (south-Peloponnesus) earthquake-detailed study of a normal-fault, evidences for east–west extension in the Hellenic arc. Journal of Geophysical Research 93, 14967–15000.
Maggi, A., Jackson, J., Priestley, K., Baker, C., 2000. A re-assessment of focal distributions in southern Iran, the Tien Shan and northern India: do earthquakes really occur in the continental mantle? Geophysical Journal International 143, 629–661.
Mai, P.M., Beroza, G.C., 2000. Source scaling properties from finite-fault-rupture models. Bulletin of the Seismological Society of America 90, 604–615.
Makris, J., Stobbe, C., 1984. Physical properties and state of the crust and upper mantle of the Eastern Mediterranean sea deduced from geophysical data. Marine Geology 55, 347–363.
Makris, J., Ben-Avraham, Z., Behle, A., Ginzburg, A., Giese, P., Steinmetz, L., Whitmarsh, R.B., Eleftheriou, S., 1983. Seismic refraction profiles between Cyprus and Israel and their interpretation. Geophysical Journal of the Royal Astronomical Society 75, 575–591.
Mansinha, L., Smylie, D.E., 1971. The displacement fields of inclined faults. Bulletin of the Seismological Society of America 61, 1433–1440.
Mascle, J., Martin, L., 1990. Shallow structure and recent evolution of the Aegean Sea: a synthesis based on continuous reflection profiles. Marine Geology 94, 271–299.
Mascle, J., Le Cleac'h, A., Jongsma, D., 1986. The eastern Hellenic margin from Crete to Rhodes: example of progressive collision. Marine Geology 73, 145–168.
McCaffrey, R., Abers, G., 1988. SYN3: a program for inversion of teleseismic body waveforms on microcomputers. Technical Report AFGL-TR-88-0099. Air Force Geophysics Laboratory, Hanscomb Air Force Base, MA., USA.
McCaffrey, R., Zwick, P., Abers, G., 1991. SYN4 Program. IASPEI Software Library, 3, pp. 81–166.
McClusky, S., Balassanian, S., Barka, A., Demir, C., Ergintav, S., Georgiev, I., Gürkan, O., Hamburger, M., Hurst, K., Kahle, H., Kastens, K., Kekelidze, G., King, R., Kotzev, V., Lenk, O., Mahmoud, S., Mishin, A., Nadariya, M., Ouzounis, A., Paradissis, D., Peter, Y., Prilepin, M., Reilinger, R., Şanlı, I., Seeger, H., Tealeb, A., Toksöz, M.N., Veis, G., 2000. Global positioning system constraints on plate kinematics and dynamics in the Eastern Mediterranean and Caucasus. Journal of Geophysical Research 105, 5695–5719.

McClusky, S., Reilinger, R., Mahmoud, S., Ben Sari, D., Tealeb, A., 2003. GPS constraints on Africa (Nubia) and Arabia plate motion. Geophysical Journal International 155, 126–138.
McKenzie, D.P., 1972. Active tectonics of the Mediterranean region. Geophysical Journal of the Royal Astronomical Society 30, 109–185.
McKenzie, D.P., 1978. Active tectonics of the Alpine-Himalayan Belt: the Aegean Sea and its surrounding regions. Geophysical Journal of the Royal Astronomical Society 55, 217–254.
Molnar, P., Lyon-Cáen, H., 1989. Fault plane solutions of earthquakes and active tectonics of the Tibetan Plateau and its margins. Geophysical Journal International 99, 123–153.
Nàbělek, J., 1984. Determination of earthquake source parameters from inversion of body waves. PhD Thesis M.I.T., Massachusetts, USA.
Nelson, M.R., McCaffrey, R., Molnar, P., 1987. Source parameters for 11 earthquakes in the Tien Shan, Central Asia, determined by P and SH waveform inversion. Journal of Geophysical Research 92, 12629–12648.
Nyst, M., Thatcher, W., 2004. New constraints on the active tectonic deformation of the Aegean. Journal of Geophysical Research 109. doi:10.1029/2003jb002830.
Okada, Y., 1985. Surface deformation due to shear and tensile faults in a half-space. Bulletin of the Seismological Society of America 75, 1135–1154.
Okal, E.A., Synolakis, C.E., Uslu, B., Kalligeris, N., Voukouvalas, E., 2009. The 1956 earthquake and tsunami in Amorgos, Greece. Geophysical Journal International 178, 1533–1554.
Papadopoulos, G.A., 2001. Tsunamis in the East Mediterranean: a catalogue for the area of Greece and adjacent seas. Proc Joint IOC-IUGG Int. Workshop, Tsunami Risk Assessment beyond 2000: Theory, Practice and Plans, Moscow, Russia.
Papadopoulos, G.A., Fokaefs, A., 2005. Strong tsunamis in the Eastern Mediterranean Sea: a re-evaluation. ISET Journal of Earthquake Technology Paper No. 463. Vol. 42, No.4, pp. 159–170.
Papadopoulos, G.A., Imamura, F., Minoura, K., Takahasi, T., Kuran, U., Yalçıner, A.C., 2004. Strong earthquakes and tsunamis in the East Hellenic Arc. European Geosciences Union, Geophysical Research Abstracts, 6, p. 03212.
Papadopoulos, G.A., Daskalaki, E., Fokaefs, A., Giraleas, N., 2007. Tsunami hazard in the Eastern Mediterranean: strong earthquakes and tsunamis in the east Hellenic Arc and Trench system. Natural Hazards and Earth System Sciences 7, 57–64.
Papazachos, B.C., 1996. Large seismic faults in the Hellenic arc. Annals of Geophysics 39, 892–903.
Papazachos, B.C., Kiratzi, A., 1996. A detailed study of the active crustal deformation in the Aegean and surrounding area. Tectonophysics 253, 129–153.
Papazachos, B.C., Papaioannou, C.A., Papazachos, C.B., Savvaidis, A.S., 1999. Rupture zones in the Aegean region. Tectonophysics 308, 205–221.
Papazachos, B.C., Karakostas, V.G., Papazachos, C.B., Scordilis, E.M., 2000. The geometry of the Wadati–Benioff Zone and lithospheric kinematics in the Hellenic arc. Tectonophysics 319, 275–300.
Parke, G., 2001. Active tectonic and sedimentary processes in western Turkey. PhD Thesis, University of Cambridge.
Pelinovsky, E.N., 1996. Hydrodynamics of tsunami waves. Institute of Applied Physics, Nizhny Novgorod.
Pirazzoli, P.A., Ausseil – Badie, J., Giresse, P., Hadjidaki, E., Arnold, M., 1992. Historical environmental changes at Phalasarna Harbour, west Crete. Geoarchaeology 7 (4), 371–392.
Pirazzoli, P.A., Thommeret, J., Thommeret, Y., Laborel, J., Montaggioni, L.F., 1982. Crustal block movements from Holocene shorelines: Crete and Antikythira (Greece). Tectonophysics 86, 27–83.
Plassard, J., Kogoj, B., 1981. Seismicité du Liban: catalogue des seismes ressentis, 3rd ed. Annales-Mémoires de l'Observatoire de Ksara, IV. CNRS, Beyrouth, p. 67.
Poirier, J.P., Taher, M.A., 1980. Historical seismicity in the near and Middle East, North Africa, and Spain from Arabic documents (VII–XVIIIth century). Bulletin of the Seismological Society of America 70, 2185–2201.
Reilinger, R., McClusky, S., Vernant, P., Lawrence, S., Ergintav, S., Cakmak, R., Ozener, H., Kadirov, F., Guliev, I., Stepanyan, R., Nadariya, M., Hahubia, M., Mahmoud, S., Sakr, K., ArRajehi, A., Paradissis, D., Al- Aydrus, A., Prilepin, M., Guseva, T., Evren, E., Dmitrotsa, A., Filikov, S.V., Gomez, F., Al-Ghazzi, R., Karam, G., 2006. GPS constraints on continental deformation in the Africa-Arabia-Eurasia continental collisional zone and implications for the dynamics of plate interactions. Journal of Geophysical Research 111, B05411. doi:10.1029/2005JB004051.
Reilinger, R., McClusky, S., Paradissis, D., Ergintav, S., Vernant, P., 2010. Geodetic constraints on the tectonic evolution of the Aegean region and strain accumulation along the Hellenic subduction zone. Tectonophysics 488, 22–30.
Roumelioti, Z., Kiratzi, A., Benetatos, C., 2011. Time-domain moment tensors for shallow ($h \leq 40$ km) earthquakes in the broader Aegean Sea for the years 2006 and 2007: the database of the Aristotle University of Thessaloniki. Journal of Geodynamics 51, 179–189.
Şaroğlu, F., Emre, Ö., Kuşçu, İ., 1992. Active Fault Map of Turkey, 2 sheets. MTA, Ankara.
Sbeinati, M.R., Darawcheh, R., Mouty, M., 2005. The historical earthquakes of Syria: an analysis of large and moderate earthquakes from 1365 B.C. to 1900 A.D. Annales of Geophysics 48 (3), 347–435.
Shaw, B., Jackson, J., 2010. Earthquake mechanisms and active tectonics of the Hellenic subduction zone. Geophysical Journal International 181, 966–984.
Shaw, B., Ambraseys, N.N., England, P.C., Floyd, M.A., Gorman, G.J., Higham, T.F.G., Jackson, J.A., Nocquet, J.M., Pain, C.C., Piggott, M.D., 2008. Eastern Mediterranean tectonics and tsunami hazard inferred from the AD 365 earthquake. Nature Geoscience 1, 265–276.
Shuto, N., Goto, G., Imamura, F., 1990. Numerical simulation as a means of warning for near field tsunami. Coastal Engineering in Japan 33, 173–193.
Skarlatoudis, A.A., Papazachos, C.B., Margaris, B.N., Papaioannou, Ch., Ventouzi, Ch., Vamvakaris, D., Bruestle, A., Meier, T., Friederich, W., Stavrakakis, G., Taymaz, T., Kind, R., Vafidis, A., Dahm, T., 2009. Source combination of acceleration-sensor and broadband velocity-sensor recordings for attenuation studies: the case of the 8 January 2006 Kythera intermediate-depth earthquake. Bulletin of the Seismological Society of America 99 (2A), 694–704.
Smith, W.H.F., Sandwell, D.T., 1997a. Measured and estimated seafloor topography (version 4.2). World Data Centre-A for Marine Geology and Geophysics research publication RP-1, poster, 34" x 53".
Smith, W.H.F., Sandwell, D.T., 1997b. Global seafloor topography from satellite altimetry and ship depth soundings. Science 277, 1957–1962.
Soloviev, S.L., Solovieva, O.N., Go, C.N., Kim, K.S., Shchetnikov, N.A., 2000. Tsunamis in the Mediterranean Sea 2000 B.C.–2000 A.D. Advances in Natural and Technological Hazards Research, 13. Kluwer, Dordrecht.
Spakman, W., Wortel, M.J.R., Vlaar, N.J., 1988. The Hellenic subduction zone: a tomographic image and its geodynarnic implications. Geophysical Research Letters 15, 60–63.
Stiros, S.C., 2001. The AD 365 Crete earthquake and possible seismic clustering during the fourth to sixth centuries AD in the Eastern Mediterranean: a review of historical and archaeological data. Journal of Structural Geology 23, 545–562.
Stiros, S.C., 2010. The 8.5+ magnitude, AD365 earthquake in Crete: coastal uplift, topography changes, archaeological and historical signature. Quaternary International 216, 54–63.
Stiros, S.C., Drakos, A., 2006. A fault-model for the tsunami-associated, magnitude $\geq$ 8.5 Eastern Mediterranean, AD 365 earthquake. Zeitschrift für Geomorphologie 146, 125–137.
Tan, O., Taymaz, T., 2006. Active tectonics of the Caucasus: earthquake source mechanisms and rupture histories obtained from inversion of teleseismic body waveforms. Post-collisional Tectonics and Magmatism in the Mediterranean Region and Asia: Geol. Soc. of America, Special Paper, 409, pp. 531–578. doi:10.1130/2006.2409 (25).
Taymaz, T., 1990. Earthquake source parameters in the Eastern Mediterranean Region. PhD Thesis, Darwin College, University of Cambridge, U.K.
Taymaz, T., 1996. S–P wave travel-time residuals from earthquakes and lateral inhomogeneity in the upper mantle beneath the Aegean and the Hellenic trench near Crete. Geophysical Journal International 127, 545–558.
Taymaz, T., Jackson, J., Westaway, R., 1990. Earthquake mechanisms in the Hellenic Trench near Crete. Geophysical Journal International 102, 695–731.
Taymaz, T., Jackson, J.A., McKenzie, D., 1991. Active tectonics of the north and central Aegean Sea. Geophysical Journal International 106, 433–490.
Taymaz, T., Westaway, R., Reilinger, R., 2004. Active faulting and crustal deformation in the Eastern Mediterranean Region. Tectonophysics 391, 1–9. doi:10.1016/j.tecto.2004.07.005.
Taymaz, T., Wright, T.J., Yolsal, S., Tan, O., Fielding, E., Seyitoğlu, G., 2007a. Source characteristics of the 6 June 2000 Orta–Çankırı (central Turkey) earthquake: a synthesis of seismological, geological and geodetic (InSAR) observations, and internal deformation of the Anatolian plate. The Geodynamics of the Aegean and Anatolia: Geological Society, London, Special Publication, 291, pp. 259–290.
Taymaz, T., Yılmaz, Y., Dilek, Y., 2007b. The geodynamics of the Aegean and Anatolia: introduction. Geological Society, London, Special Publications 291, 1–16.
Taymaz, T., Yolsal, S., Tok, H.E., et al., 2007c. Source rupture processes of M_w~6.7 Kytheria Earthquake of January 8, 2006 and Synthesis of International EGELADOS and COLUMBOS Projects: active tectonics of the Aegean Sea. Geophysical Research Abstracts, 9. Vienna, Austria.
Vassilakis, E., Royden, L., Papanikolaou, D., 2011. Kinematic links between subduction along the Hellenic trench and extension in the Gulf of Corinth, Greece: a multidisciplinary analysis. Earth and Planetary Science Letters 303, 108–120.
Ventouzi, Ch., Bruestle, A., Fischer, K.D., Kueperkoch, L., Taymaz, T., Meier, T., Friederich, W., Papazachos, C., Stavrakakis, G., the EGELADOS working group, 2007. Investigations on the Kythira-earthquake (SW Aegean Sea) on 8 January 2006 using the EGELADOS-network, European Geosciences Union (EGU) 2007. Geophysical Research Abstracts, 9, p. 07086. Vienna, Austria.
Wells, D.L., Coppersmith, K.J., 1994. New empirical relationships among magnitude, rupture length, rupture width, rupture area, and surface displacement. Bulletin of the Seismological Society of America 84, 974–1002.
Wessel, P., Smith, W.H.F., 1998. New, improved version of the Generic Mapping Tools released. EOS, Transactions of the American Geophysical Union 79, 579.
Woodside, J., Mascle, J., Huguen, C., Volkonskala, A., 2000. The Rhodes Basin, a Post-Miocene tectonic trough. Marine Geology 165, 1–12.
Woodside, J.M., Mascle, J., Zitter, T.A.C., Limonov, A.F., Ergun, M., Volkonskaia, A., a shipboard scientists of the PRISMED II expedition, 2002. The Florence Rise, the western bend of the Cyprus Arc. Marine Geology 185, 177–194.
Wortel, M.J.R., Spakman, W., 1992. Structure and dynamics of subducted lithosphere in the Mediterranean region. Proceedings of the Koninklijke Nederlandse Akademie van Wetenschappen 95 (3), 325–347.
Yagi, Y., Fukahata, Y., 2011. Introduction of uncertainty of Green's function into waveform inversion for seismic source processes. Geophysical Journal International. doi:10.1111/j.1365-246X.2011.05043.x.
Yagi, Y., Kikuchi, M., 2000. Source rupture process of the Kocaeli, Turkey, earthquake of August 17, 1999, obtained by joint inversion of near-field data and teleseismic data. Geophysical Research Letters 27, 1969–1972.
Yagi, Y., Mikumo, T., Pacheo, J., 2004. Source rupture process of the Tecoman, Colima, Mexico earthquake of January 22, 2003, determined by joint inversion of teleseismic body wave and near-field data. Bulletin of the Seismological Society of America 94 (5), 1795–1807.
Yalçıner, A.C., Pelinovsky, E., Talipova, T., Kurkin, A., Kozelkov, A., Zaitsev, A., 2004. Tsunami in the Black Sea: comparison of the historical, instrumental and numerical data. Journal of Geophysical Research 109, C12023. doi:10.1029/2003JC002113.
Yolsal, S., 2008. Source Mechanism Parameters and Slip Distributions of Crete-Cyprus Arcs, Dead Sea Transform Fault Earthquakes and Historical Tsunami Simulations. PhD Thesis, 523 pages, Graduate School of Institute of Science and Technology, İstanbul Technical University, November 2008, İstanbul, Turkey.

Yolsal, S., Taymaz, T., 2010. Sensitivity analysis on relations between earthquake source rupture parameters and far-field tsunami waves: case studies in the Eastern Mediterranean Region. Turkish Journal of Earth Sciences 19, 313–349.

Yolsal, S., Taymaz, T., Yalçıner, A.C., 2007. Understanding tsunamis, potential source regions and tsunami prone mechanisms in the Eastern Mediterranean. *The Geodynamics of the Aegean and Anatolia,* Special Publication: Geological Society, London, Special Publications, 291, pp. 201–230.

Yolsal-Çevikbilen, S., Biryol, C., Beck, S., Zandt, G., Taymaz, T., Adıyaman, H., Özacar, A., 2012. 3-D Crustal structure along the North Anatolian Fault Zone in North Central Anatolia revealed by local earthquake tomography. Geophysical Journal International 188, 819–849. doi:10.1111/j.1365-246X.2011.05313.x.

Yoshida, S., 1992. Waveform inversion for rupture process using a non-flat seafloor model: application to 1986 Andreanof Islands and 1985 Chile earthquakes. Tectonophysics 211, 45–59.

Zitter, T.A., Woodside, J.M., Mascle, J., 2003. The Anaximander Mountains: a clue to the tectonics of southwest Anatolia. Geological Journal 38, 375–394.